Anisotropic magneto-transport properties of epitaxial magnetite thin films

Rafael Ramos

School of Physics

Trinity College Dublin

A thesis submitted to the University of Dublin, Trinity College, in application for the degree of

Doctor of Philosophy

30th October 2009

Declaration

This thesis is submitted by the undersigned for examination for the degree of Doctor of Philosophy at the University of Dublin. It has not been submitted as an excercise for a degree at any other Univesity.

Apart from the advice, assistance and joint effort mentioned in the under signed and in the text, is entirely my own work.
I agree, that the library may lend or copy this thesis freely upon request.

I would like to dedicate this thesis to Aldara, Noa and Xerome.

Acknowledgements

It has been five very long years since I moved to Dublin with Aldara to start a post-graduate course, during this time I made some new friends and had a beatiful little girl named Noa and a little boy, Xerome who always has a smile on his face. They are the cheer of my life.

I am grateful to many people who have helped me in my endeavors. As with most similar lists, omission from this section by no means symbolizes a lack of thanks, merely absentmindedness on my part.

I would like to thank my supervisor Prof. Igor Shvets for his support and giving me the opportunity to work in his group at Trinity College Dublin.

I am also grateful to Dr Sunil K Arora for some of the discussions and for proof reading this thesis.

I am grateful to Dr Xuesong Jin for his selfless help and teaching me the basics when I first joined the group.

I would like to thank Ciaran for sharing the breaks and for his advice and many of the proof readings. Floriano for the time we share together during the last five years, for his sarcastic approach to our survival times, I also want to thank him for the moka he gave me to make proper coffee, Simona for one of the nicest cakes I ever tried. Barry for minding Noa when I went to New Grange. Sumesh for his

invaluable help and many scientific and non-scientific disscussions, I am also thankfull to Parvathy and Sidhart. Han Chun for sharing those delicious centra lunches every day (sometimes we also went for proper ones), many scientific advice and his invaluable help. Giuseppe for inviting me to the Italian soccer matches. Ricardo for his positivism and his pleasant company. Kevin for the climbing sessions and giving me directions of what to do, where to go in Austin. Paul for the many diverse talks and proof reading this thesis. Asia for minding my cat, Patucos, and feeding my fishes. Cormac for the cake. Karsten Rode for his help on XRD measurements. Plamen Stamenov for his help on PPMS measurements. Robbie Gunning for organizing soccer matches. Olaf for the Metallica concert and bringing me to the Fiber Magis. Tarek and Zhou for their help on EBL. Mohamed for his honesty, opening my eyes and showing me what is like to do science. Gen and Ciaran Fowley for showing me how to use ion milling. Gareth Keeley for organizing the soccer games. Michele Byrne for proof reading some of the chapters.

I'm pretty sure I might forget someone, I also like to thank all group members, present and past: Victor, Ruggero, Xiao Min, Elizabeta, Karsten Fleitscher, Yang, Sundar, Roman, Keith, Guido, Ken Jordan, Sergio Ceballos, Alex, Marie Kinsella. And staff of School of Physics and CRANN :Robbie Gallagher, Ken Concannon, Pat Murphy, Dave Momahony, Mike Finneran, Des Keany.

Una mencion especial para Aldara por su incondicional apoyo y paciencia, Noa y Xerome por la inspiración. Tambien quiero agradecer a Fuco y Carlos por los ánimos y por las discusiones trascendentales en el balcón, a Pepa por el capitulo 8, je, je... a Manuel, a Chus.

A mis padres por siempre actuar en el mejor interes de Adriana y yo. Adriana por los ánimos a Barcala, Conchi, Demi, Carlos, Juan, Laura. A los abuelos. A Toño por su admirable carácter, a los Kurmans y a todo aquel que crea que debería esta incluido y se me ha olvidado.

Summary

In this thesis we investigate the anisotropic magneto-transport properties of epitaxial Fe_3O_4 films grown on MgO substrates. In particular we investigate the angular dependence of the anisotropic magnetoresistance (AMR), its relation to the conduction mechanism and the presence of defects. The magneto-transport properties of nanoscale gap contacts on Fe_3O_4 films were also investigated.

In chapter 5 we study the angular and temperature dependence of the AMR in epitaxial Fe_3O_4 films of different thickness grown on MgO(001) substrates and a Fe_3O_4(001) single crystal. We observe an additional cubic anisotropy in AMR, superimposed to the conventional two-fold anisotropy. The observed effect is independent of thin film thickness and also present in the Fe_3O_4(001) single crystal, suggesting that it is not exclusive to the epitaxial films but rather an intrinsic property of Fe_3O_4. The observation of this anomalous cubic component of AMR was compared with the mechanism of the Verwey transition suggesting that its origin could be related to a possible change in the conduction mechanism of magnetite due to presence of polarons.

In chapter 6 we have studied the AMR of Fe_3O_4 thin films grown on MgO(001) substrates with a miscut angle with respect to the (001) plane along the <100> direction, the presence of miscut allows the

formation of atomic steps on the MgO surface. Measurements of in-plane magnetization hysteresis loops show that the presence of atomic steps induces an uniaxial anisotropy within the plane of the films, which could be observed at all temperatures studied. This uniaxial anisotropy could be understood in terms of anisotropy in the magneto-elastic response of the film due to the different strain status in the directions parallel or perpendicular to the steps edges (SE). Another interesting feature is the different angular dependence of AMR in these samples for current applied parallel or perpendicular to the SE direction at temperatures below the Verwey transition. The observed differences are explained within the two band picture of AMR.

In chapter 7, we present magneto-transport measurements in Fe_3O_4 films on MgO(001) with nano-scale gaps of different dimmensions. The field dependent magnetoresistance (MR) shows different behaviour depending on the size of the gaps. In the case of probing 1-2 antiphase boundaries (80 nm gap) the MR shows linear dependence with the applied magnetic field while the MR behaviour is non-linear when measuring a single magnetite domain (30 nm gap).

In chapter 8, we give a short summary of the work in this thesis.

Publications:

1. **R. Ramos**, S.K. Arora, R.G.S. Sofin, and I.V. Shvets.
   Step-density dependence of the anisotropic magnetoresistance and magnetization reversal of Fe_3O_4 films grown on vicinal MgO(001) substrates.
   (In preparation.)

2. Han-Chun Wu, M. Abid, B.S. Chun, **R. Ramos**, O.N. Mryasov, and I.V. Shvets.
   Probing anti-phase boundaries and single magnetite domain using nanogap contacts.
   Nano Letters. (Submitted)

3. J.M. Caicedo, G. Herranz, **R. Ramos**, S.K. Arora, I.V. Shvets and J. Fontcuberta.
   Magnetopolaron optical conductivity in magnetite.
   Phys. Rev. Lett. (Submitted)

4. **R. Ramos**, S.K. Arora, and I.V. Shvets.
   Influence of miscut on the anisotropic magnetoresistance of magnetite thin films.
   J. Appl. Phys., **105**, 07B108 (2009).

5. **R. Ramos**, S.K. Arora, and I.V. Shvets.
   Anomalous anisotropic magnetoresistance in epitaxial Fe_3O_4 thin films on MgO(001).
   Phys. Rev. B, **78**, 214402 (2008).

6. K. Hild, J. Maul, T. Meng, M. Kallmayer, G. Schrohense, H.J. Elemers, **R. Ramos**, S.K. Arora and I.V. Shvets.
   Optical magnetic circular dichroism in threshold photoemission from a magnetite thin film.
   J. Phys. Condens. Matter., **20**, 235218 (2008).

7. X. Jin, **R. Ramos**, Y. Zhou, C. McEvoy and I.V. Shvets.
   Planar Hall effect in magnetite (100) films.
   J. Appl. Phys., **99**, 08C509 (2006).

8. Y. Zhou, C. McEvoy, **R. Ramos**, and I.V. Shvets.
   The magnetic and magnetoresistance properties of ultrathin magnetite films grown on MgO substrate.
   J. Appl. Phys., **99**, 08J111 (2006).

List of Abbreviations:

AF - antiferromagnetic

AGFM - alternating gradient field magnetometer

AMR - anisotropic magnetoresistance

APB - anti-phase boundary

APD - anti-phase domain

ATLAS - atomic terrace low angle shadowing

BMP - bound magnetic polaron

CCR - closed cycle refrigeration

CMR - colossal magnetoresistance

DMS - dilute magnetic semiconductors

DWR - domain wall resistance

EBL - electron beam lithography

EP - electron-phonon

FERAM - ferroelectric random access memory

FM - ferromagnetic

FMR - ferromagnetic resonance

FWHM - full width half maximum

HRXRD - high resolution x-ray diffraction

LRO - long-range order

MBE - molecular beam epitaxy

MRAM - magnetic random access memory

MIT - metal-insulator transition

MR - magnetoresistance

MTJ - magnetic tunnel junction

PPMS - physical properties measurement system

RHEED - reflection high energy electron diffraction

SE - step edge

SEM - scanning electron microscope

SP - small polaron

SPM - super paramagnetic

SRO - short-range order

STM - scanning tunneling microscopy

TEM - transmission electron microscope

TMR - tunneling magnetoresistance

T_V - Verwey temperature

UHV - ultra high vacuum

UV - ultra-violet

VRH - variable range hopping

VSM - vibrating sample magnetometer

XRR - x-ray reflectivity

List of Figures

LIST OF FIGURES

List of Tables

Contents

Chapter 1

Introduction

Spintronics is a multidisciplinary field which focuses on the active control and manipulation of spins in solid state systems. The field gained increased interest after the discovery of giant magnetoresistance (GMR) in magnetic multilayers in the late 1980s. The GMR consists on an enhancement of the magnetoresistance due to spin scattering between the ferromagnetic electrodes separated by a non-magnetic metal [1, 2]. In parallel with the above mentioned developments, advances were made on the growth of high-quality oxide thin films, mainly motivated by the discovery of high-temperature superconductivity in oxides [3]. Experience in the oxide thin film growth proved to be crucial for realization of high quality magnetic tunnel junctions (MTJ).

The initial interest in oxides for MTJs was a consequence of the predicted enhancement of the tunneling magnetoresistance (TMR), if a half metallic ferromagnet was used as electrodes. Since among the materials that have been predicted to be half metals, many are oxides [4], this triggered an intensive research in the area of ferromagnetic oxide thin films for spintronic applications. MTJs with manganite electrodes yielded tunneling magnetoresistance values $\sim$ 1000 %, orders

of magnitude higher than those obtained with metallic electrodes [5, 6, 7, 8, 9] However the TMR decreased rather rapidly with the temperature. This problem motivated the search to explore MTJs based on other half metallic ferromagnets with higher Curie temperatures.

One possible candidate was magnetite (Fe_3O_4), the first magnetic material known to mankind. It belongs to the family of the spinel ferrites, with ferrimagnetic ordering ocurring at a temperature as high as 858 K [10]. Band structure calculations predicted a half metallic behaviour [11, 12, 13], however, observed TMR results were far from promising [14, 15, 16]. This was initially attributed to the interface between Fe_3O_4 and MgO layers, however transmission electron microscopy (TEM) studies showed sharp interfaces [16, 17].

The most famous characteristic of magnetite is the presence of a metal to insulator transition (Verwey transition) at a temperature of $\sim$ 125 K [18, 19] in which the conductivity abruptly decreases by two orders of magnitude. The nature of this transition, in spite of almost 70 years of dedicated research, is still the matter of controversy [20, 21].

There are also claims of observed ferroelectric behaviour at temperatures well below the Verwey transition, first observed in single crystals [22] and more recently on thin films [23].

Epitaxial films of Fe_3O_4 are usually grown on MgO substrate, due to the small lattice mistmatch between thin film and substrate. However this hetero-epitaxial system is known to suffer from the formation of anti-phase boundaries (APB), these are natural growth defects due to the difference in translational and rotational symmetry between Fe_3O_4 and MgO [24]. Presence of APBs can affect the spin polarized conduction of electrons due to the anti-ferromagnetic (AF) coupling present across a significant fraction of these boundaries [25, 26]. Defining devices with lateral sizes in the deep sub-100-nm range might permit to have a

better picture of their role in the transport properties [27].

All the above mentioned characteristics make magnetite a very interesting material for research studies, from the fundamental point of view as well as possible applications. An understanding of the mechanisms which govern the magnetotransport properties of Fe_3O_4 thin films is of fundamental importance for its possible applications as a device or sensor. One of the mechanism contributing to the magnetotransport phenomenon is the anisotropic magnetoresistance (AMR). The AMR manifests as a change of electric resistance upon varying magnetization direction [28, 29, 30]. Although the experimental observation of the AMR is rather direct, its theoretical understanding is far from being complete. Most of the theoretical efforts have focussed, almost entirely on 3d ferromagnetic metals and its alloys and it is believed to be a consequence of the spin-orbit interaction [30, 31, 32, 33, 34, 35]. Despite large number of investigations of AMR on magnetic oxides [36, 37, 38] all attempts to understand the observed results have been based on the model developed for metals, owing to the complexity of interactions involved in these strongly correlated systems, which makes the development of a theory of AMR on oxides a very difficult challenge.

1.1 Outline of this thesis

Previous studies of AMR in Fe_3O_4 films have only focussed on the magnitude of the AMR ratio but not on the magnetic field direction dependence of the magnetoresistance. The main theme of this work is the study of the angular dependence of the anisotropic magnetoresistance. Related questions that will be addressed are: the relation of the AMR to the conduction mechanism in magnetite. How the presence of defects (APBs) can affect the angular response

of the AMR in vicinal samples. APBs are known to affect the magnetic and transport properties of magnetite films [25, 39, 40], for this reason it is interesting to study the magnetotransport properties across a single APB and compare it with the measurements in a single domain of magnetite.

A detailed description chapter by chapter of the work presented is given below:

Chapter 2: In this chapter we provide in detail overview of the general properties of magnetite bulk and thin films. We start with a description of some common properties of magnetite such as the crystal structure, magnetic properties and the metal to insulator transition (Verwey transition), finishing with the formation of antiphase boundaries (APBs) in thin film grown on MgO(001) substrates.

Chapter 3: In this chapter we briefly introduce the anisotropic magnetoresistance theory at the microscopic level as well as a description of the phenomenological approach. We also provide a brief description of the applications of anisotropic magnetoresistance.

Chapter 4: In this chapter we discuss the experimental techniques used in the present work. In section 4.2 details of the MBE system and the *in-situ* reflection high energy electron diffraction (RHEED) are given. In section 4.3 a description of the *ex-situ* characterization techniques is provided, these includes details of high resolution X-ray diffraction (HRXRD), alternating gradient field magnetometer (AGFM), vibrating sample magnetometer (VSM), physical property measurement system (PPMS). In section 4.4 we provide a brief description of the lithography techniques.

Chapter 5: In this chapter we present the results obtained for the anisotropic magnetoresistance of magnetite single crystal and epitaxial thin films grown on flat MgO(001) substrates. As the samples are cooled down an additional component in angular dependence of the magnetoresistance develops, the origin of this

anomalous anisotropic magnetoresistance is possibly related to the conduction mechanism of magnetite and the formation of polarons at temperatures higher than the Verwey transition.

Chapter 6: In this chapter we present the results of Fe_3O_4 films grown on vicinal MgO(001) substrates with a miscut with respect to the (001) plane along the <100> direction. Results of the in-plane magnetization hysteresis loops show that the presence of steps induces an in-plane easy axis behaviour in the direction perpendicular to the step edges, possibly related to the different magneto-elastic response of the film in the directions parallel or perpendicular to the steps respectively. Another interesting feature is the different angular dependence of AMR in the films with respect to the direction of applied current at temperatures below the Verwey transition. The observed differences are explained within the two band picture of AMR.

Chapter 7: In this chapter we discuss the magneto-transport properties of Fe_3O_4 films grown on MgO(001) substrates, in which nanoscale gaps of different dimension have been deposited. Since the anti-phase domain (APD) size between two APBs scales with the thickness of the films, measurements of gaps of different dimmensions are expected to provide information about the magneto-transport properties of a single APB or a single magnetite domain. The results clearly show the feasibility to probe antiphase boundaries as well as a single magnetite domain, with different magneto-transport response in each case respectively.

Chapter 8: In this chapter we summarise the main results of the thesis, we also present the preliminary steps for the fabrication of an exchanged bias magnetoresistive medium, for the measurement of domain wall resistance and discuss the future work.

References

[1] Baibich, M. N., Broto, J. M., Fert, A., Dau, F. N. V., and Petroff, F. *Phys. Rev. Lett.* **61**, 2472 (1988).

[2] Binash, G., Grünberg, P., Saurenbach, F., and Zinn, W. *Phys. Rev. B* **39**, 4828 (1989).

[3] Bednorz, J. G. and Mueller, K. A. *Z. Phys. B, Condens. Matter* **64**, 189 (1986).

[4] Coey, J. M. D. and Sanvito, S. *J. Phys. D: Appl. Phys* **37**, 988 (2004).

[5] Lu, Y., Li, W., Gong, G., Xiao, G., Gupta, A., Lecoeur, P., Sun, J., Wang, Y., and Dravid, V. *Phys. Rev. B* **54**, R8357 (1996).

[6] Sun, J. Z., Gallagher, W. J., Ducombe, P. R., Krusin-Elbaum, L., Altman, R. A., Gupta, A., Lu, Y., Gong, G. Q., and Xiao, G. *Appl. Phys. Lett.* **69**, 3266 (1996).

[7] Sun, J. Z., Krusin-Elbaum, L., Duncombe, P. R., Gupta, A., and Laibowitz, R. B. *Appl. Phys. Lett.* **70**, 1769 (1997).

[8] Viret, M., Drouet, M., Nassar, J., Contour, J. P., Fermon, C., and Fert, A. *Europhys. Lett.* **39**, 545 (1997).

[9] Bowen, M., Bibes, M., Barthélémy, A., Contour, J. P., Anane, A., Lemaître, Y., and Fert, A. *Appl. Phys. Lett.* **82**, 233 (2003).

[10] Glasser, M. and Milford, F. J. *Phys. Rev.* **130**, 1783 (1963).

[11] Zhang, Z. and Satpathy, S. *Phys. Rev. B* **44**, 13319 (1991).

[12] Antonov, V. N., Harmon, B. N., and Yaresko, A. N. *Phys. Rev. B* **67**, 024417 (2003).

[13] Yanase, A. and Saratori, K. *J. Phys. Soc. Jap.* **53**, 312 (1984).

[14] Seneor, P., Fert, A., Maurice, J.-L., Montaigne, F., Petroff, F., and Vaurès, A. *Appl. Phys. Lett* **74**, 4017 (1999).

[15] Alldredge, L. M. B., Chopdekar, R. V., Nelson-Cheeseman, B. B., and Suzuki, Y. *J. Appl. Phys.* **99**, 08K303 (2006).

[16] Li, X. W., Gupta, A., Xiao, G., Qian, W., and Dravid, V. P. *Appl. Phys. Lett* **73**, 3282 (1998).

[17] Arora, S. K., Sofin, R. G. S., Shvets, I. V., and Luysberg, M. *J. Appl. Phys.* **100**, 073908 (2006).

[18] Verwey, E. J. W. and Haayman, P. W. *Physica* **8**, 979 (1941).

[19] Verwey, E. J. W., Haayman, P. W., and Romeijn, F. C. *J. Chem. Phys.* **15**, 181 (1947).

[20] Walz, F. *J. Phys.: Condens. Matter.* **14**, R285 (2002).

[21] García, J. and Subías, G. *J. Phys. Cond. Matter.* **16**, R145 (2004).

[22] Rado, G. T. and Ferrari, J. M. *Phys. Rev. B* **12**, 5166 (1975).

[23] Alexe, M., Ziese, M., Hesse, D., Esquinazi, P., Yamauchi, K., Fukushima, T., Picozzi, S., and Gösele, U. *Adv. Mater.* **21**, 1 (2009).

[24] Hibma, T., Voogt, F. C., Niesen, L., a. van der Hieijden, P. A., de Jonge, W. J. M., Donkers, J. J. T. M., and van der Zaag, P. J. *J. Appl. Phys* **85**, 5291 (1999).

[25] Eerenstein, W., Palstra, T. T. M., Saxena, S. S., and Hibma, T. *Phys. Rev. Lett.* **88**, 247204 (2002).

[26] Celotto, S., W.Erenstein, and Himba, T. *Eur. Phys. J. B* **36**, 271 (2003).

[27] Eerenstein, W., Palstra, T. T. M., Hibma, T., and Celotto, S. *Phys. Rev. B* **68**, 014428 (2003).

[28] Thomson, W. *Proc. Roy. Soc.* **8**, 546 (1857).

[29] Döring, W. *Ann. Phys.* **32**, 259 (1938).

[30] Jaoul, O., Campbell, I. A., and Fert, A. *J. Magn. Magn. Mater.* **5**, 23 (1977).

[31] Smit, J. *Physica* **17**, 612 (1951).

[32] Berger, L. *Physica* **30**, 1141 (1964).

[33] McGuire, T. R. and Potter, R. I. *IEEE Trans. Mag.* **11**, 1018 (1975).

[34] Potter, R. I. *Phys. Rev. B* **10**, 4626 (1974).

[35] Malozemoff, A. P. *Phys. Rev. B* **34**, 1853 (1986).

[36] Bibes, M., Laukhin, V., Valencia, S., Martnez, B., Fontcuberta, J., Gorbenko, O. Y., Kaul, A. R., and Martínez, J. L. *J. Phys. Condens. Matter* **17**, 2733 (2005).

[37] Ziese, M. and Sena, S. P. *J. Phys.: Condens. Matter* **10**, 2727 (1998).

[38] Wang, L. M. and Guo, C.-C. *Appl. Phys. Lett.* **87**, 172503 (2005).

[39] Arora, S. K., Sofin, R. G. S., and Shvets, I. V. *Phys. Rev. B* **72**, 134404 (2005).

[40] Margulies, D. T., Parker, F. T., Spada, F. E., Goldman, R. S., Li, J., Sinclair, R., and Berkowitz, A. E. *Phys. Rev. B* **53**, 9175 (1996).

Chapter 2

Properties of magnetite

2.1 Introduction

Magnetite, the famous lodestone, is the oldest magnetic material known to man. It is abundantly found in nature (specially in rocks) and was first discovered in Greece around 2000 BC. It belongs to a family that includes sixteen iron oxides, hydroxides and oxide hydroxides. Iron oxides are widespread in nature and are of interest to many scientific disciplines (Figure 2.1). The major applications of iron oxides include pigments for paints and the construction industry, magnetic pigments and ferrites, catalysts for industrial syntheses and raw material for the iron and steel industry [1]. In more recent times magnetite has been more extensively studied because of its very high Curie temperature of 858 K [2] and predicted half metallic ferromagnetic properties (electrons at the Fermi level fully spin polarised) [3, 4, 5, 6], making it a very interesting candidate for applications in spin electronics. Magnetite also presents a metal to insulator transition at a temperature of 125 K, known as Verwey transition, the origin of which is still under debate [7, 8, 9].

In the following sections, we provide details of the properties of bulk and thin films of magnetite.

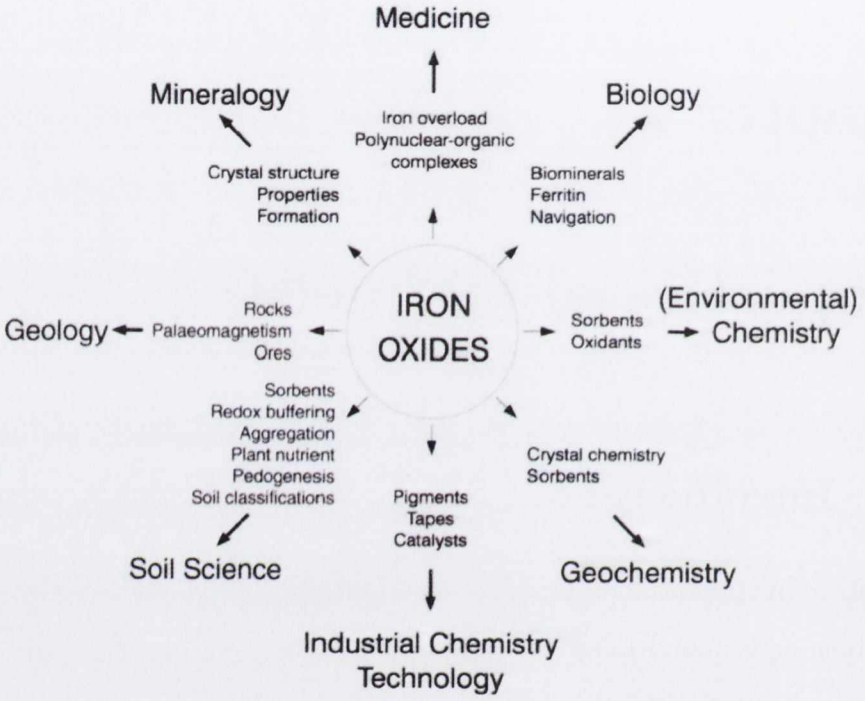

Figure 2.1: Widespread spectrum of research and application of iron oxides. Reproduced from [1]

2.2 Crystal structure

The main details of the structure of magnetite (Figure 2.2(a) were established in 1915; this was one of the first minerals to which X-ray diffraction was applied [10, 11] It crystallizes on the inverse spinel structure with a lattice constant of 0.8397 nm [12, 13].

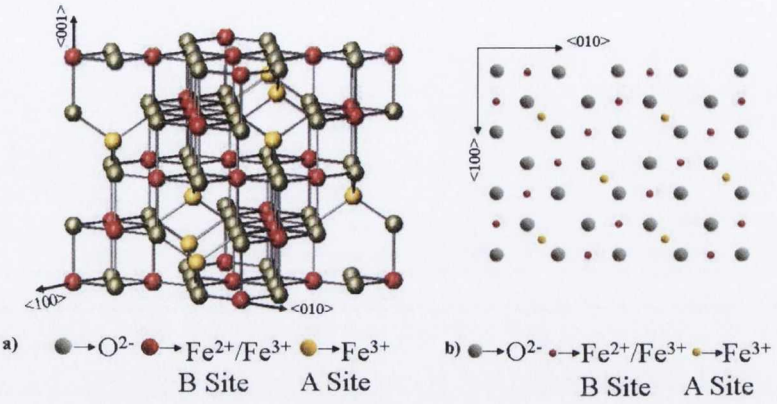

Figure 2.2: (a) 3D view of the unit cell of Fe_3O_4 containing 32 oxygen anions (grey) 16 octahedral iron ions (red) and 8 tetrahedral iron ions (yellow). (b) (001) plane of Fe_3O_4. The tetrahedral iron ions (yellow) are half way between two planes of octahedral iron ions (red) and oxygen ions (grey).

The spinel structure is a cubic structure, which belongs to the space group O_h^7-Fd$\bar{3}$m [14]. The unit cell of Fe_3O_4 comprises 4 formula units and is composed of 32 O^{2-} and 24 $Fe^{2+,3+}$ cations. The 32 oxygen anions are arranged in a face-centered cubic (fcc) lattice that embrace 64 tetrahedral interstices (A-type) and 32 octahedral interstices (B-type). Normal spinels are formed when 1/8 of the A sites are occupied by 8 divalent ions and 1/2 of the B sites are occupied by 16 trivalent ions. Instead, Fe_3O_4 crystallizes in the inverse spinel structure, where 8 of the 16 ferric Fe^{3+} ions in the unit cell are placed in A sites, whereas the other 8 ions, together with the 8 ferrous Fe^{2+}, occupy the B sites, see Figure 2.2(a). The unit cell consists of four (001) layers separated by $\sim$ 0.21 nm, each layer containing the oxygen anions and the octahedral iron cations. The tetrahedral sites are located halfway between these layers. The B site cations run in strings in the <110> directions. In a (001) plane, alternating strings are occupied, see

Figure 2.2(b). The strings in consecutive layers in the (100) type planes are rotated by 90° with respect each other.

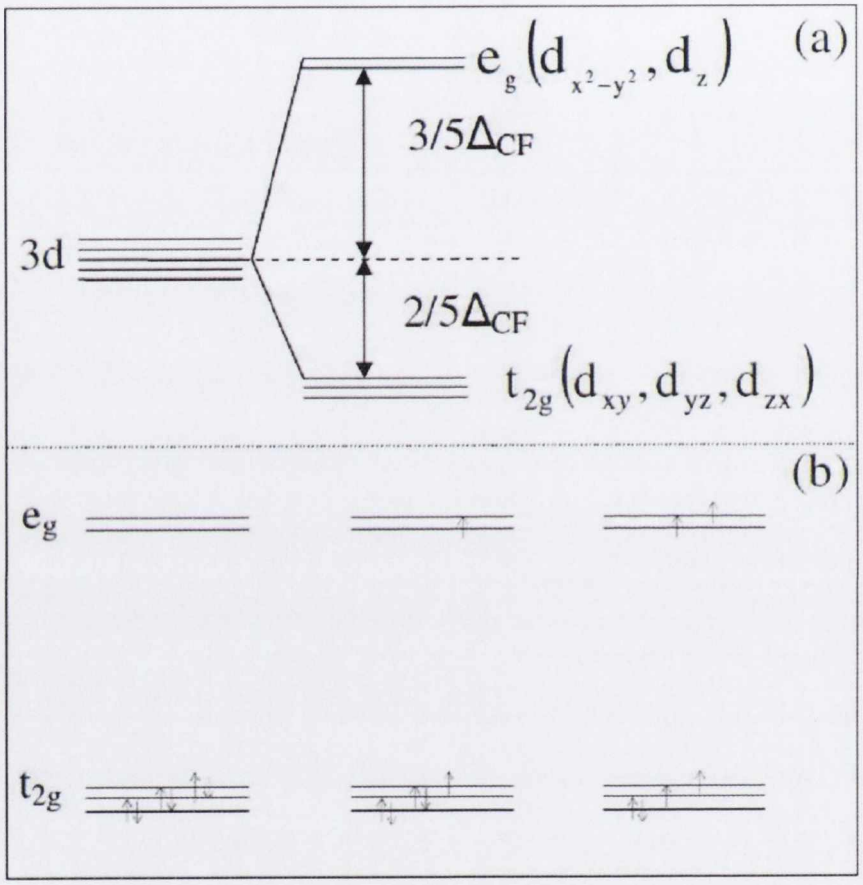

Figure 2.3: (a)Schematic representation of the splitting of the 3d electronic orbitals of an isolated iron ion in an octahedral crystal field. (Δ_{CF} is the crystal field splitting) (b) The three possible electronic configurations of Fe^{2+} in an octahedral site.

The room temperature conductivity, about 200 $\Omega^{-1}cm^{-1}$ was suggested to be the consequence of the electron delocalization between the octahedral neighbouring Fe ions (B-sites), presenting an average oxidation state of $Fe^{2.5+}$ [15, 16].

According to crystal field theory, it is possible to represent the state of the octahedral (B) sites of Fe_3O_4 as shown in Figure 2.3(a) [17]. The five d orbitals split into two levels consisting of two e_g levels and three t_{2g} levels. The two different iron ions, Fe^{2+} (d^6) and Fe^{3+} (d^5), are present in the octahedral sites. The Fe^{3+} ions are in a high spin state, with the 5 electrons arranged in parallel, in accordance with Hund's rule. The antiferromagnetic (AF) alignment of the two consecutive crystallographic planes causes the magnetic moment associated with these Fe^{3+} ions in the B-site to be cancelled by the one of the Fe^{3+} ions in the A-site. There are three electronic configurations possible for a Fe^{2+} ion, see Figure 2.3(b). The high spin configuration with 4 unpaired electrons is believed to be correct because it is in agreement with the value of the magnetisation measured experimentally of 4 μ_B per formula unit. The additional spin down electron of the Fe^{2+} ion in the octahedral site can hop to a neighbouring Fe^{3+} site provided their spins are parallel. In the magnetically ordered state, only the spin-down electron can easily move, resulting in spin-polarised electron transport. The electron transport is restricted to the B-sites. B sites are oriented ferromagnetically because of their mutual anti-ferromagnetic coupling to the A-site spins. The magnetic coupling will be further disscussed below.

2.3 Magnetic exchange interactions

There are several magnetic exchange interactions in Fe_3O_4. We can describe the magnetic exchange interaction between two neighbouring spins by the Heisenberg exchange hamiltonian:

$$H_{ex} = -\sum_{i,j} J_{ij} \vec{S}_i \cdot \vec{S}_j \tag{2.1}$$

where $\vec{S}_i$, $\vec{S}_j$ are the spin angular momentum of two electrons on neighbouring atoms and J_{ij} is a constant called the exchange integral. The sign and strength of the exchange integral depends on the distance, angle, spin and electronic configuration of the neighbouring ions. If J_{ij} is positive, the energy is lowest when the two spins are parallel to each other and is called (FM) interaction. For J_{ij} negative, moments of adjacent atoms point in opposite directions, resulting in the lowest energy state and is called antiferromagnetic (AF). A good description of the several exchange interactions is given by Goodenough [18].

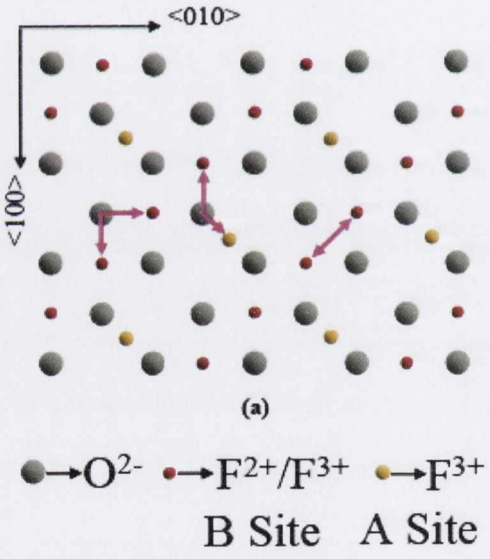

Figure 2.4: Schematic drawing of a (100) plane, showing the main exchange interactions in bulk magnetite

Figure 2.4 shows the most important exchange interactions in magnetite which are:

Cation-cation interactions: The most important interaction is the double exchange interaction between the iron ions of the octahedral sites [19]. This in-

teraction is based on the electron transfer between the Fe^{3+} and Fe^{2+}. Since the spin of the extra electron of Fe^{2+} is oppositely directed to the electrons of Fe^{3+}, electron transfer is only possible when both ions are aligned ferromagnetically. This increases the bandwidth of delocalisation of the extra electron, thereby decreasing its kinetic energy and favoring a ferromagnetic alignment.

Cation-oxygen-cation interactions (superexchange): The strength and sign of this exchange interaction depends on the angle between the ions and on the filling of the orbitals. Exchange between the two iron ions via the oxygen anion requires overlap of the orbitals. On the oxygen ions three p-orbitals contribute, of which two have a π-type symmetry and one has a σ-type symmetry [18, 20]. Of the five d-orbitals of iron, three posses a π-type symmetry (the three t_{2g}-orbitals) and two a σ-type symmetry (the two e_g-orbitals). The e_g-orbitals thus overlap with the oxygen p-orbitals with σ-type symmetry and the t_{2g}-orbitals with the oxygen p-orbitals with π-type symmetry. Because the σ-overlap is generally larger than π-overlap [18], σ-exchange is stronger.

- **125 degree iron-oxygen-iron exchange:** This is acting between the Fe^{3+} ions on the octahedral and tetrahedral sites. This is a strong anti-ferromagnetic coupling, largely due to overlap of the e_g-orbitals on the B site and t_{2g}-orbitals on the A sites. This exchange is responsible for the high Curie temperaute of 858 K.

- **90 degree iron-oxygen-iron exchange:** The angle between the octahedral iron ions and the intervening oxygen is 90 degrees. This leads to a ferromagnetic coupling between the iron ions, but this coupling is much weaker than the anti-ferromagnetic coupling between the A and B sublattices. Since the overlap between the iron t_{2g} and oxygen p orbitals is weak, this exchange is difficult to separate from the double exchange.

The magnetic ordering in magnetite is an example of Neel´s two sublattice model of ferrimagnetism [21]. In this model it is assumed that the A-B interaction is strongly negative and the interactions between the ions of the same sublattice weak. These interactions favor an antiparallel arrangement of the spins of the A-site and B-site ions. Thus the resultant magnetization is the difference between that of the A and B site ions. The magnetizations of the Fe^{3+} in tetrahedral and octahedral sites cancel each other, therefore the magnetic moment in Fe_3O_4 is that of Fe^{2+} ion in B sites, which is 4 μ_B and shows a saturation magnetization $\vec{M}_s = 48\text{x}10^4 A/m$.

2.4 Verwey transition

One of the most intriguing characteristic of magnetite is the presence of a metal to insulator trantition, known as Verwey transition [7]. The transition temperature (T_V) is 125 K at which the crystal structure changes from cubic to monoclinic [16, 22] and a charge ordering occurs at the B sites [23] thus reducing the conductivity. The band gap below T_V was estimated to be 0.22 eV [24].
Despite the fact that the Verwey transition has been extensively studied since the late 1940s, its mechanism is still a matter of discussion and controversy [8, 25, 26]. Various theoretical models have been proposed to explain the electron transport mechanism in the low- and high- temperature phases, and the sudden change in conductivity at the transition point [7, 8, 27]. Some of these models explain the Verwey transition as a complete order-disorder transition [7] of the charges of the conducting electrons. Anderson estimated that a transition between a Verwey order and complete disorder would be expected for temperatures of the order of 10^4 K [28]. To explain the much lower transition temperature measured exper-

imentally, he proposed that two different types of order are present at different temperatures: a long-range order (LRO) present at $T < T_V$ and a short-range order (SRO) that persists at $T > T_V$. He also postulated a condition for SRO, according to which, the minimum lattice energy is achieved provided every tetrahedron formed by the nearest-neighbor octahedral sites is occupied by two Fe^{2+} and two Fe^{3+} ions.

Recent studies demonstrated that the Verwey transition is a cooperative phenomenon, in which an interplay between lattice, charge and orbital degrees of freedom plays a decisive role. The idea that both Coulomb interactions and the electron-phonon (EP) coupling are responsible for the transition was first proposed by Ihle and Lorenz [29], their model provides a good description of the electric conductivity above T_V [24]. Piekarz et al. [9, 22] have recently investigated the mechanism of the Verwey transition in terms of a group theory analysis in conjuction with electronic structure calculations and analysis of the neutron scattering data. They concluded that in the presence of electron correlations the coupling between the electrons in t_{2g} states and phonons is largely enhanced since it leads to stabilization of the orbital ordering and a lowering of the total energy. This coupling between charge-orbital fluctuations and phonons can also account for the observed critical diffuse scattering observed by neutron scattering measurements, which show already about 200 K [30, 31, 32].

2.5 Thin films: formation of anti-phase boundaries (APBs) and induced exchange interactions

Physical properties of epitaxial Fe_3O_4 films deviate from those of the bulk, such as larger electrical resistivity [33], magnetoresistance [34, 35] and magnetization which does not saturate in fields of up to 7 Tesla [36]. These differences are attributed to the presence of antiphase boundaries (APBs) which are natural defects occurring during growth of Fe_3O_4 on MgO substrate. [36, 37] In the first stages of growth, islands of Fe_3O_4 are deposited on MgO. However, due to the difference in unit cell parameter and crystal symmetry, the different islands can be related by a shift vector, which is a fraction of the lattice unit vector [12, 36]. APBs are formed when islands of Fe_3O_4 on the MgO surface coalesce and the neighbouring islands are shifted with respect to each other [38]. The oxygen sublattice is more or less undisturbed across the APBs and only the cation lattice is shifted. The APBs are formed as a consequence of two types of symmetry breaking between MgO and Fe_3O_4. The first one is due to the lattice parameter of MgO (0.4213 nm) being half that of Fe_3O_4 (0.8397 nm). The second one is a result of the lower symmetry of the spinel structure of Fe_3O_4 ($Fd\bar{3}m$) compared to the rocksalt structure of the MgO substrate ($Fm\bar{3}m$). Consequently, adjacent Fe_3O_4 islands on the same MgO surface may be shifted with respect to each other resulting in the formation of APB. Eerenstein et al have reported that the APB's domain size increases significantly with film thickness [33].

Across the boundary there can be superexchange interactions that are not present in bulk Fe_3O_4 (see Figure 2.5). The magnetic exchange interactions across the APBs are very important because they can affect the physical properties of the

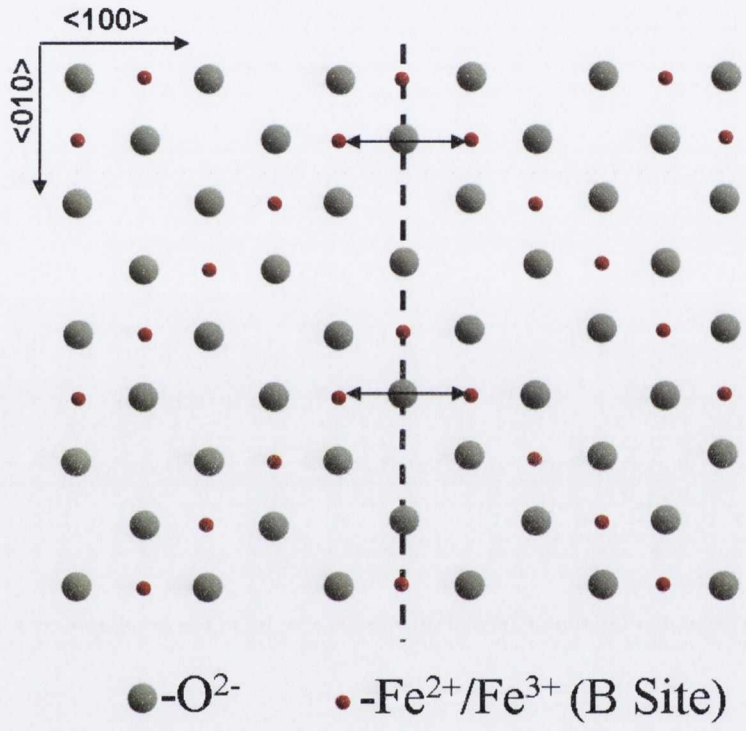

Figure 2.5: Schematic of the formation of APB and the induced 180° super-exchange interaction. The figure shows an APB formed by disruption of rotational symmetry, equivalent to an out-of-plane shift by a quarter of a lattice period.

Exchange interaction	Type and angle	Strength and sign	Presence
oct-ox-oct	super, 180°	AF, strong	At APB
tet-ox-tet	super, ~ 140°	AF, strong	At APB
oct-ox-tet	super, ~ 120°	AF, strong	Bulk and at APB
oct-ox-oct	super, ~ 90°	FM, weak	Bulk and at APB
tet-ox-tet	super, ~ 70°	AF, weak	At APB
oct-oct	direct	FM, weak	Bulk and at APB
tet-tet	direct	AF, weak	At APB
oct-tet	direct	FM, weak	At APB

Table 2.1: Magnetic exchange interactions in epitaxial Fe_3O_4 films on MgO. It can be observed the additional exchange interactions that are present across the antiphase boundaries. Reproduced from [37]

epitaxial Fe_3O_4 films. A detailed study of different magnetic exchange interactions across the APBs which are not present in the bulk Fe_3O_4 is reported by Celotto et al. [37]. Their analysis shows that across the APBs there can be other, 180 degree strong antiferromagnetic octahedraloxygen-octahedral super exchange, 90 degree weak ferromagnetic octahedral-oxygen-octahedral super exchange (which exists in addition to the 90 degree ferromagnetic super exchange in the bulk), additional double exchange interactions between octahedral iron ions (see Table 2.1) [37].

It is clear that the majority of strong interactions present in thin film are antiferromagnetic in nature [37]. In order to saturate the magnetization in Fe_3O_4, the magnetic field must be large enough to align all B site spins parallel to the field direction, while A site spins are antiparallel due to A-B exchange coupling.

In bulk crystals this occurs at relatively low fields (anisotropy field $\sim$ 0.031 T) which only needs to be large enough to overcome the crystalline anisotropy and dipolar fields (i.e. shape anisotropy). But in the case of thin films, in order to create this collinear arrangement of the spins the field must be large enough to overcome the strong exchange coupling across the APB which favours antiparallel spins on either side of the boundary. Since the exchange fields are very large, films remain unsaturated in fields as large as 7 T [36]. Since the presence of the APBs results directly from the growth process of Fe_3O_4 thin films grown on MgO substrates, the anomalous magnetic properties are intrinsic to the films, independent of preparation technique [39].

It has been recently shown that APBs can also be formed in hetero-epitaxial systems with same symmetry such as $Fe_3O_4/MgAl_2O_4$. The presence of APBs in such a system has been explained by the formation of misfit dislocations [40].

References

[1] Cornell, R. M. and Schwertmann, U. *The Iron Oxides.* Verlagsgellschaft mbH, (1996).

[2] Glasser, M. and Milford, F. J. *Phys. Rev.* **130**, 1783 (1963).

[3] Zhang, Z. and Satpathy, S. *Phys. Rev. B* **44**, 13319 (1991).

[4] Yanase, A. and Saratori, K. *J. Phys. Soc. Jap.* **53**, 312 (1984).

[5] Yanase, A. and Hamada, N. *J. Phys. Soc. Jap.* **68**, 1607 (1999).

[6] Dedkov, Y. S., Rüdiger, U., and Güntherodt, G. *Phys. Rev. B* **65**, 064417 (2002).

[7] Verwey, E. J. W., Haayman, P. W., and Romeijn, F. C. *Nature (London)* **144**, 327 (1939).

[8] Walz, F. *J. Phys.: Condens. Matter.* **14**, R285 (2002).

[9] Piekarz, P., Parlinski, K., and Olés, A. M. *Phys. Rev. B* **76**, 165124 (2007).

[10] Nishikawas, S. *Proc. Math. Phys. Soc. Tokyo* **8**, 199 (1915).

[11] Bragg, W. H. *Nature* **95**, 561 (1915).

[12] Voogt, F. C. *NO_2 assisted Molecular Beam Epitaxy of Iron Oxide Films.* PhD thesis, University of Groningen, The Netherlands, (1998).

[13] Wyckoff, R. W. G. *Crystal Structures*, volume 1-3. Krieger, Malabar, 2nd edition, (1982).

[14] Tables, I. C. *Phys. Lett* **1**, 251 (1962).

[15] Verwey, E. J. W. and Haayman, P. W. *Physica* **8**, 979 (1941).

[16] Verwey, E. J. W., Haayman, P. W., and Romeijn, F. C. *J. Chem. Phys.* **15**, 181 (1947).

[17] Khomskii, D. *Exchange and magnetism in Oxides.* Springer-Verlag, Berlin Heidelberg, (2001).

[18] Goodenough, J. B. *Magnetism and Chemical Bond.* Wiley New York, (1963).

[19] Cox, P. A. *Transition Metal Oxides*, 221–223. Oxford University Press, Oxford (1995).

[20] Atkins, P. W. *Physical Chemistry.* Oxford University Press, 5^{th} edition, (1994).

[21] Nel, L. *Ann. Phys. (Paris)* **3**, 137 (1948).

[22] Piekarz, P., Parlinski, K., and Olés, A. M. *Phys. Rev. Lett.* **97**, 156402 (2006).

[23] Wright, J. P., Attfield, J. P., and Radelli, P. G. *Phys. Rev. Lett.* **87**, 266401 (2001).

[24] Ihle, D. and Lorenz, B. *J. Phys. C: Solid State Phys.* **19**, 5239 (1986).

[25] García, J. and Subías, G. *J. Phys. Cond. Matter.* **16**, R145 (2004).

[26] Rozenberg, G. K., Pasternak, M. P., Xu, W. M., Amiel, Y., Hanfland, M., Amboage, M., Taylor, R. D., and Jeanloz, R. *Phys. Rev. Lett.* **96**, 045705 (2006).

[27] Mott, N. F. *Metal-Insulator Transitions.* Taylor and Francis, London, (1990).

[28] P. W. Anderson, P. W. *Phys. Rev.* **102**, 1008 (1956).

[29] Ihle, D. and Lorenz, B. *Philos. Mag. B* **42**, 337 (1980).

[30] Shapiro, S. M., Iizumi, M., and Shirane, G. *Phys. Rev. B* **14**, 200 (1976).

[31] Yamada, Y. *Phys. Rev. B* **21**, 4642 (1980).

[32] Siratori, K., Ishii, Y., Morii, Y., Funahashi, S., Todo, S., and Yanase, A. *J. Phys. Soc. Jpn.* **67**, 2818 (1998).

[33] Eerenstein, W., Palstra, T. T. M., Hibma, T., and Celotto, S. *Phys. Rev. B* **66**, 201101 (2002).

[34] Eerenstein, W., Palstra, T. T. M., Saxena, S. S., and Hibma, T. *Phys. Rev. Lett.* **88**, 247204 (2002).

[35] Arora, S. K., Sofin, R. G. S., Nolan, A., and Shvets, I. V. *J. Magn. and Magn. Mater.* **286**, 463 (2005).

[36] Margulies, D. T., Parker, F. T., Rudee, M. L., Speda, F. E., Chapman, J. N., Aitchison, P. R., and Berkowitz, A. E. *Phys. Rev. Lett* **79**, 5162 (1997).

[37] Celotto, S., W.Erenstein, and Himba, T. *Eur. Phys. J. B* **36**, 271 (2003).

[38] Hibma, T., Voogt, F. C., Niesen, L., a. van der Hieijden, P. A., de Jonge, W. J. M., Donkers, J. J. T. M., and van der Zaag, P. J. *J. Appl. Phys* **85**, 5291 (1999).

[39] Margulies, D. T., Parker, F. T., Spada, F. E., Goldman, R. S., Li, J., Sinclair, R., and Berkowitz, A. E. *Phys. Rev. B* **53**, 9175 (1996).

[40] Luysberg, M., Sofin, R. G. S., Arora, S. K., and Shvets, I. V. *Phys. Rev. B* **80**, 024111 (2009).

Chapter 3

Anisotropic magnetoresistance

3.1 Introduction

The physical properties of crystals are in some cases strongly directional. Crystals of the ferromagnetic materials are, in most cases, magnetically anisotropic to a remarkable degree, and have easy and hard directions of magnetization. Apart, however, from the crystalline anisotropy a ferromagnetic body may also have easy and hard axis depending on its shape. Small deformation of a material in a particular direction may introduce further directional effects.

The possible microscopic sources of magnetic ansisotropy [1] are on one side the dipole-dipole interaction, responsible mainly for shape anisotropy effects and on the other hand the spin-orbit coupling (crystalline anisotropy), where the spin couples to the charge density distribution in the crystal and the magnetization is coupled to the crystal via the orbital motion of the magnetic electrons, which are coupled to the lattice by the ligand field.

The anisotropic magnetoresistance could be considered as the transport equivalent of the crystalline anisotropy. It is manifested as a dependence of the resistiv-

ity of a ferromagnet on the angle between the magnetization $\vec{M}$ and the electric current $\vec{J}$, the phenomenon that was first discovered in 1857 by William Thomson [2]. The microscopic theory of AMR in metal ferromagnets began with the work of Smit [3], who explained this phenomenon using the two-current model of conduction in transition metals developed by Mott [4].
In this chapter we will give a brief summary of the theory from the microscopic and phenomenological approach, followed by past and present applications of AMR.

3.2 Microscopic theory

3.2.0.1 Two-current model

Mott's two-current model [4] of electrical conduction for transition metals assumes that the $4s$-electrons are mainly responsible for the current (due to their small effective mass compared to the $3d$-electrons) and that during a transition from an s to an s or d state the spin direction does not change. This is equivalent to divide the current into two independent parts with opposite spin (see Figure 3.1).

There are two types of scattering events, the $s-s$ intraband scattering and the $s-d$ interband scattering. Due to the higher density of states at Fermi level for the d band in comparison to the s band, the scattering between s and d electrons dominates ($s-d$ scattering). In order to obtain the conductivity, Mott started from the classical expression for metals

$$\sigma = \frac{ne^2}{\mu}\tau \tag{3.1}$$

where n is the number of electrons per unit volume, μ the effective mass of the

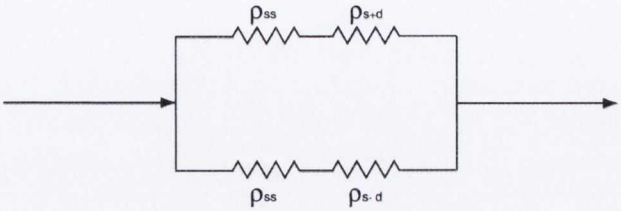

Figure 3.1: Equivalent circuit for the two current model. ρ_{ss} resistivity of s to s state scattering events, ρ_{s+d} (ρ_{s-d}) resistivity of s to d state scattering events in the majority (minority) spin channel respectively. By majority spin channel, it is meant, the electrons which spins point in the same direction as the magnetization of the material.

electron and τ the relaxation time. The relaxation time is given by

$$\frac{1}{\tau} = P^{s,n'}_{k,k'} \tag{3.2}$$

where $P^{s,n'}_{k,k'}$ is the probability of an s-electron with wave vector k to be scattered into a n'-electron (n': s or d) with wave vector k', which after Born approximation (small scattering potential) is given by the following formula

$$P^{s,n'}_{k,k'} \propto \frac{1}{4\pi^2\hbar} \frac{| < n', k'|V_{scatt}|s, k > |^2}{|\nabla'_k \epsilon(k')|} \tag{3.3}$$

this probability of scattering is proportional to the density of states of the final state ($1/\nabla'_k \epsilon(k')$) and to the square of the scattering potential matrix element $| < n', k'|V_{scatt}|s, k > |$ (where V_{scatt} is the scattering potential and $|s, k >$ and $|n', k' >$ are the initial and final states respectively). The expressions obtained by Mott always lead to isotropic conductivities because the bands are assumed to be isotropic.

3.2.0.2 Anisotropic Magnetoresistance

The anisotropic magnetoresistance is often defined [5]

$$AMR = \frac{\Delta\rho}{\rho_{ave}} = \frac{\rho_{||} - \rho_{\perp}}{\frac{1}{3}\rho_{||} + \frac{2}{3}\rho_{\perp}} \tag{3.4}$$

where ρ_{av} is the average resistivity (resistivity of the demagnetized specimen) and $\rho_{||}$ and $\rho_{\perp}$ are the resistivities parallel and perpendicular to the magnetization respectively.

If $s - d$ scattering is the dominant feature of transition-metal electronic conductivity, then the ferromagnetic resistance anisotropy must be a consequence of an anisotropic scattering mechanism. If we consider the expression for the scattering probabilities eq. (3.3), then the anisotropy could result from a lower-than-cubic-symmetry scattering potential or the $3d$ atomic wave functions ($|s, k>$, $|n', k'>$) should have less than cubic symmetry [1]. The latter is generally considered the more likely condition. The symmetry of the wave functions is lowered by the spin-orbit interaction as proposed by Smit [3]. This interaction has the form

$$H_{so} = \lambda\vec{L}\cdot\vec{S} = \lambda[L_z S_z + \frac{1}{2}(L_+ S_- + L_- S_+)] \tag{3.5}$$

with the z components and climbing operators of the spin and angular momentum defined in the usual way and λ denoting the spin-orbit interaction potential. H_{so} makes a contribution to the energy of the d states that depends on spin or magnetization direction, making it favorable for the magnetization to point along certain directions. Thus the d electron spin is coupled to its orbital motion,

[1] If one considers one of the axis of a cubic crystal, any of the other two axis of the crystal, which are rotated 90°, will be equivalent considering symmetry arguments, but from the definition of AMR (see Eq. 3.4), if the magnetization is in the x direction the resistivity will be different in the x or in the y direction ($\rho_{||}$ or $\rho_{\perp}$ respectively). This suggests that the scattering mechanism responsible for the AMR should present lower than cubic symmetry

which in turn is coupled to the lattice by the crystal field. As a consequence of this energy contribution, the d state wave functions must be recalculated using perturbation theory. The spin-orbit interaction causes a non-symmetrical mixing of majority and minority 3d states and the resultant perturbed wave functions exhibit a complex dependence on the angle of magnetization with respect to current direction.

Potter [6] performed a calculation of the AMR in NiCu alloys following the steps outlined above, but instead of taking the atomic d wave functions for the calculation of the spin-orbit perturbed wave functions, he considered the tight-binding ones obtained for Ni [7] in order to account for the band structure. He obtained the following expressions for the relaxation times τ_{s+d} (τ_{s-d}) for the majority (minority) spin channel $s-d$ scattering events respectively

$$\frac{1}{\tau_{s+d}} \propto \frac{2\pi}{\hbar} N_d (k_x^2 + k_y^2) k_z^2 \tag{3.6}$$

$$\frac{1}{\tau_{s-d}} \propto \frac{\pi}{8\hbar} N_d \left(\frac{\lambda}{H_{ex} + \Delta_{cf}}\right)^2 (k_x^2 - k_y^2)^2 \tag{3.7}$$

where $\hbar = h/(2\pi)$ (h is Planck's constant), N_d the density of d states, λ the spin-orbit coupling constant, H_{ex} the exchange splitting and Δ_{cf} the cristal field splitting, the $k_i's$ (i= x, y, z) are the wave vectors along diferent directions. Assuming that the magnetization points along the z-axis, we can transform into spherical coordinates to get

$$\frac{1}{\tau_{s+d}} \propto cos^2(\theta) - cos^4(\theta) \tag{3.8}$$

$$\frac{1}{\tau_{s-d}} \propto 1 - 2cos^2(\theta) + cos^4(\theta) \tag{3.9}$$

which shows the dependence of the inverse of the relaxation times with respect to the angle between magnetization and current direction.

In summary, the spin-orbit interaction makes an energy contribution to electrons

in the magnetization-controlling d states. This contribution depends on the direction of the magnetization, thus making it energetically favorable for the spin to point in particular directions. Therefore the orbital motion of the d electrons are coupled to their spin and the crystal lattice. The end result of introducing spin-orbit coupling into our picture of conduction is that now the d electron wave functions must be recalculated due to the energy shift, as a consequence the resultant perturbed wave functions show a lower than cubic symmetry, therefore the scattering potential matrix element $| < n', k'|V_{scatt}|s, k > |$ and the resistivity are anisotropic. The AMR in transition-metal ferromagnets is understood theoretically through the scattering of s-band carriers into empty d-band states. In the case of ferromagnetic oxides, even though the conduction mechanism is different, all the attempts to understand the results on AMR are based on the model developed for metals.

3.3 Expression arising from symmetry: Phenomenological expression

Usually this approach is followed in order to express the angular dependence of the AMR. The starting point is Ohm's law for a chemically homogeneous metal under isothermal conditions:

$$E_i = \sum_{j=1}^{3} \rho_{ij} J_j \tag{3.10}$$

where: $\vec{J} = (J_1, J_2, J_3)$ is the current density, $\vec{E} = (E_1, E_2, E_3)$ is the electric field and ρ_{ij} is the tensor of resistivity. If the metal is under the effect of some external magnetic field $\vec{H}$ the resistivity tensor depends on the magnetic field or on the magnetization

$$E_i = \rho_{ij}(\vec{H}) J_j = \rho_{ij}(\vec{M}) J_j \tag{3.11}$$

if the metal is a saturated single crystal the magnetization can be described by the direction cosines with respect to the crystallographic axes

$$\vec{M} = (M\alpha_1, M\alpha_2, M\alpha_3) = Mcos(\vec{\alpha}) \tag{3.12}$$

and the resistivity tensor in equation (3.10) depends only on $\vec{\alpha}$ ($\vec{\alpha}$ being the vector of the direction cosines).

$$E_i = \rho_{ij}(\vec{\alpha})J_j \tag{3.13}$$

where $\vec{\alpha} = (\alpha_1, \alpha_2, \alpha_3)$. After expansion on the direction cosines using MacLaurin's series this tensor is described by the expression

$$\rho_{ij}(\vec{\alpha}) = a_{ij} + a_{ijk}\alpha_k + a_{ijkl}\alpha_k\alpha_l + ... \tag{3.14}$$

where the Einstein summation convention is understood. The resistivity tensor can be divided into an even function of the $\vec{\alpha}$ and an odd function of the $\vec{\alpha}$, these are associated with the magnetoresistive and Hall effects, respectively. Since we are interested in the magnetoresistive part of the tensor, we will consider the terms of the expansion which are a function of $\vec{\alpha}$:

$$\rho^s_{ij} = a_{ij} + a_{ijkl}\alpha_k\alpha_l + ... \tag{3.15}$$

Considering Onsager's theorem $\rho_{ij}(\vec{\alpha}) = \rho_{ij}(-\vec{\alpha})$ and the crystal symmetry the tensor with elements a_{ij}, a_{ijkl} can be simplified [5]. Birss [8] obtained the nonzero elements for the point group m3m, to which the cubic crystals belong. The obtained magnetoresistivity tensor to fifth order in the α_i is

$$\begin{pmatrix} C'_0 + C'_1\alpha_1^2 + C'_2\alpha_1^4 + C'_3\alpha_2^2\alpha_3^2 & C'_4\alpha_1\alpha_2 + C'_5\alpha_1\alpha_2\alpha_3^2 & C'_4\alpha_1\alpha_3 + C'_5\alpha_1\alpha_3\alpha_2^2 \\ C'_4\alpha_1\alpha_2 + C'_5\alpha_1\alpha_2\alpha_3^2 & C'_0 + C'_1\alpha_2^2 + C'_2\alpha_2^4 + C'_3\alpha_3^2\alpha_1^2 & C'_4\alpha_2\alpha_3 + C'_5\alpha_2\alpha_3\alpha_1^2 \\ C'_4\alpha_1\alpha_3 + C'_5\alpha_1\alpha_3\alpha_2^2 & C'_4\alpha_2\alpha_3 + C'_5\alpha_2\alpha_3\alpha_1^2 & C'_0 + C'_1\alpha_3^2 + C'_2\alpha_3^4 + C'_3\alpha_1^2\alpha_2^2 \end{pmatrix}$$

where the $C'_i (i = 1, ...5)$ are linear combinations of the tensor elements

$a_{ij}, a_{ijk}, a_{ijkl}, ...$ The anisotropy comes from the higher order tensor elements $a_{ijkl}, a_{ijklmn}, ...,$ if this elements were not considered the resistivity tensor would be $\rho_{ij} = \rho\delta_{ij}$ [1] with $\rho = a_{11} = a_{22} = a_{33}$.

The resistivity along the current direction $\vec{\beta} = (\beta_1, \beta_2, \beta_3)$ (where β_i; $i = 1, 2, 3$ are the direction cosines of the current with respect to the crystallographic axes) can be written

$$\rho(\vec{\alpha}, \vec{\beta}) = \frac{\vec{J} \cdot \vec{E}}{|J|^2} = \frac{J_i \rho_{ij} J_j}{J_i J_j} = \beta_i \rho^s_{ij} \beta_j \tag{3.16}$$

This can also be written in the form

$$\begin{aligned} \rho(\vec{\alpha}, \vec{\beta}) \;=\; & C_0 + C_1[\alpha_1^2\beta_1^2 + \alpha_2^2\beta_2^2 + \alpha_3^2\beta_3^2] \\ & + C_2[\alpha_1\alpha_2\beta_1\beta_2 + \alpha_2\alpha_3\beta_2\beta_3 + \alpha_3\alpha_1\beta_3\beta_1] \\ & + C_3 s + C_4[\alpha_1^4\beta_1^2 + \alpha_2^4\beta_2^2 + \alpha_3^4\beta_3^2 + \\ & + 2C_5[\alpha_1\alpha_2\beta_1\beta_2\alpha_3^2 + \alpha_2\alpha_3\beta_2\beta_3\alpha_1^2 + \alpha_3\alpha_1\beta_3\beta_1\alpha_2^2] \end{aligned} \tag{3.17}$$

with s=$\alpha_1^2\alpha_2^2 + \alpha_2^2\alpha_3^2 + \alpha_3^2\alpha_1^2$. The constants C_i are $C_0 = C_0', C_1 = C_1' - C_3', C_2 = 2C_4', C_3 = C_3'$, and $C_4 = C_2' + C_3'$

The equation (3.17) indicates that a cubic single crystal sample with the current applied along one of its crystallographic axes, exhibits a resistivity of the form

$$\rho = C_0 + C_i\alpha_1^2 + C_4\alpha_1^4 + ... \tag{3.18}$$

In summary, the phenomenological approach allow us to extract the angular dependence of AMR. Even though there is no clear relation between the coefficients C_i and physical properties.

[1] δ_{ij} is Kronecker delta function where δ_{ij}=1 if i=j and zero otherwise

3.4 Applications

The birth of modern MRAM concepts took place at Honeywell the mid-1980s, with the invention of the first cells based on the anisotropic magnetoresistance [9, 10]. The material used for this sensors was a cobalt-permalloy alloy with a normal AMR ratio of about 2%. Despite imporvements in reading methods, the maximum differential resistance of the cell between a "1" and a "0" when it was read was about 0.5%, this gave differential sense signals of 0.5-1.0 mV. This amplitude of sense signal allowed 16 Kbit integrated chips to operate with a read access time of about 250 ns [11].

The discovery of the giant magnetoresistance (GMR) [12, 13] gave hope for

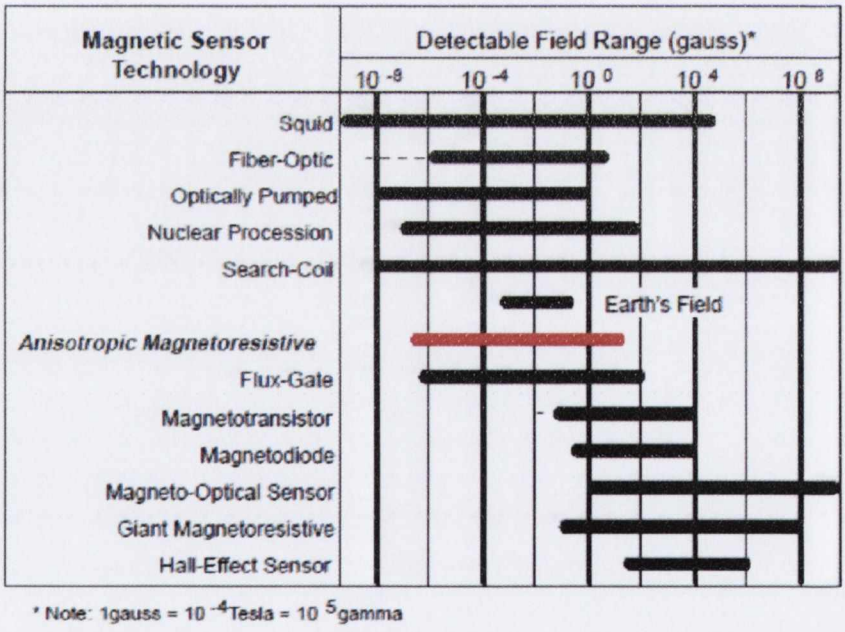

Figure 3.2: Typical field range of various magnetic field sensors.Reproduced from [15]

higher readout signal amplitudes and faster read access time eventually replacing the AMR sensors. Currently 4 Mbit tunneling magnetoresistance (TMR) based,

magnetic random access memories (MRAM) with access times as small as 35 ns are already being developed [14].

Anisotropic magnetoresistive sensors are still used nowadays to detect the direction and magnitude of external magnetic fields and due to the compatibility of AMR sensor range with the earth's magnetic field (see Figure 3.2) they can be used for compassing applications [16, 17].

References

[1] Farle, M. *Rep. Prog. Phys.* **61**, 755 (1998).

[2] Thomson, W. *Proc. Roy. Soc.* **8**, 546 (1857).

[3] Smit, J. *Physica* **17**, 612 (1951).

[4] Mott, N. F. *Proc. Roy. Soc.* **A153**, 699 (1936).

[5] McGuire, T. R. and Potter, R. I. *IEEE Trans. Mag.* **11**, 1018 (1975).

[6] Potter, R. I. *Phys. Rev. B* **10**, 4626 (1974).

[7] Fletcher, G. C. *Proc. Phys. Soc. Lond. A* **65**, 192 (1952).

[8] Birss, R. R. *Symmetry and Magnetism.* North-Holland Publishing Co. Amsterdam, (1964).

[9] Pohm, A. V., Daughton, J. M., Comstock, C. S., Yoo, H. Y., and Hur, J. *IEEE Trans. Mag.* **23**, 2575 (1987).

[10] Pohm, A. V., Huang, J. S. T., Daughton, J. M., Krahn, D. R., and Mehra, V. *IEEE Trans. Mag.* **24**, 3117 (1988).

[11] Hurst, A. and Granley, G. In *Proceedings of the 1996 Nonvolatile Memory Technology Conference* (, Alburquerque NM, 1996).

[12] Baibich, M. N., Broto, J. M., Fert, A., Dau, F. N. V., and Petroff, F. *Phys. Rev. Lett.* **61**, 2472 (1988).

[13] Barnás, J., Fuss, A., Camley, R. E., Grünberg, P., and Ziss, W. *Phys. Rev. B* **42**, 8110 (1990).

[14] http://www.everspin.com/products16-4Mb.html.

[15] Caruso, M. J. *Sensors* **15**, 34 (1998).

[16] Včelák, J., Ripka, P., Kubík, J., Platil, A., and Kašpar, P. *Sens. Actuators A* **123-124**, 122 (2005).

[17] Včelák, J., Ripka, P., Platil, A., Kubík, J., and Kašpar, P. *Sens. Actuators A* **129**, 53 (2006).

Chapter 4

Experimental techniques

4.1 Introduction

The advances in the area of study and application of thin film have developed over the last decades due to the improvement in ultra high vacuum technology (UHV) and deposition techniques. In this chapter we give a description of the methods used for thin film growth, characterization and the techniques used for micro-fabrication. The chapter is divided in three sections. In the first section , the thin film growth using molecular beam epitaxy (MBE) and in-situ analysis of the samples using reflection high energy diffraction (RHEED) are discussed. In the second section, the characterization techniques are described and in the last section the micro-fabrication methods are shown.

4.2 Molecular Beam Epitaxy

The films used for this study were grown by molecular beam epitaxy (MBE). This is a material deposition technique capable of predictably and reproducibly

yielding material with impurity levels below ten parts per billion [1], with unprecedented control over the precision with which the composition and doping of the structure can be tailored. Some of these attributes are intrinsic to the MBE process, e.g., slow growth rates and low deposition temperatures. The major advantages that make MBE a supreme tool for basic research as well as device production can be summarized as follows:

- MBE allows a very precise control of layer thickness and dopant incorporation down to the atomic scale.
- The UHV enviroment in the growth chamber allows the application of various in-situ measurement techniques to study the processes governing crystal growth. At the same time, these measurements can be used to implement real-time feedback loops for growth control.

Molecular beam epitaxy (MBE) involves the generation of flux of evaporated material (molecular beam) and their reaction at the substrate to form an ordered overlayer. Epitaxy is characterized by a continuation of crystal structure from substrate to the film, the deposited material is essentially single crystalline and it can be grown one monolayer at a time. Highly ordered crystalline films can be prepared in this way and used in a wide range of studies and applications [2, 3, 4, 5, 6, 7, 8, 9].

Elemental or compound constituents are heated (if in the solid state) or introduced (if gaseous) to cause mass transfer from the flux generators to the substrate, via the vapor phase. To maintain the high purity and integrity of the deposit, stringent vacuum conditions are needed. MBE is essentially a line-of-sight technique from source to substrate, and the fluxes of constituents (and thus the composition of the material perpendicular to the growth direction) can be temporally modulated either by altering the evaporation introduction conditions

or by physically interrupting the beam using rapid action mechanical shutters. In solid source MBE, material is evaporated from solid ingots by heating or with an electron beam. The basic principle of epitaxy is that atoms on a clean surface are free to move around until they find a correct position in the crystal lattice to bond. In practice there will be more than one nucleation site on a surface and so growth is by the spreading of islands. The mobility of an adatom on the surface will be greater at higher substrate temperature resulting in smoother interfaces, but higher temperatures also lead to a lower "sticking coefficient "and more migration of atoms within the layers already grown. Clearly there will be a compromise temperature to achieve the best results. Using MBE thin films can be grown with very precise control over the film thickness and stoichiometry, thus enhancing the reproducibility of quality thin film production.
In our MBE system a molecular beam of a metal is created by the evaporation of the source material using a beam of high energy electrons. The molecular beam subsequently condenses on a substrate and the thin film grows epitaxially. By controlling the flux of the molecular beam and by controlling the energy of the evaporating e-beam, one can control the growth rate of the thin film. Metal oxides may also be grown by MBE by simply adding the appropriate gas into the deposition chamber. The gas may be added in molecular or atomic form (using a plasma generator). In this manner we were able to produce the magnetite films for this research work. The low background pressure possible due to the advances in high vacuum technology ensure that the growing film remains contamination free for the time necessary to deposit the films and analyse them in situ.

All of the films grown and investigated during the course of the research outlined in this thesis were deposited using a DCA MBE M600 Molecular Beam Epitaxy System (see Fig. 4.1). The system comprised of two separated cham-

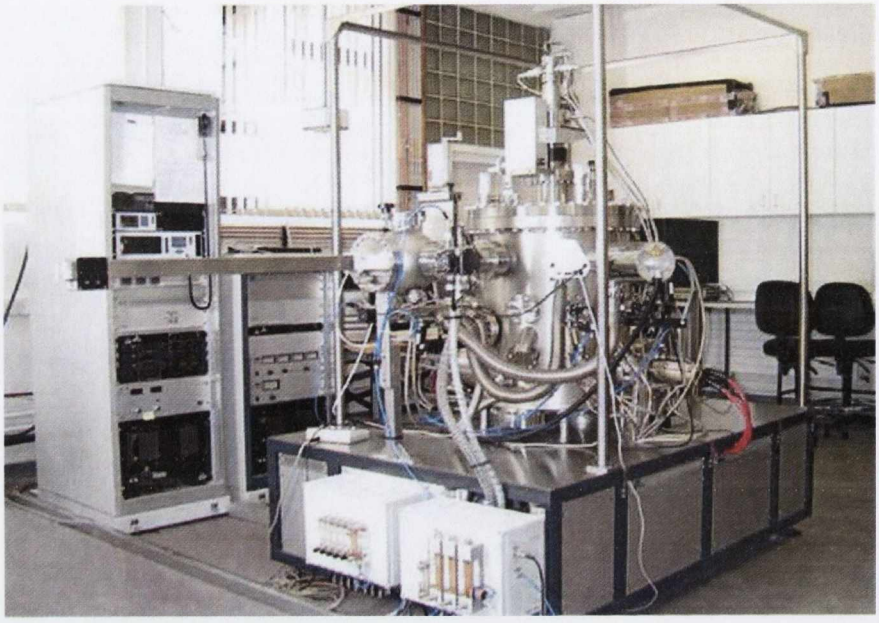

Figure 4.1: Molecular Beam Epitaxy system DCA MBE M600 used in this study.

bers connected via a gate valve. The chambers were designated the Load-Lock chamber and the Deposition chamber. Substrates and samples were transferred between the chambers using a magnetically coupled transfer arm, which had a transfer cup attached. The transfer cup facilitated transfer of the bare substrate/sample from the Load-Lock chamber to the Deposition chamber and vice versa. The deposition chamber was fitted with a reflection high energy electron diffraction (RHEED) system for in situ sample analysis. The base pressure of the Load-Lock chamber was of the order $5x10^{-7}$ Torr while the base pressure of the Deposition chamber was of the order of $5x10^{-10}$ Torr. The detailed description of different parts of MBE is given in the following sections.

4.2.1 Ultra high vacuum (UHV) system

The deposition chamber associated with the MBE system was a vertical 600 mm ID chamber with a wire sealed removable top flange. A schematic of the chamber is shown in Figure 4.2 The system was fitted with a low wobble substrate manipulator which consisted of a heavy duty Z-manipulator, a hollow shaft inverted rotary motion feed-through and a high temperature heater stage. The substrate manipulator was located vertically in centre of the chamber in such a way that the substrate was loaded facing downwards during all processes and manipulations.

The heater stage was a high temperature heater stage with a PBN/PG/PBN cup heater element. The element was surrounded by a radiation shield. A C-type thermocouple (W/Rh) was located in the space between the filament and the substrate. The temperature was controlled via a EUROTHERM 2408 controller used in conjunction with a DC power supply. All pre-deposition annealing was done *in situ* using the substrate manipulator heater, avoiding the need for a separate annealing chamber. This improved the quality of the cleaned substrates and minimised possible contaminants that may have arisen as a result of the transfer procedure between adjacent chambers. The heavy duty Z-stage was used for loading and RHEED alignment purposes. The manipulator also allowed the substrate to be lowered to any height above the main shutter thus increasing the effectiveness of the main shutter in interrrupting all e-beams. The substrates were loaded into Molybdenum holders where the substrates were held by gravity alone, this allowed for low incident angle for the RHEED measurements.
The system is equipped with two electron beam guns for source evaporation. The electron beam generated by each e-gun was controlled by a sweeper mechanism, which allowed the electron beam characteristics to be adjusted. This allowed the frequency at which the electron beam swept the relevant crucible to be controlled

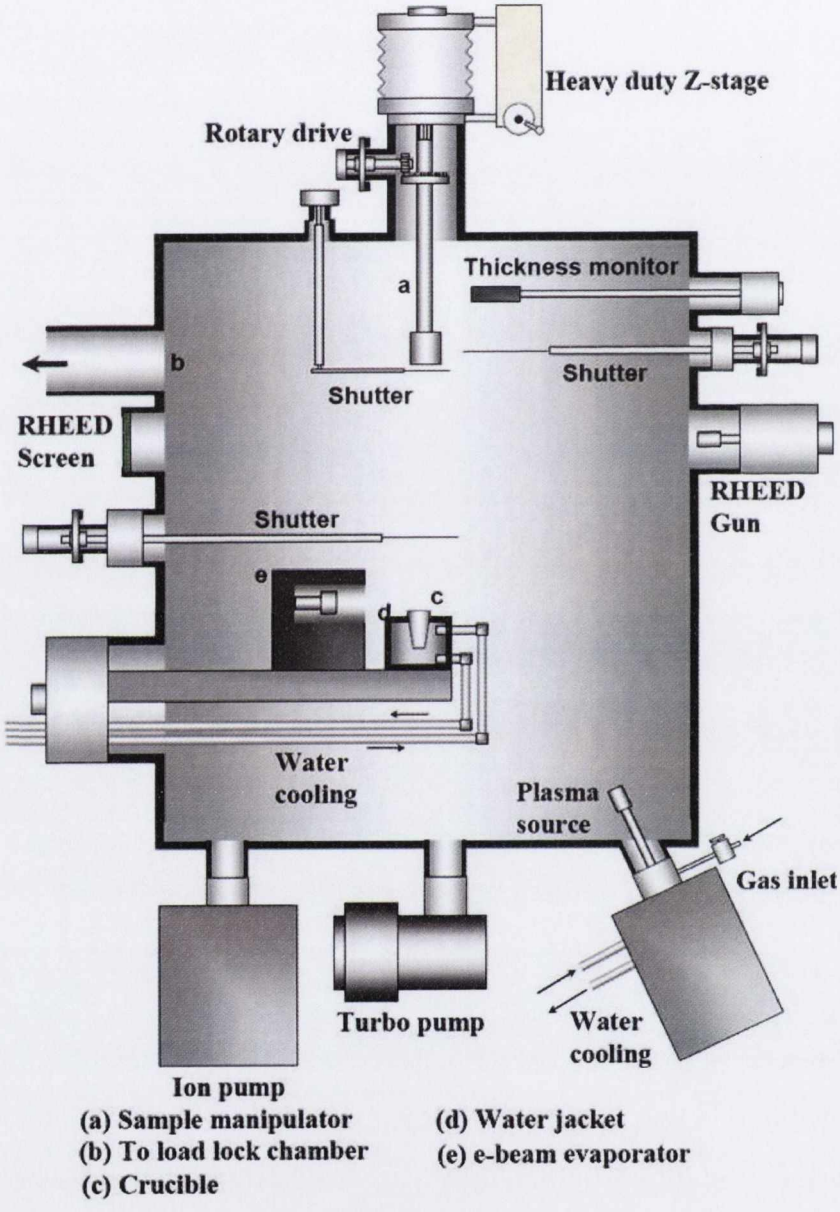

Figure 4.2: Schematic drawing of the molecular beam epitaxy system used

along with the X- and Y-axis travel of the beam over the crucible surface. This was achieved by controlling the voltage applied to plates within the e-gun architecture, thus controlling the deflection of the electron beam. The relevant values were adjusted using a separate, handheld control panel. When the sweeper functionality was in an off position the electron beam fell on only one point of the crucible.

The e-gun power and hence the deposition rates were monitored and controlled using an INFICON IC/5 deposition rate controller. The deposition rate could also be controlled using the sweeper module, by adjusting the area upon which the eletron beam fell, although this method was not employed and the electron beam was set to sweep the entire crucible surface to obtain a more uniform heating of the source material and minimise the effect of local hot spots. Each e-gun had a port associated with it to house a quartz crystal monitor head, which were positioned in such a way that they were shielded from other sources. Furthermore, each crystal monitor head had its own shutter mechanism which, when used correctly, acted to prolong the lifetime of the monitor head. Each e-gun also had an associated shutter positioned over the relevant crucible evaporation position. This shutter acted to allow material to impact on the crystal monitor head but not on the substrate.

The shutter system was a linear electro-pneumatic shutter system. Operation was controlled using Festo controllers which allow for easy adjustment of the shutter motion via adjustable pressure valves. The shutters were run in soft-mode to minimise vibrations and flake fallings.

The electron gun area was separated from the main body of the deposition chamber by a water cooled roof. The lower part of the deposition chamber was fitted with a water cooled shroud that effectively separated the growth area from the e-guns. The source positions were separated from each other with double wall

Mo beam separator plates. These plates were in good thermal contact with the water panel and the double walled design effectively prevented any thermal or chemical cross talk between different sources.
The pumping system consisted of a VARIAN Triode ion pump with a pumping speed of 500 ls^{-1}, a VARIAN V1000 1000 ls^{-1} turbo pump and a VARIAN Tri Scroll 600 dry scroll vacuum pump. This pumping system allowed pressures of the order of 7 x 10^{-10} mbar to be achieved in the deposition chamber.

4.2.1.1 Plasma source

The system was fitted with an Oxford Scientific OSPrey Plasma Source set to operate in Atomic Mode. The specially designed aperture plate inhibits ions from escaping from the plasma, yet allows reactive neutrals to escape and form the dominant beam fraction. The emitted particles are largely thermalised through multiple collisions on passing through the aperture. Microwaves with a frequency of 2.45 GHz were generated by a microwave magnetron operating at a magnetron power of 10-250 W. The microwaves were then coupled through a resonant coupler into a coaxial feed-through structure which guided the microwaves into the vacuum and up into the plasma chamber. The plasma was excited in this chamber and the microwaves absorbed. The plasma was confined to this chamber. Further enhancement of the plasma density was provided by a magnetic quadrupole arranged around the discharge chamber which generates an 87 mT field inside the plasma. At this field strength electrons in a 2.45 GHz microwave field undergo electron cyclotron resonance motion. The spirally motion greatly enhanced the electron path length and therefore the probability of collisions leading to the creation of ions was increased. The open end of the plasma chamber was fitted with aperture plates with a number of small holes. These acted to reduce the number of ions leaving the plasma chamber thus effectively reducing the ion current. The

beam leaving the plasma chamber consisted mainly of molecular and atomic particles. In this manner molecular oxygen (O_2) was converted into atomic oxygen and subsequently introduced into the deposition chamber. The atomic oxygen impinged on the surface of the substrate and in such a manner thin film metallic oxides were deposited.

4.2.2 Reflection High Energy Electron Diffraction

Reflection high energy electron diffraction (RHEED) is one of the most important in situ sample characterization tools for the crystal structure and the thickness of the film [10, 11, 12]. In comparison to other diffraction methods, the glancing-incidence-angle geometry of RHEED offers many advantages, such as high surface sensitivity and in situ compatibility with crystal growth.

In a typical RHEED system a high energy electron beam (10-50 keV) arrives at a sample surface under grazing incident angle (0.1-5 degree). At such high energies the electrons can penetrate any material for several hundreds of nanometers. However, due to a grazing angle of incidence, the electrons only interact with the topmost layer of atoms (1-2 nm) at the surface which makes the technique very surface sensitive. The scattered electrons collected on a phosphorus screen form a diffraction pattern characteristic for the crystal structure of the surface and also contains information about the morphology of the surface (see Figure 4.3). The main reasons for the popularity of RHEED are accessibility of the sample during the deposition in relatively high pressure enviroment and the observation of intensity oscillation of the specular spot during deposition which allows determination of growth rate and growth mode. [13] In the following section a description of the basic principles of RHEED is provided.

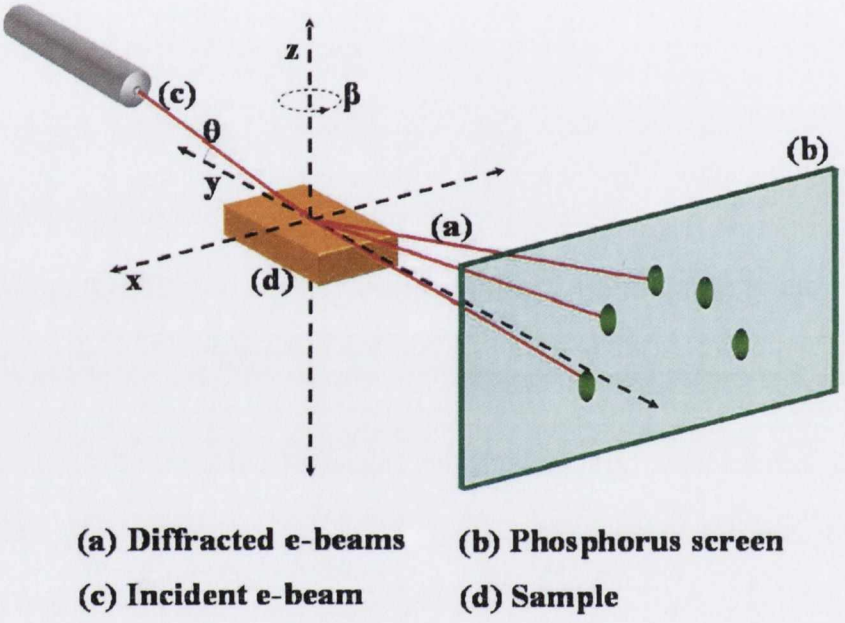

Figure 4.3: Schematic of the RHEED

4.2.2.1 Basic principles of RHEED

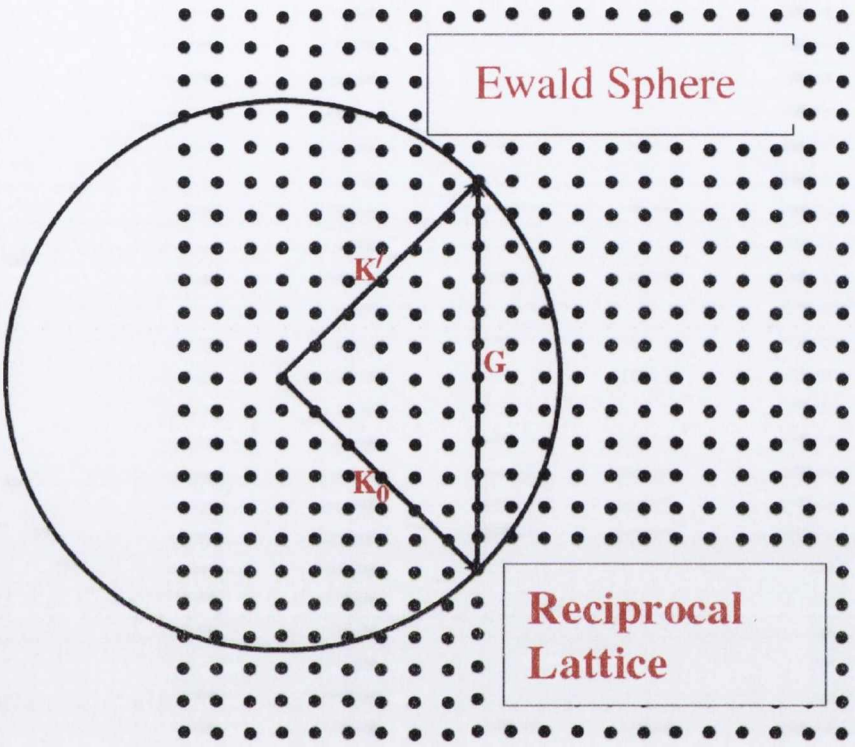

Figure 4.4: Ewald sphere of radius k_0

In kinematical scattering therory, the possible reflections are determined by the condition that the wavevectors of the incident ($\vec{k_0}$) and diffracted ($\vec{k'}$) differ by a reciprocal-lattice vector $\vec{G}$:

$$\vec{k'} - \vec{k_0} = \vec{G} \tag{4.1}$$

In the case of elastic scattering, this means that $|\vec{k'}| = |\vec{k_0}|$, this diffraction condition can be better understood by inspection of the Ewald sphere, in this construction the tip of $\vec{k_0}$ is attached to a reciprocal lattice point. The sphere around the origin of $\vec{k_0}$ with radius $|\vec{k_0}|$ defines the Edwald sphere, see Figure 4.4. Reflections

can occur for all $\vec{k'}$ connecting the origin of the sphere and a reciprocal lattice point of the sphere.

The magnitude of the wavevector for high energy electrons is given by:

$$k_0 = \frac{1}{\hbar}\sqrt{2m_0 E} \tag{4.2}$$

where the relativistic correction term is not considered, since it only amounts for about 3 % for 20 keV electrons. In RHEED, the Ewald sphere is large; for 20 keV electrons k_0 is 785 nm^{-1}, which is more than 20 times larger than the reciprocal lattice unit of MgO ($\sim$ 30 nm^{-1}), producing an almost planar cut through the first few Brillouin zones of the reciprocal lattice.

RHEED is very surface-sensitive in that it samples only very few atomic layers beneath the surface. The surface normal component $\vec{k_{0z}}$ of the incident wave vector which determines the penetration into the material can be carried over a large range of values by changing the incident angle θ. For low incident angles the sampling depth of RHEED can be very small. This implies that the periodic part of the crystal beneath the surface can usually be neglected and therefore we can approximate the sampled volume in the reciprocal lattice by a two dimensional layer. The reciprocal lattice then degenerates into a set of one-dimensional rods along the z direciton perpendicular to the surface. Using this reciprocal lattice, we get the Ewald sphere construction used in RHEED (Figure 4.5). Since the reciprocal lattice consists of continuous rods, every rod produces a reflection in the diffraction pattern as shown in the Figure 4.5.

The reflections occur on so-called Laue circles of radius L_n cantered at H the projection of the component parallel to the surface k_0 onto the screen. The specular reflection or specular spot S is located at the intersection of the zeroth-order Laue circle with the (00) rod. The origin of the reciprocal lattice is projected on to I, where for some sample geometries the part of the incident beam that

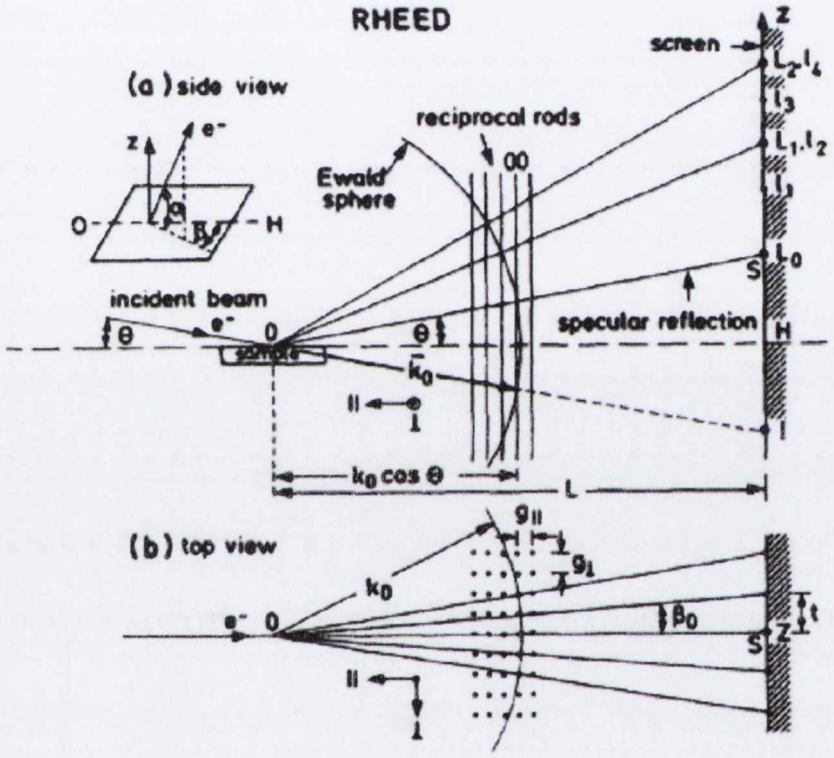

Figure 4.5: Schematic of the RHEED diffraction geometry. (a) Side view of intersections of Ewald sphere with the reciprocal lattice rods. (b) Projection of the Ewald sphere on a plane parallel to the sample surface. Reproduced from [14]

misses the sample becomes visible. [10] A quantitative method to determine the lattice constant of the sample from the RHEED pattern is given by Hernandez-Calderon et al [14]. In a typical RHEED experiment with an electron wave vector $\vec{k}_0 \sim 10^3$ nm^{-1} and a reciprocal surface vector $\vec{g}$, the characteristic value of $\frac{|\vec{g}|}{|\vec{k}_0|} \sim 10^{-2}$. This means that the Ewald sphere will touch a few rods at both sides of the (00) rod (Figure 4.5(b)). The angles between these reflections will practically be the same and are given by

$$\beta_0 = tan^{-1}[\frac{g_\perp}{\sqrt{(k_0^2 - g_\perp^2)}}] = tan^{-1}(\frac{t}{L}) \tag{4.3}$$

where t is the distance between streaks and L is the sample-to-screen distance. Since $g_\perp = 2\pi/d_\parallel$, where $d_\parallel$ is the distance between equivalent rows of atoms parallel to the incident beam and $g_\perp \ll k_0$ and $k_0 = 2\pi/\lambda_0$, the relation

$$d_\parallel t = L\lambda_0 \tag{4.4}$$

is obtained from Equation 4.3, where λ_0 is the wavelength of the electron in the relativistic approximation. For a fixed electron beam energy and geometry configuration, the parameter $L\lambda_0$ can be calibrated with a sample whose lattice constant is well known. In this way a precision in the determination of lattice constants of 10^{-3} can be easily obtained.

The intensity of specular spot in the RHEED pattern generally exhibits very regular oscillations as a function of time, under the growth conditions that lead to layer-by-layer growth [15, 16, 17, 18]. In the layer-by-layer growth mode one layer is essentially completed before material is added to the following layer. This periodic variation of the surface morphology is the reason for RHEED oscillations. The intensity of the specular spot of the clean substrate is maximum when deposition starts, islands are formed on the surface resulting in an increase of the roughness and a corresponding decrease in intensity due to diffuse scattering [19].

After the completion of one monolayer the surface is again smooth and the intensity increases. RHEED oscillations are used to determine growth rates, layer thicknesses and alloy compositions [18]. For Fe_3O_4 one monolayer corresponds to a quarter of the unit cell which is 0.21 nm. when the oscillation period is known, the thickness of the film can be calculated accurately from the deposition time. The RHEED images obtained for a vicinal surface show distinct features when beam directed along the step edges and perpendicular to the step edges. In the first case RHEED images shows vertical lattice rods and sharp Kikuchi lines are observed, while in the second case RHEED images show sharp horizontal Kikuchi lines which are not oberved in the first case. This is because of the increased inelastic scattering due to the presence of atomic steps. The horizontal Kikuchi lines are generally slightly tilted with respect to the shadow edge due to the miscut of the sample surface.

4.2.2.2 Instrumentation details of RHEED on the MBE system

The MBE deposition chamber was fitted with a Staib Instrumente Reflection High Energy Electron Diffraction (RHEED) RH 30 system. The system consisted of an electron gun (e-gun) fitted to one of the spare radial deposition chamber ports and a phosphor screen located diagonally across from the e-gun. A digital camera was mounted behind the screen to capture the RHEED images. the electron beam source and detector, effectively the e-gun and the phosphor screen, were located along the same axis as was required for the proper operation of the RHEED system. The RHEED system was capable of working in UHV and also in a vacum of the order of 7 x 10^{-5} mbar, though at this pressure the RHEED electron gun (e-gun) was pumped under a differential arrangement by the load-lock turbo pump. This was done in order to prevent oxidation of the RHEED e-gun element. Specifics of the RHEED system included:

- a small focus spot (< 100 μm)
- the beam size remains constant even over large working areas
- a small beam divergence (under 0.2 mrad) could be obtained.

The RHEED system was equipped with an electron optical system specially designed for RHEED applications, i.e. it was equipped with an electron optical diaphragm system thus producing as shallow angle electron beam as possible. For all RHEED images presented in this work the RHEED system was operated at a voltage of 20 kV and a filament current of 1.6 A. It must be noted that due to the effect of the e-gun sweeper fields on the RHEED electron beam, the quality of the images obtained during growth will be compromised, for this reason images were usually taken only after completion of the deposition. To complete a RHEED analysis the substrate had to be rotated to ensure the correct crystal orientation was presented to the electron beam. This was achieved by rotating the substrate manipulator through pre-defined angles in order to present the <110> and the <100> directions to the electron beam.

4.3 Ex-situ sample characterization

4.3.1 High resolution X-ray diffraction

The high resolution X-ray diffraction (HRXRD) is a key characterization tool in the area of thin film growth, it provides nondestructive ex-situ information of the characteristics of epitaxial layers of heterostructures and superlattice systems. Parameters such as composition, uniformity and thickness of epitaxial layers can be obtained, as well as the built in strain and relaxation. Below we provide a brief description of this technique and the instrumentation used.

4.3.1.1 Basic principles of HRXRD

The lattice spacing of a crystal can be determined by Bragg's law:

$$d_{hkl} = \frac{n\lambda}{2sin\theta} \tag{4.5}$$

where d_{hkl} is the spacing of lattice planes with Miller indices (hkl), θ is the corresponding Bragg angle, λ the wavelength of the X-ray used, and n is an integer which represents the order of diffraction.

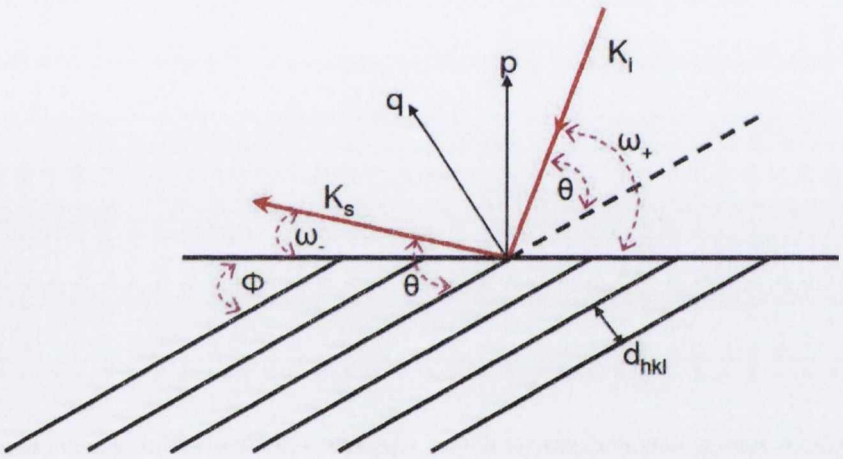

Figure 4.6: Scattering geometry of X-rays probing a plane having an interplanar angle ϕ with the surface plane.

In Figure 4.6 the scattering geometry is shown. ϕ denotes the angle between the lattice plane (hkl) and the surface, K_i and K_s are the incident and the scattered vectors, respectively. p is the surface normal and q is the normal on reflecting planes. ω_+ is the angle between the surface plane and incident wavevector whereas ω_- is the angle between the surface plane and scattered wavevector. ω_+ is referred to as ω here after.

In epitaxial systems typically lattice constants variations $(\Delta d/d)$ between 10^{-2} to

10^{-4} have to be measured. The corresponding angular changes $\Delta\theta$ in the Bragg angle follow from the differentiation of Bragg's law (Equation 4.5) as

$$\frac{\Delta d}{d} = \frac{\Delta\lambda}{\lambda} - \frac{\Delta\theta}{tan\theta} \tag{4.6}$$

It is clear from Equation 4.6 that for high precision measurements of lattice constants the wave length spread $\Delta\lambda$ has to be minimised and to achieve this, the simple powder diffractometers using a focussing path for the X-Rays are replaced by double and triple axis spectrometers equipped with multiple crystal or channel cut monochromators and analyzers. In a double axis spectrometer two crystals are used. The first one is often a dislocation free Ge or Si crystal, used as the beam conditioner. The second one is the sample to be investigated. In a triple-axis spectrometer apart from the beam conditioner and sample crystal, channel cut crystal is used as an analyser. The advantages of the triple-axis spectrometer are the following:

- Improved angular resolution permits the observation of weak diffraction satellites.
- The triple-axis diffractometer allows Bragg plane tilts and dilatations to be determined independently.
- Diffuse scattering can be easily be separated from coherent Bragg scattering.

The disadvantage of triple axis in comparison with double-axis spectrometer is that the analyser crystals reduce the intensity, resulting in longer measurement times. In triple-axis mode the difficulty of the adjustment procedure is higher compared to the double-axis.

4.3.1.2 X-ray reflectivity

X-ray reflectivity (XRR) is a non-destructive technique, used for estimation of density, thickness and roughness of thin film structures. Basically it consists in the measurement of the reflected intensity of X-rays from a sample surface near glancing incidence [20]. In this study, it was used to measure the thickness of the thin films. Typical scattering geometry is shown in Figure 4.7. The incident angle is equal to the reflected angle and is usually less than 6°.

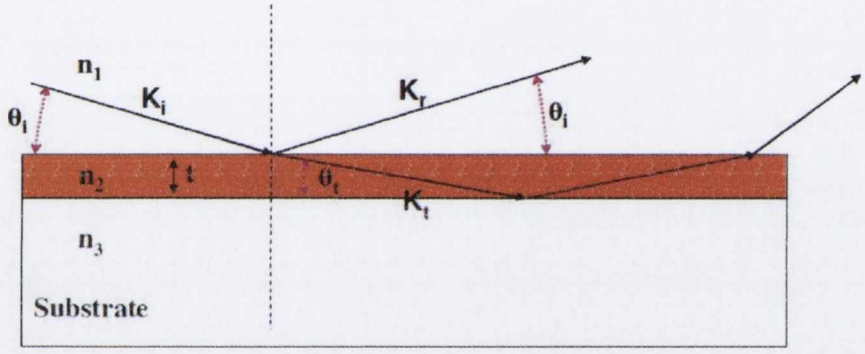

Figure 4.7: Scattering geometry of specular reflection of X-rays in the thin film and substrate.

At X-ray frequencies the refractive index of a medium can be expressed as [20]:

$$n = 1 - \delta - i\beta \tag{4.7}$$

where δ and β are the dispersion and absorption terms. The real part of refractive index n, 1-δ, is connected to the phase-lag of the propagating wave and the imaginary part, β, corresponds to the decrease of the wave amplitude, δ and β are small positive quantities of the order 10^{-5} to 10^{-7} for X-ray wavelengths at about 0.15 nm [21].

Therefore from Equation 4.7 it is clear that the refractive index is slightly less than 1 and from Snell's law [22], there will be a critical angle (θ_c).
The critical angle θ_c is the angle at which X-ray will undergo total internal reflection when propagating from a medium of high refractive index to a medium of low refractive index. Considering the case of an absorption free film ($\beta = 0$) and air (n_1=1) interface, the X-ray critical angle is given by:

$$cos\theta_c = n_2 = 1 - \delta \tag{4.8}$$

For angles greater than θ_c the X-ray beam penetrates the film and reflection occurs at the top and the bottom surfaces of the film. The interference between the rays reflected from the top and the bottom of the film results in interference fringes as shown in Figure 4.8 for a 60 nm film.
The relation between the thickness of the film (t) and intensity maxima positions

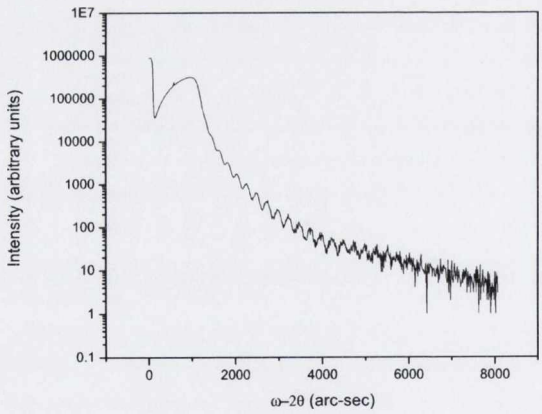

Figure 4.8: Reflectivity scan of Fe_3O_4 film on MgO(100).

θ_m is given by [21]

$$\frac{1}{2}(2m+1)\lambda = 2t\sqrt{\theta_m^2 - 2\delta} \tag{4.9}$$

$$\frac{1}{2}(2m+1)\lambda = 2t\sqrt{\theta_m^2 - 2\theta_c^2} \tag{4.10}$$

where m is an integer. Considering two neighbouring m and m+1 maxima and employing Equation 4.9 we obtain:

$$t = \frac{\lambda}{2}[\frac{1}{\theta_{m+1} - \theta_m}] = \frac{\lambda}{2}\frac{1}{\Delta\theta_m} \tag{4.11}$$

where $\Delta\theta_m$ is the fringe spacing obtained from intensity oscillation during the reflectivity measurements. The thickness is often determined with a precision better than 0.1 nm. From X-ray reflectivity mesurements we can also obtain information about the roughness and density of the grown layers.

4.3.1.3 Tilt analysis of miscut angle measurement

The tilt or miscut angle of the sample can be measured using HRXRD. Because of the miscut, the ω positions at which diffraction is found vary as the specimen is rotated about its surface normal (azimuth rotation ϕ). If we perform a symmetric scan ideally ω is half of $2\theta_s$ value, but for vicinal substrates with a miscut angle α it can be $\theta_s \pm \alpha$. The two extreme cases are as follows; $\omega = \theta_s + \alpha$ is the case when miscut minimum is facing the incident beam or the incident beam is in the step up direction as shown in Figure 4.9(a) and $\omega = \theta_s - \alpha$ is in the case when miscut maximum is facing the incident beam or incident beam is in the step down direction as shown in Figure 4.9. In general the dependence of the diffraction angle on the azimuth can be written as:

$$\omega = \omega_0 + \alpha cos(\phi + offset) \tag{4.12}$$

whre α is the miscut of the substrate and "offset" gives the direction of miscut.

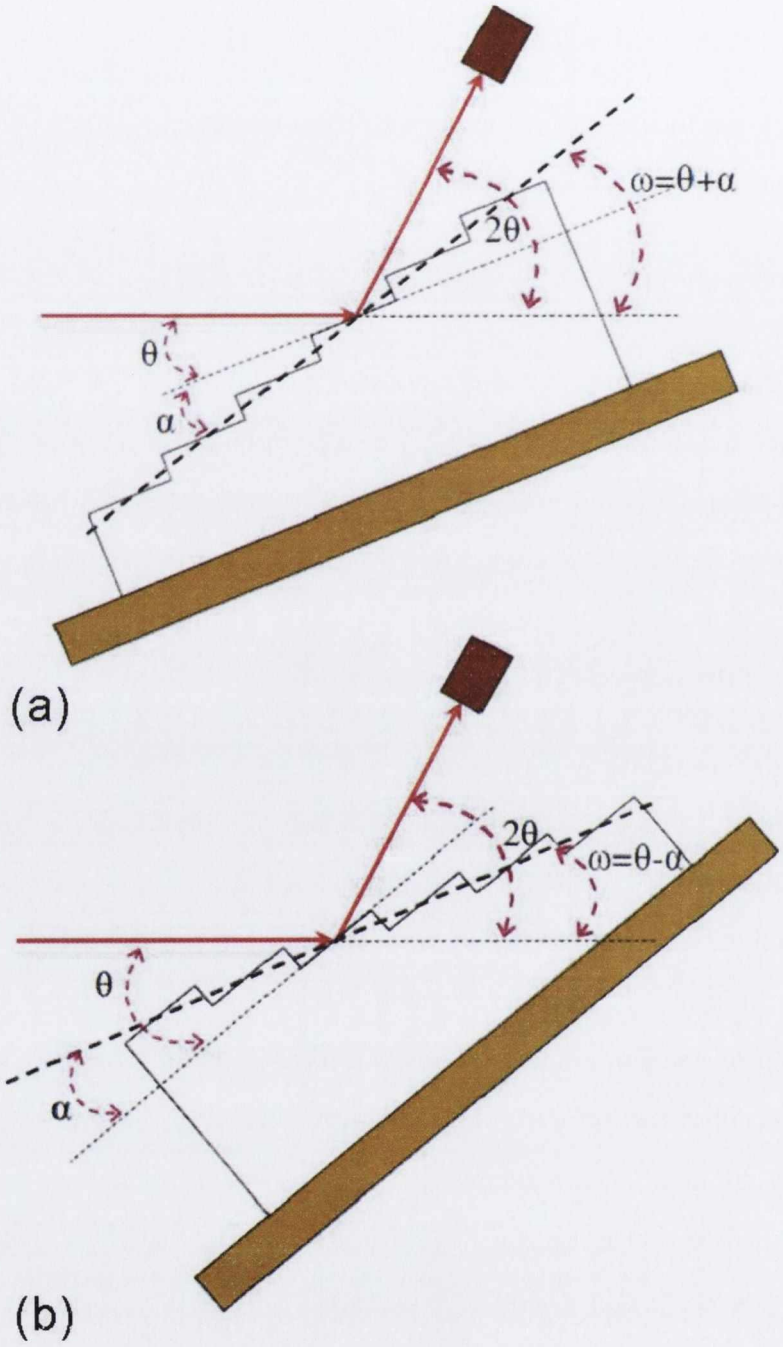

Figure 4.9: Schematic of the diffraction geometry for a vicinal surface.(a) and (b) shows symmetric diffraction when miscut minimum facing the incident beam and when miscut maximum facing the incident beam respectively.

4.3.1.4 Instrumentation details of HRXRD

The high resolution x-ray difractometer used to perform all of the high resolution x-ray diffraction (HRXRD) and x-ray reflectivity measurements in this work was a Bede D1 diffractometer. The source or beam stage was fixed to the system housing and comprised all the beam conditioning mechanisms and the related optics required to ensure a homogeneous X-ray beam of small angular dispersion. A channel cut crystal acted as the beam conditioner in front of the X-ray source. With correct optimisation of the source stage optics a sub-millimeter beam could be achieved that maintained its integrity over long distances ($\sim$ 150 cm). The X-rays were produced from a Cu Kα1 transition and had a wavelength of 0.15406 nm.

4.3.2 Magnetization measurements

Among the several methods available to study the magnetization behavior of magnetic materials, in the present work we performed measurements of the magnetic moment of the samples using a vibrating sample magnetometer (VSM) [23] and a alternating gradient field magnetometer (AGFM). We provide a brief description of their operation below.

4.3.2.1 Vibrating sample magnetometry

This instrument is credited to S. Foner[23]. Its working principle is based on the flux change in a coil when a magnetized sample is vibrated near it (see Figure 4.10 for a schematic). The oscillating magnetic field of the moving sample induces an alternating electromotive force in the detection coils, whose magnitude is proportional to the magnetic moment of the sample. The induced voltage can

be described by the following equation:

$$V_{coil} = \frac{d\Phi}{dt} = \frac{d\Phi}{dz}\frac{dz}{dt} \tag{4.13}$$

In equation 4.13, Φ is the magnetic flux enclosed by the pickup coil, and t is time. For a sinusoidally oscilating sample, the voltage is based on the following equation:

$$V_{coil} = 2\pi f C m A sin(2\pi f t) \tag{4.14}$$

where C is a coupling constant, m is the DC magnetic moment of the sample, A is the amplitude of oscillation, and f is the frequency of oscillation.

The acquisition of magnetic moment measurements involves measuring the co-

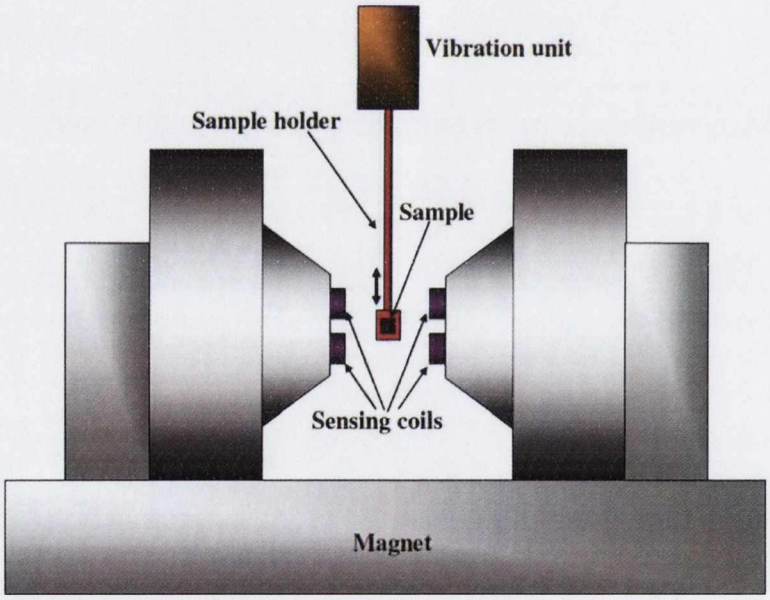

Figure 4.10: Schematic of vibrating sample magnetometer or VSM

efficient of the sinusoidal voltage response from the detection coil. The sample is attached to the end of a sample rod that is driven sinusoidally. The center of

oscillation is positioned at the vertical center of a gradiometer pickup coil.
The setup used in this research work was a Princeton Measurements Corp. Model 3900 MicroMag Vibrating Sample Magnetometer, which has a sensitivity of 1 μemu (or 10^{-9} A/m^2) at an averaging time of 1 s per point. The applied field is continuously monitored by a built-in Hall-effect gaussmeter, which provides feedback for a precise control in both field sweep and static mode conditions. It is equipped with a low temperature cryostat and high-temperature oven which enables the measurement in all temperature range from 10 K to 1023 K.

4.3.2.2 Alternating gradient field magnetometry

In this technique, the sample is mounted at the end of a fiber and subjected to a fixed dc field plus an alternating field gradient, produced by a coil pair (see Fig. 4.11. This gradient produces an alternating force on the sample, which oscilates and causes the flexion of a fiber. If the vibration frequency is tuned to a resonant frequency of the system, the vibration amplitude increases by a factor equal to the quality factor of the vibrating system. A piezoelectric crystal is usually used to generate a voltage proportional to the vibration amplitude, [24] which in turn is proportional to the sample moment.
The AGFM is more limited than the VSM in the maximum mass of the sample that can be measured, and tuning the vibration frequency to resonance complicates the measurement. The necessary presence of a field gradient means the sample is never in a completely uniform field, which can be a limitation.
The setup used in this research work was a Princeton Measurements Corp. Model 2900 MicroMag Alternating Gradient Force Magnetometer, which has a sensitivity of 1 nemu (or 10^{-11} A/m^2) at an averaging time of 1 s per point. The applied field is continuously monitored by a built-in Hall-effect gaussmeter, which provides feedback for a precise control in both field sweep and static mode conditions.

It is equipped with a low temperature cryostat and high-temperature oven which enables the measurement in all temperature range from 10 K to 1023 K.

The calibration of the VSM/AGFM system was done with a Standard Reference

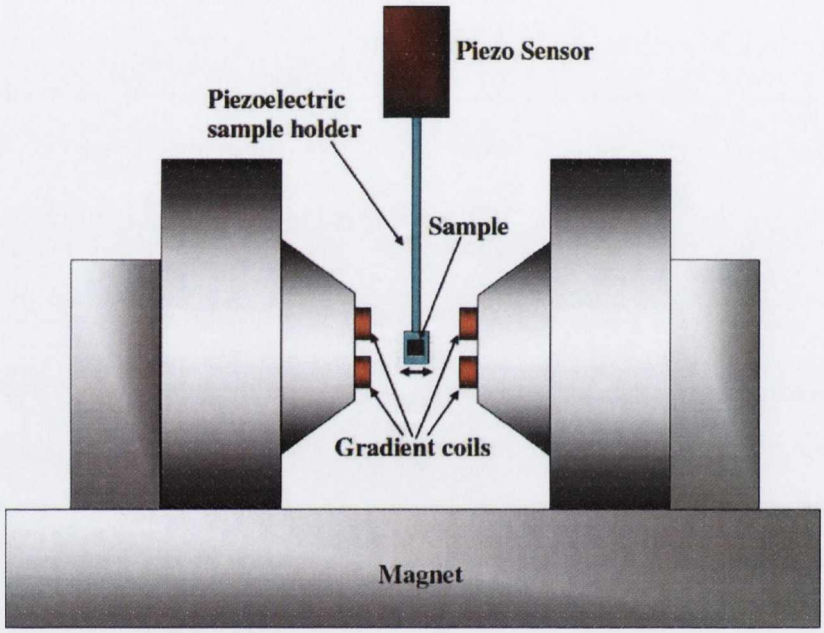

Figure 4.11: Schematic of alternating gradient force magnetometer or AGFM

Material® (SRM) 2853 Magnetic Moment Standards and Technology (NIST).

4.3.3 Electrical properties measurements

4.3.3.1 Physical property measurement system

The measurements were performed using a Physical Property Measurement System (PPMS 6000 system of Quantum Design). The PPMS consists of a helium cooled cryostat which is pumped by a rotary pump in which the sample can be placed and the temperature can be varied between 2 K and 400 K. Although

in this study the minimum temperature at which measurements were performed was 80 K. The system is equipped with a 14 T superconductor magnet with a field uniformity of ± 0.1 % over 5.5 cm. The resolution of the magnet is 0.03 mT to 1.5 Tesla and 0.3 mT up to 14 T. The sample temperature is controlled with a stability of ± 0.2 % and is monitored by a platinum resistance thermometer (PT-100) with an accuracy of ± 1 % from zero to full field. The PPMS 6000 system is also equipped with a motorized sample rotator to conduct the angular dependence measurements (see figure 4.12). Samples are mounted on removable platforms. The rotator can sweep the angular range from -10 to 370, with the step size of 0.053° for standard resolution.

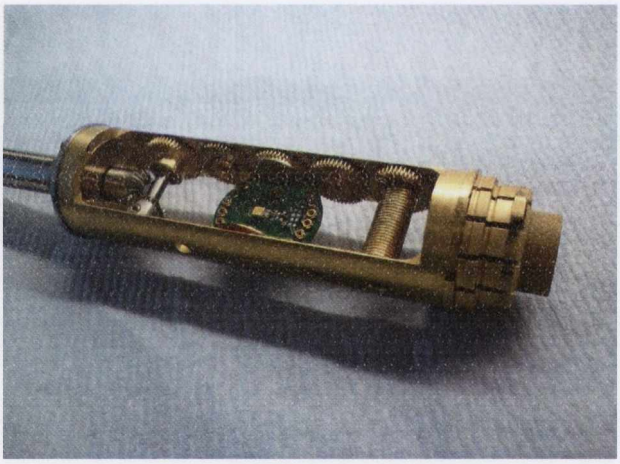

Figure 4.12: Sample rotator used for the angular dependence measurements of magnetoresistance.

4.3.3.2 Magnetic field control

A superconducting magnet was used to produce field of up to 14 T in our PPMS system. The advantages of superconducting magnets are: [25]

- No electric power is needed to sustain a constant magnetic field.

- No Joule heat is generated, so that no provision is necessary to remove heat from the coil, except for liquid helium which is used to keep the coil in a superconducting state.

- It is possible to keep the field completely time-independent by short-circuiting the coil with a superconducting shunt. This is known as persistent current or persistent-mode operation.

The disadvantages of superconducting coils are:

- They require cooling with liquid helium.

- If the maximum field is exceeded, the magnet 'quenches' from the superconducting state with the rapid generation of heat which very quickly evaporates liquid helium.

- The uniformity of the field is perturbed by persistent eddy currents in the superconductors.

- When the field is changed, there can be sudden irregular small changes in field intensity caused by 'flux jumps'.

The essential process to charge and discharge the PPMS superconducting magnet is as follows:

- The Model 6700 Magnet Controller matches the current in the magnet.

- A small portion of the superconducting magnet wire (the persistence switch) is heated by another resistive wire.

- The heated persistence switch becomes non-superconducting, which switches the magnet controller into the previously closed superconducting circuit.

- The magnet controller drives the magnet to the current that is necessary for the new field.

The persistence switch heater is generally turned off after the field set point is reached, allowing the entire magnet to superconduct again. The magnet is in Persistent mode when the persistence switch is superconducting. In Persistent mode, the current in the magnet does not dissipate, so the power supply current can be turned off. The magnet can also be operated in Driven mode, which retains the current source in the magnet circuit in order to drive the current. The field in the sample space is a known function of the current in the magnet. To ensure that the proper field exists in the magnet during magnet charging and discharging, the current from the power supply is passed through one of two calibrated resistors in the Model 6700 (magnet control module) before the persistence switch heater is turned off. The two resistors are for high-power and low-power operation, and the appropriate resistor is used for each current. The voltage drop across the resistor is directly proportional to the current in the magnet and thus proportional to the field within the sample space. The field is calculated from this potential drop and if the field is not within a certain range of the field set point, the magnet current is adjusted accordingly until the field is within the acceptable range. For the 14 Tesla magnet, the field must be within about 0.3 mT of the set point for set points above about 1.5 T, and the field must be within about 0.03 mT of the set point for set points below 1.5 T before the persistence switch heater is turned off. The field that is reported is calculated from the drop across the resistor. The temperature coefficient of the calibration resistors in the Model 6700 is nominally 30 ppm/°C, so variations in the temperature of the instrument might have very small effects on the reported field. It is important to note that the field reported by the PPMS is only that due to the current through the magnet circuit, the reported field value does not account for any background sources or remnant field

in the magnet, therefore this has to be taken into consideration when measuring small fields. The value remnant field in the magnet after application of a field of 5 Tesla is 0.008 T.

4.3.3.3 Closed cycle refrigeration (CCR) system

The DC resistivity of the sample can also be measured with a HP 34401A Multimeter, in the standard four probe configuration. Electrical contacts were made on the sample using quick drying silver paint (Agar scientific, Batch number 0294) and 0.075 mm thin silver wire. The silver paint was diluted in Iso-Butyl-Methyl-Ketone (Agar scientific, Batch number R1272). The low temperature measurements were carried out using a closed cycle refrigeration (CCR) system (CTI-Cryogenics 8200 Compressor). A schematic of the CCR system is shown in Fiure 4.13, the system requires no liquid helium or liquid nitrogen as a source of cooling. A closed loop of helium gas is compressed and expanded, during the expansion phase of each cycle, heat is removed from the cold finger, on which the sample is mounted.

The temperature of the sample is controlled by a Lake Shore 330 Temperature Controller, which varied the current in the heating wires wound near to the sample, to counter the cooling effect of the compressed helium from the compressor. The temperature of the sample stage was monitored using a GaAlAs thermometer with an accuracy of $\pm$ 0.05 K. The temperature range attained with this system was from 30 K to 300 K.

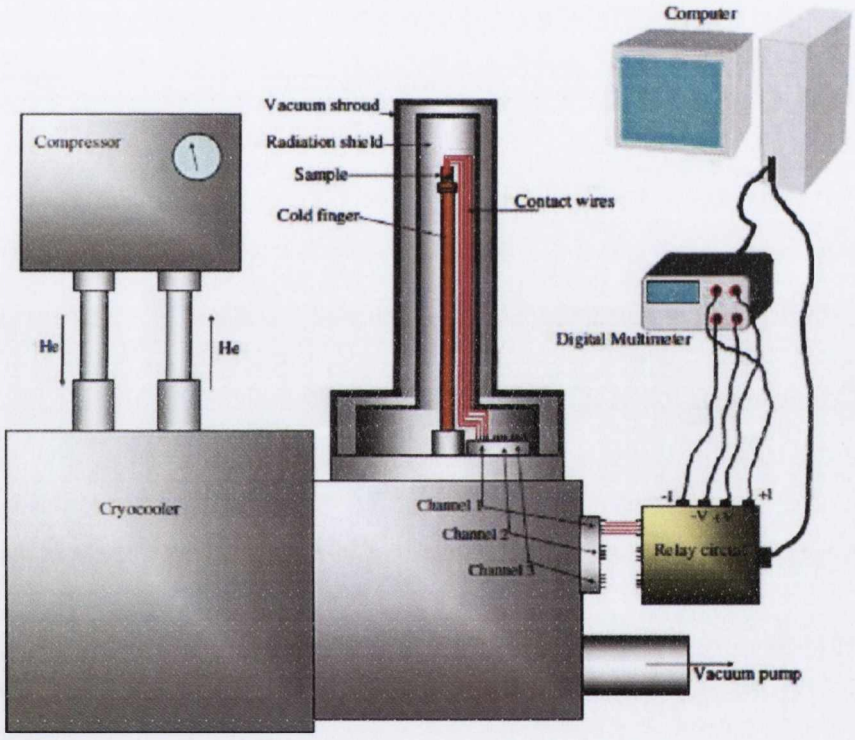

Figure 4.13: Schematic of the CCR system.

4.4 Lithography techniques

Microlithography and nanolithography usually refers to the lithographic patterning methods capable of structuring material on a fine scale. [26] The basic steps (see Figure 4.14) of a typical lithography process are described as follows: [27]

- **Sample preparation**: Samples are solvent cleaned with isopropanol to remove any contamination of the surface.
- **Spin coating**: The sample is then coated with the liquid resist material. Different resists require different spin coating conditions, such as a initial slow spin followed by a ramp up to the final required rotational speed. Some important quality measures for resist application are time, speed, thickness, uniformity, particulate contamination, and resists defects such as pinholes.
- **Exposure**: This step involves the exposure of the resist to UV light or electron beam to obtain the desired design. Positive photoresist, becomes soluble in the basic developer when exposed; negative photoresist becomes insoluble in the developer.The methods of exposure are described below.
- **Developing**: This step creates the pattern in the resists on the sample surface. The soluble areas of the resist are dissolved by liquid developer chemicals.
- **Etching**: a liquid ("wet ") or plasma ("dry ") chemical agent removes the uppermost layer of the substrate in the areas that are not protected by the resist, transfering the desired pattern to the sample.
- **Lift-Off**: The target material is deposited over the whole area of the wafer, reaching the surface of the substrate in the etched regions and staying on the top of the resist in the regions that where not developed. When the resist

is washed away, the material on the top is lifted-off and washed together with it. After the lift-off, the target material remains only in the regions where it had a direct contact with the substrate.

- **Resist removal**: After the etching or lift-off the photoresist is no longer needed and it must be removed from the substrate. This usually requires a liquid "resist stripper", which chemically alters the resist so that it no longer adheres to the substrate.

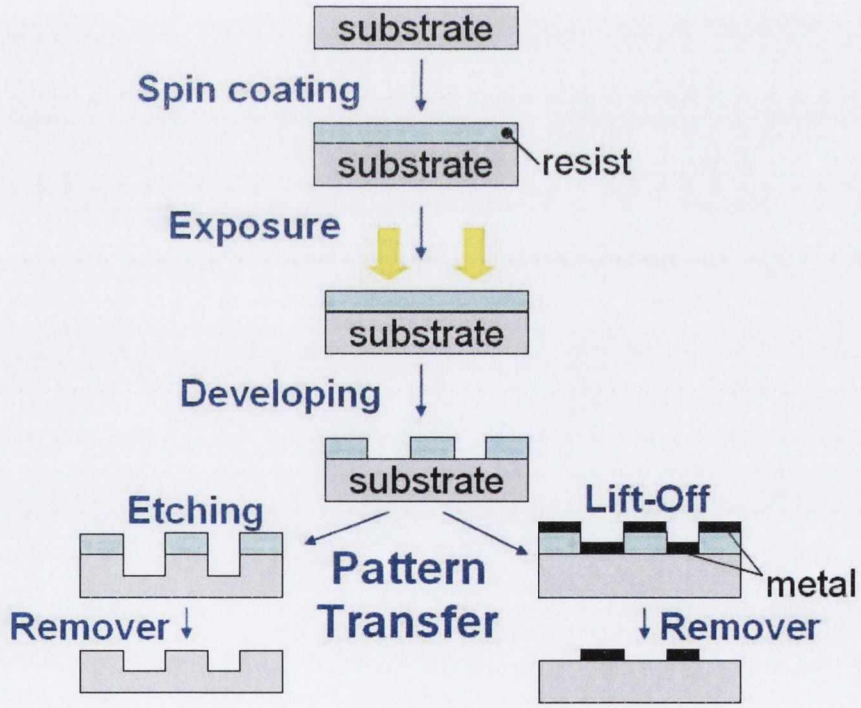

Figure 4.14: Schematic of the steps followed in a lithography process.

4.4.1 Exposure methods

4.4.1.1 UV-lithography

The UV-lithography technique was used in order to fabricate the micrometer size hall bars and to deposit the contacts on the nano-structures. The overall concept of UV lithography is quite simple, as the name implies UV light is shinned through a mask onto a photoresist covered wafer. The mask stops some of the light from proceeding onto the resist covered surface. The mask aligner used is a Karl Suss MJB-3 UV400, which has capability for exposing wafers up to 3 inches in diameter. The wafer sits on a movable chuck that can be moved for alignment of existing patterns on the wafer. The light source is a 350 W multi-wavelength mercury arc lamp calibrated at 23 mW/cm^2 (mJ/s) measured for h-Line (405 nm). The exposures were always performed in soft contact mode, which means that contact between sample and mask is only given by mechanical force. The resolution of the apparatus in this mode is about 2-3 μm.

4.4.1.2 Electron beam lithography (EBL)

Electron beam lithography was carried with a scanning electron microscope (SEM) equiped with a Raith50 electron lithography tool. The microscope is a field emission scanning electron microscope (SUPRA40, Carl Zeiss). The beam generator is a thermal field emission tip (Schottky-emitter) which consists of a finely etched <100> oriented tungsten crystal tip, with a sintered reservoir of zirconium oxide in the shank. The tip is heated to aproximately 1800 K by the filament bake out current. The microscope has an imaging resolution of 1.3 nm at 15 kV, with a magnification factor ranging from 12 to 9 x 10^5. The acceleration voltage can be set from 0.2 to 30 kV with a probe current ranging from 4 pA to 10 nA. It has an In-lens and a Secondary electron detector.

References

[1] Farrow, R. F. C., editor. *Molecular Beam Epitaxy. Application to key materials.* Noyer Publications, (1995).

[2] Warusawithana, M. P., Cen, C., Sleasman, C. R., Woicik, J. C., Li, Y., Kourkoutis, L. F., Klug, J. A., Li, H., Ryan, P., Wang, L.-P., Bedzyk, M., Muller, D. A., Chen, L.-Q., Levy, J., and Schlom, D. G. *Science* **324**, 367 (2009).

[3] Wang, X. J., Buyanova, I. A., Zhao, F., Lagarde, D., Balocchi, A., Marie, X., Tu, C. W., Harmand, J. C., and Chen, W. M. *Nat. Mat.* **8**, 198 (2009).

[4] Nikishin, S., Borisov, B., Pandikunta, M., Dahal, R., Lin, J. Y., Jiang, H. X., Harris, H., and Holtz, M. *Appl. Phys. Lett.* **95**, 054101 (2009).

[5] Ko, K.-M., Seo, J.-H., Kim, D.-E., Lee, S.-T., Noh, Y.-K., Kim, M.-D., and Oh, J.-E. *Nanotechnology* **20**, 225201 (2009).

[6] Stolichnov, I., Riester, S. W. E., Trodahl, H. J., Setter, N., Rushforth, A. W., Edmonds, K. W., Campion, R. P., Foxon, C. T., Gallagher, B. L., and Jungwirth, T. *Nat. Mat.* **7**, 464 (2008).

[7] Tsintzos, S. I., Pelekanos, N. T., Konstantinidis, G., Hatzopoulos, Z., and Savvidis, P. G. *Nature* **453**, 372 (2008).

[8] König, M., Wiedmann, S., Brüne, C., Roth, A., Buhmann, H., Molenkamp, L. W., Qi, X.-L., and Zhang, S.-C. *Science* **318**, 766 (2007).

[9] Tsukazaki, A., Ohtomo, A., Kita, T., Ohno, Y., Ohno, H., and Kawasaki, M. *Science* **315**, 1388 (2007).

[10] W.Braun. *Applied RHEED: Reflection High Energy Electron Diffraction During Crystal Growth*, volume 154 of *Springer Tracts in modern Physics.* Springer, (1999).

[11] Britze, K. and Meyer-Ehmsen, G. *Surf. Sci.* **77**, 131 (1978).

[12] Lee, Y., Juang, J. Y., Ou, J. H., Chen, Y. F., Wu, K. H., Uen, T. M., and Gou, Y. S. *Physica B* **284-288**, 2099 (2000).

[13] Neave, J. H., Joyce, B. A., Dobson, P. J., and Norton, N. *Appl. Phys. A* **31**, 1 (1983).

[14] Hernandez-Calderon, I. and Hochst, H. *Phys. Rev. B* **27**, 4961 (1983).

[15] Harris, J. J., Joyce, B. A., and Dobson, P. J. *Surf. Sci.* **103**, L90 (1981).

[16] Wood, C. E. C. *Surf. Sci.* **108**, L441 (1981).

[17] Hove, J. M. V., Lent, C. S., Pukite, P. R., and Cohen, P. I. *J. Vac. Sci. Technol.* **B1**, 741 (1983).

[18] Lee, D., Barnett, S. J., Pitt, A. D., Houlton, M. R., and Smith, G. W. *Appl. Surf. Sci.* **50**, 428 (1991).

[19] Arthur, J. R. *Surf. Sci.* **500**, 189 (2002).

[20] Auciello, O. and Krauss, A. R. *In situ real-time characterization of thin films.* John Willey & Sons, Inc, (2001).

[21] Krost, A., Bauer, G., and Woitok, J. *Optical characterization of epitaxial semiconductor layers.* Springer, Berlin/ Heidelberg/ New York, (1995).

[22] Hecht, E. *Optics*, 101. Adison Wesley, 4^{th} edition (2002).

[23] Foner, S. *Rev. Sci. Instr.* **30**, 548 (1959).

[24] Flanders, P. J. *J. Appl. Phys.* **63**, 3940 (1988).

[25] Chikazumi, S. *Physics of Ferromagnetism.* Oxford University Press, (1997).

[26] Yao, N. and Wang, Z. L., editors. *Handbook of Microscopy for nanotechnology.* Springer, (2005).

[27] Jaeger, R. C. *Introduction to Microelectronic Fabrication*, volume Volume V of *Modular series on Solid State Devices.* Prentice Hall, New Jersey, (2002).

Chapter 5

Anomalous anisotropic magnetoresistance in $Fe_3O_4(001)$ epitaxial films

5.1 Introduction

Many transition metal oxides exhibit charge and orbital ordering which manifests itself in a spatial localization of charge carriers on certain ionic sites and electron orbitals, respectively. These correlated ordering processes govern the physical properties, such as; magnetism and charge transport, and are responsible for many ubiquitous phenomena [1, 2, 3]. Magnetite, Fe_3O_4, is one of the important 3d transition metal oxides, with a high Curie temperature (858 K) and presence of a metal-insulator transition (MIT) at around 125 K (known as Verwey transition). Due to its predicted half metallic nature, it is viewed as a potentially interesting material for spintronic applications [4, 5]. The Verwey transition in Fe_3O_4 is a metal-insulator transition that leads to a change in conductivity by

two orders of magnitude across the transition temperature and is believed to be associated with an order-disorder transition from a charge-ordered state of B-site Fe ions ($Fe^{+2,+3}$, for octahedral Fe-ions) with a high resistivity at low temperatures to a disordered state ($Fe^{+2.5}$ at all B-sites) at higher temperatures and an increased conductivity. Despite decades of research, the underlying physics related to this transition is not yet completely clear [6, 7]. Various techniques have been used to grow epitaxial hetero-structures based on magnetite [8, 9, 10]. MgO is an ideal template to grow Fe_3O_4 films owing to the small lattice mismatch. However, the Fe_3O_4/MgO hetero-epitaxial system suffers from the formation of antiphase boundaries (APB) [11, 12, 13, 14]. The presence of APBs has a deleterious effect on the magnetic properties but they are beneficial in enhancing the magneto-resistance of films due to the additional spin scattering induced at the APB [15, 16]. Magneto-transport studies in epitaxial magnetite films are mostly focused on the influence of APBs, disorder and strain. Simulations show that an uniaxial strain has significant effects on the electronic structure of magnetite, the insulating band gap of the majority spin is reduced and the half-metallic behaviour eventually turns into normal metal behavior at high-strain states [17]. In a recent study [18], it was shown that if the APBs in Fe_3O_4 films are manipulated in an ordered fashion one can attain a sizable magnetoresistance.

Understanding mechanisms that affect the magneto-transport behavior in Fe_3O_4 is of crucial importance in realization of its application as a magneto-resistive sensor. One of the mechanisms contributing to the magneto-transport phenomenon is the anisotropic magnetoresistance, AMR. In ferromagnets, the AMR is caused by the spin-orbit interaction, which gives rise to a magnetization-direction dependent scattering rate [19, 20, 21]. As a result, the conductivity of a saturated sample is affected by the angle between the electrical current $\vec{J}$ and magnetization

$\vec{M}$. The angular dependence of resistivity is generally given by

$$\rho = \rho_{\perp} + (\rho_{\parallel} - \rho_{\perp})cos^2\theta \tag{5.1}$$

where $\rho_{\parallel}$ and $\rho_{\perp}$ are the resistivities for $\vec{M} \parallel \vec{J}$ and $\vec{M} \perp \vec{J}$ respectively. Various mechanisms have been proposed to explain the origin of the AMR and its link to spin-orbit coupling. Some aspects of AMR have been dealt theoretically by Smit [19], Berger [22], Potter [23], Campbell and Fert [24]. In ferromagnetic poly crystalline alloys the magnitude of the AMR is around 20 and 5 % at low temperature (20 K) and room temperature respectively [20]. In single crystals and epitaxial thin films, in contrast to poly-crystals, additional features in AMR at low fields are observed which are related to the magneto-crystalline anisotropy and the AMR exhibits a deviation of the angular dependence from the $cos^2\theta$ curve [25, 26]. Enhanced magnitude of up to several tens of percent could be obtained in nano-structured devices like multilayers, constrictions in the ballistic regime, and nanowires [27, 28]. There are studies aimed at understanding the charge and spin coupling on AMR. In particular, AMR investigations in epitaxial thin films and single crystals of rare earth manganites have shown an anomalous temperature dependence where the magnitude of AMR peaks at a temperature close to the MIT, which is an issue actively debated by theoreticias and experimentalists [29, 30, 31]. In Fe_3O_4 films, the AMR investigations have been performed by Ziese et al. [32, 33]. In films of thickness larger than 15 nm, they found a temperature independent AMR ($\sim$ 0.5 %) for $T > 200$K, and a sign change in AMR at temperatures close to Verwey transition. No details of the angular dependence of the AMR were provided.

In this chapter we report a detailed study of angular and temperature dependence of AMR in a synthetic single crystal of Fe_3O_4 and epitaxial Fe_3O_4 films of different thickness grown on MgO(001) substrates. Remarkably, in angular dependence of

AMR, we observe an additional anisotropy, superimposed on the conventional two-fold anisotropy at temperature below 200 K. Its magnitude grows with an increasing field and decreasing temperature. We provide possible explanations for the observed effect.

5.2 Experiment

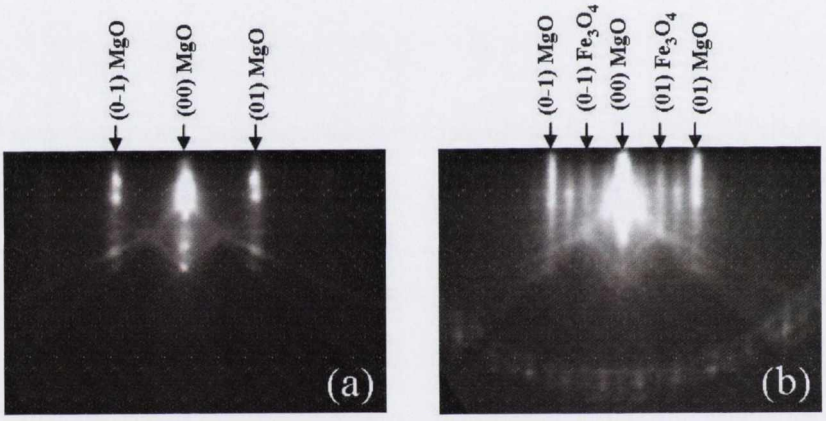

Figure 5.1: RHEED patterns along <100>. (a) Annealed MgO substrate (b) 67 nm thick Fe_3O_4 film.

The Fe_3O_4 thin films of thicknesses 33, 67 and 200 nm were grown on MgO(001) single crystal substrates using an oxygen plasma assisted molecular beam epitaxy (DCA MBE M600) with a base pressure of 5 x 10^{-10} Torr. The substrates were annealed at 600°C in UHV for 1/2 h followed by 2 h annealing in 1.1x10^{-5} Torr oxygen. The growth of Fe_3O_4 films was carried out by means of electron beam evaporation of pure metallic Fe (99.999 %) in the presence of free oxygen radicals (1.1x10^{-5} Torr). Substrate temperature during growth was 250 °C. Details of the

growth procedure can be found elsewhere [18].

Figure 5.1(a) shows the RHEED pattern of the MgO(001) single crystalline substrate measured along the <100> azimuth after the annealing procedure in oxygen atmosphere. It shows vertical lattice rods and radial Kikuchi lines indicative of well ordered and flat surface. Figure 5.1(b) shows the RHEED pattern for a 67 nm thin film, the appearance of half order lattice rods in the middle of lattice rods corresponding to MgO, indicate the formation of Fe_3O_4.

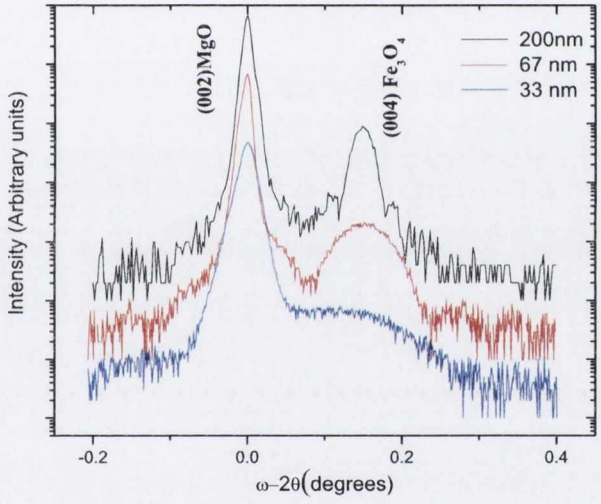

Figure 5.2: The ω-2θ scans for the Fe_3O_4 thin films on MgO used in this study. The scan was measured for the (002) Bragg reflection common to substrate and thin film. Curves are shifted along the vertical axis for clarity

Figure 5.2 shows the $\omega - 2\theta$ scan at room temperature, for the (002) and (004) Bragg reflections of substrate and film respectively for the three thin films used in this study, the curves are shifted for clarity. From the peak separation, using Bragg's law (Eq. 4.5) and the relation between lattice constant and interplanar

spacing for a cubic crystal, we obtained a value of $a_{\perp}$= 0.8369 nm. The in-plane lattice constant was determined from the asymmetric scans performed on the (113) and (226) common peak of substrate and film respectively. The obtained value was $a_{||}$= 0.8426 nm. The unit cell volume of the films (0.594 nm^3), consistent with that of bulk magnetite, is a signature of the high degree of stoichiometry of the films.

Resistance versus temperature measurements for the samples were performed using a standard four probe method. Prior to the transport measurements, the samples were patterned into the Hall bar geometry by UV-lithography and chemically etched with an 8.55 M HCl solution.

In order to study the angular dependence of the AMR, the samples were subjected to a constant in-plane magnetic field $\vec{H}$, while the angle θ, with respect to the electric current I, was changed from 0 to 360 degrees. The longitudinal voltage which is proportional to the AMR was measured between contacts V^+ and V^- (inset Fig. 5.4(a)). A DC bias current was applied along the <100> direction, the applied current was always kept in 1-10 μA range for the thin film samples and in 1-10 mA range for the single crystal. The synthetic crystal of Fe_3O_4 used in this study was grown employing the skull melting technique and showed a Verwey transition temperature (T_V) of 119 K.

5.3 Results and discussion

We present a systematic study of the angular dependence of the anisotropic magnetoresistance at different temperatures and magnetic field strengths on 33, 67 and 200 nm thick Fe_3O_4 films grown on MgO(001) substrates. Prior to the AMR measurements the temperature dependence of the resistivity was measured. Figure 5.3(a) shows the resistivity as a function of temperature for all the films. Also

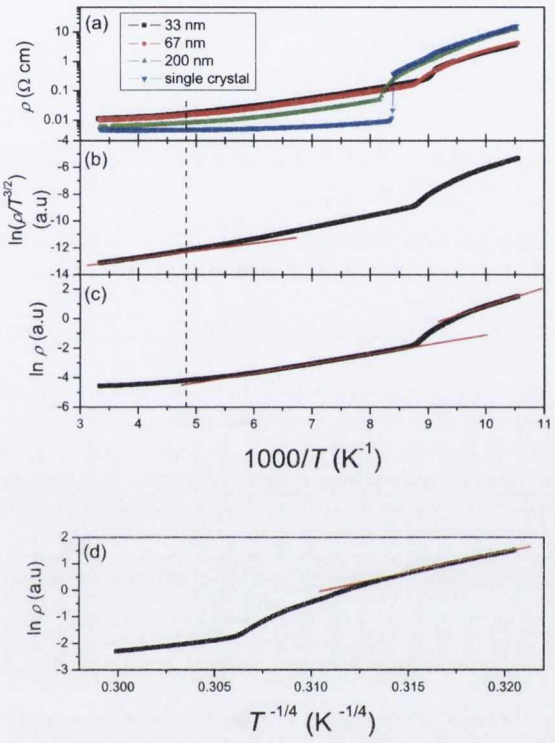

Figure 5.3: (a) Temperature dependence of the resistivity for all the thin film samples of Fe_3O_4 along with that of single crystal Fe_3O_4 samples. The Verwey transition temperatures are found to be 110, 112 and 121 K for the 33, 67 and 200 nm thick films respectively. Verwey transition for the single crystal was 119 K. Panels (b) to (d) show the resistivity of the 67 nm thick film fitted (red lines) to the (b) Small-polaron hopping (c) Arrhenius law and (d) variable range hopping (VRH) models. The VRH expression is only fitted for temperatures below T_V.

Thickness (nm)	T_v (K)	ρ [300K] (Ωcm)
33	110	0.0113
67	112	0.0105
200	121	0.0063
single crystal	119	0.0048

Table 5.1: Verwey transition and resistivity measured for the thin film samples and magnetite single crystal used in this study.

shown in the figure is the data for a single crystal slice of Fe_3O_4 cut along the (001) plane. Resistivity of the films at 300 K is found to increase with a decrease in film thickness and is greater than that of the single crystal (see table 5.1). These observations are in line with the previously reported values of resistivities and T_V [32, 34].

Temperature dependence of resistivity for Fe_3O_4 films suggests that the electronic transport in Fe_3O_4 follows a thermally activated behaviour, with an increase in conductivity as the temperature is increased. As previously reported [35], three regions with different activation energies can be distinguished. The first one is a high temperature region ($T \gtrsim 200$ K), the second is a middle temperature region (just above T_V up to ~ 200 K) and the third a low temperature region (below T_V), hereafter referred to as region I, II and III respectively. The resistivity data was fitted using expressions for small-polaron hopping ($\rho/T^{3/2} = Aexp(W_p/k_BT)$) in region I, Arrhenius law or band gap model ($\rho = \rho_\infty exp(E_a/k_BT)$) in regions II and III and variable-range hopping ($\rho = \rho_\infty exp(T_0/T)^{1/4}$) for temperatures below T_V [36]. Different models were used for region I and II due to the fact that the Arrhenius law is know to be applicable at temperatures not too far above the Verwey transition [37], furthermore

Thickness (nm)	**Arrhenius law** (meV) $\rho = \rho_\infty exp(E_a/kT)$		**Small-polaron hopping** (meV) $\rho/T^{3/2} = Aexp(W_p/kT)$	**VRH** (K) $\rho = \rho_\infty exp(T_0/T)^{1/4}$
	E_a^{II}	E_a^{III}	W_p^I	T_0 (regime III)
33	58.0	92.5	53.0	$3.7 * 10^8$
67	56.8	102.9	52.6	$6.0 * 10^8$
200	55.0	106.9	46.1	$8.8 * 10^8$
single crystal	31.8	112.6	33.0	$9.1 * 10^8$

Table 5.2: Values of activation energies (E_a) and polaron hopping energies (W_p) at 0 Tesla in different temperature regions determined using various conductivity models for different thickness films and single crystal magnetite. W_p^I relate to the temperature region T>200 K; E_a^{II} to the region 120 K<T<200 K. E_a^{III} and T_0 were obtained at temperatures below the Verwey transition.

the activation energies obtained using Arrhenius law in region I are quite small, around same magnitude of the thermal energy ($k_B * 300K = 26meV$). Figures 5.3(b) to 5.3(d) show the data for the 67 nm thick film fitted to small-polaron hopping (Fig. 5.3(b)), Arrhenius law (Fig. 5.3(c)) and variable-range hopping (5.3(d)). From the slope of the curves we obtain the polaron hopping energy (W_p), activation energy (E_a) and Mott temperature (T_0) respectively. These parameters obtained using the above models are summarized in Table 5.2.

The values of E_a agree well with previous reports [32] both above and below T_V. The Mott temperature T_0 is found to be related to the localization length [38] and agrees well with earlier reported values [9]. The existence of two different electrical conduction regions above T_V *(i. e. region I and II)* in magnetite agrees

well with the Ihle et al.'s model [39] for small polaron (SP) band and SP hopping conduction, the first one being dominant at lower temperatures (just above T_V, region II) and the latter one at higher temperatures (region I).
Now, let us examine the temperature and magnetic field dependence of the measured AMR. The AMR is usually defined as the ratio: AMR = $(\rho_{\parallel} - \rho_{\perp})/\rho_{ave}$, where $\rho_{\parallel}$, $\rho_{\perp}$ are the resistivities for magnetic field applied parallel, perpendicular to the current direction respectively and $\rho_{ave} = \rho_{\parallel}/3 + 2\rho_{\perp}/3$. Our results show a room temperature value of about 0.3 %, in agreement with earlier reports [32, 33, 40].

Figure 5.4(a) shows the relative amplitude of the angular dependence of the magnetoresistance for the 67 nm sample at an applied field of 5 Tesla for a series of temperatures T = 300, 250, 200, 150, 120 K (defined as: $\Delta\rho/\rho_{min}(\%) = [(\rho(\theta) - \rho_{min})/\rho_{min}] * 100$, where θ is the angle between magnetic field and current and ρ_{min} is the minimum of resistivity for each scan). The data was also taken in the reverse angular sweep and resulted in no hysteresis in the AMR. At high temperatures (above 200 K), the angular dependence of AMR follows the typical $cos^2\theta$ dependence (two-fold symmetry) with peaks at 0° and 180° and valleys at 90° and 270° respectively. When the sample is cooled down to a temperature below 200 K a deviation from the two-fold symmetry starts to appear with the valleys near 90° and 270° broadening and eventually an additional set of peaks appearing showing an overall four-fold symmetry, which becomes dominant at lower temperatures. Similar behavior was exhibited by the other films and by a (001) oriented stoichiometric Fe_3O_4 single crystal (Fig. 5.4(b)). Similar features in the angular dependence of AMR have been previously observed in manganites [41] and more recently in diluted magnetic semiconductors (DMS) [42, 43]. In the latter case it has been related to the existence of two conduction mechanisms with different temperature dependencies. In general, additional anisotropy terms in

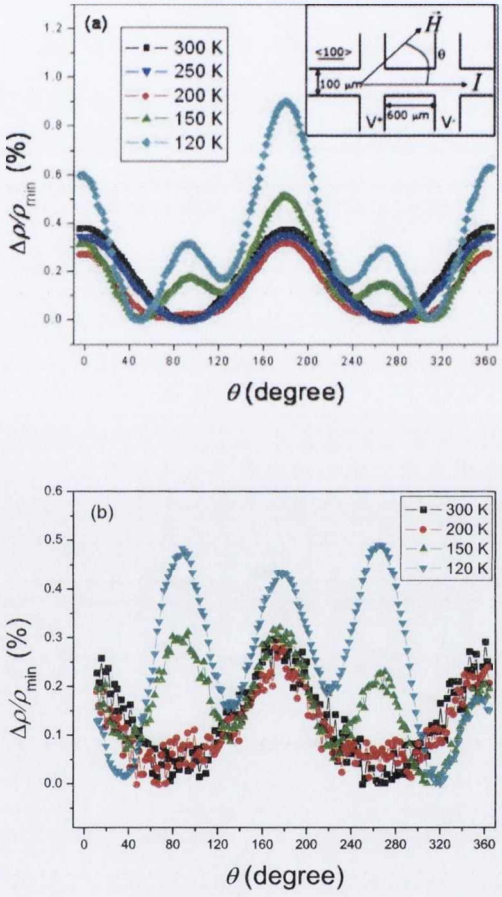

Figure 5.4: (a) Angular dependence of the magnetoresistance for the 67 nm Fe_3O_4 thin film sample measured at $\mu_0\vec{H}$= 5 Tesla. Below 200 K, it can be seen that the aditional anisotropy develops with peaks at 90° and 270°. (b) Angular scan of AMR at different temperatures for the (001) oriented single crystal Fe_3O_4 measured at 5 Tesla field. Inset in Fig. 5.4(a) shows the Hall bar geometry used in these investigations.

the AMR response appear for single crystalline thin films provided the magnitude of external field is below the anisotropy field, such an example can be found for the case of a manganite thin film [44].

The appearance of an additional anisotropy in the AMR in Fe_3O_4 films is quite surprising. In order to establish its possible origin, we investigate the angular dependence of AMR at different magnetic fields. A representative data of angular scans for a 67 nm thick Fe_3O_4 film measured at 150 K with varying magnetic field strengths (0.1, 0.5, 1.0, 5.0 and 14 Tesla) is shown in Fig. 5.5(a). Surprisingly, we notice that even with an increase in the magnetic field up to 14 T, we could not overcome this anisotropy. Furthermore the fact that the peaks related to the additional anisotropy are present at positions where the angle between the magnetic field and current is 90°, could suggest that it originates because of the contribution of Lorentz force (whose magnitude is greatest when the field is applied perpendicular to the current). The Lorentz force related contribution can be observed if $\omega_c\tau > 0.1$ [41], where ω_c is the cyclotron frequency ($\omega_c = eB/m^*c$) and τ is the scattering time. This condition can be written as $BR_H/\rho = tan\theta_H > 0.1$ where R_H is the Hall coefficient and θ_H the Hall angle. For a 5 Tesla field we estimate a value of $BR_H/\rho = tan\theta_H \sim 10^{-5}$, therefore, Lorentz force effects can be ruled out. Furthermore the magnetoresistance (MR(H)(%)=[($\rho(H) - \rho(0)$)/$\rho(0)$]*100) of the samples is always negative (see Fig. 5.5(b)), in contrast to the positive magnetoresistance expected from the Lorentz force effects.

In order to understand the mechanism related to this additional anisotropic terms in AMR behaviour of magnetite, we need to look at the details of the origin of AMR in ferromagnets. Phenomenologically, AMR shows a two-fold symmetry for polycrystalline materials because the magnetocrystalline effect is averaged out. However in single crystals and epitaxial films, it contains higher order terms which reflect the symmetry of the crystals [45, 46].

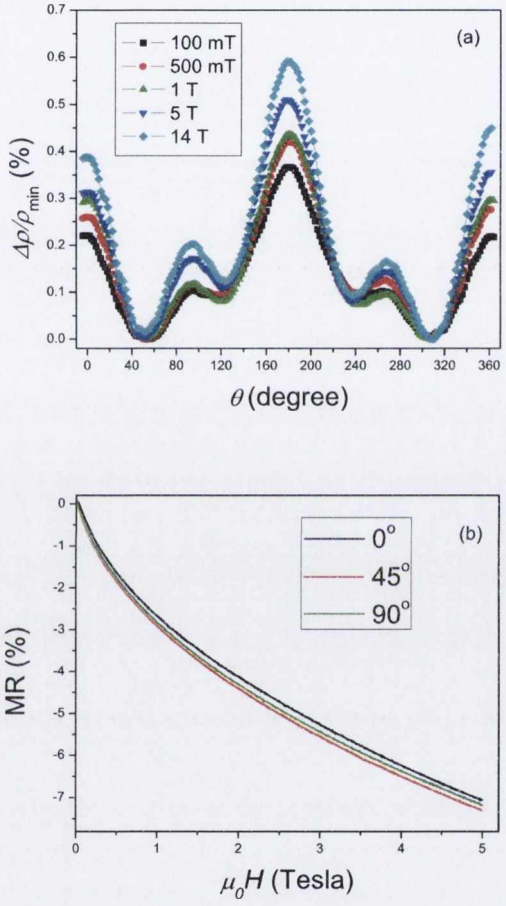

Figure 5.5: (a) Angular dependence of the magnetoresistance for the 67 nm thick Fe_3O_4 thin film measured at 150 K. The data is plotted for different field values of 100 mT, 500 mT, 1 T, 5 T and 14 T (b) Magnetoresistance of the 67 nm thick film measured at field orientations 0, 45 and 90 ° with respect to the current.

Using the phenomenological description for the anisotropic magnetoresistance, the dependence of the resistivity tensor with respect to the angle between magnetization and current can be calculated. Expanding the resistivity tensor as a function of the direction cosines of the magnetization and considering the symmetric part only gives:

$$\rho_{ij}(\vec{\alpha}) = a_{ij} + a_{ijkl}\alpha_k\alpha_l + a_{ijklmn}\alpha_k\alpha_l\alpha_m\alpha_n + ... \tag{5.2}$$

where $a_{ij}, a_{ijkl}, a_{ijklmn}$ are elements of the tensor up to the fourth order and the α_k are the direction cosines of the magnetization. The number of coefficients can be reduced considering the symmetry of the crystal [47]. For an in-plane magnetization and current applied in the $< 100 >$ direction, the obtained resistivity tensor looks as follows:

$$\rho(\theta) = C_0 + C_2 cos^2\theta + C_4 cos^4\theta \tag{5.3}$$

with $C_0 = a_{11} + a_{1122} + a_{111122}$, $C_2 = a_{1111} - a_{1122} - 2a_{111122} + a_{112211}$ and $C_4 = a_{111111} + a_{111122} - a_{112211}$, and θ the angle between magnetization and current directions. This result is based on power expansions in terms of $cos^n\theta$; even though our data is analysed using the following expression:

$$\rho(\theta) = a_0 + a_u cos2\theta + a_c cos4\theta \tag{5.4}$$

since we can extract direct information on the uniaxial and cubic components of the anisotropic magnetoresistance. The a_0, a_u and a_c constants are related to the previous ones by $a_0 = C_0 + C_2/2 + 5/8C_4$, $a_u = (C_2 + C_4)/2$ and $a_c = C_4/8$.
We fit the angular dependence of AMR using the expression of Eq. 5.4, obtaining the coefficients a_u and a_c, which are proportional to the uniaxial and cubic component respectively. These are plotted as a function of temperature for the three different samples and an applied field of 5 Tesla in Fig. 5.6.

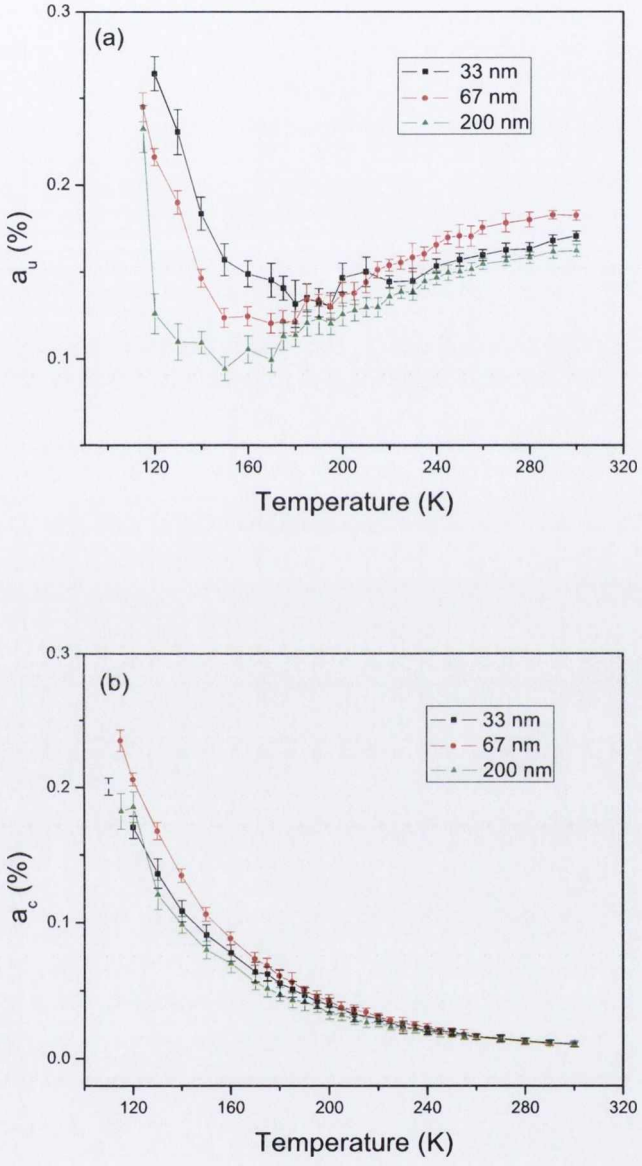

Figure 5.6: Temperature dependence of the (a) uniaxial (a_u) and (b) cubic (a_c) components for samples of three different thicknesses. The coefficients are determined from the angular-dependent AMR scans taken at each temperature with an applied field of 5 Tesla.

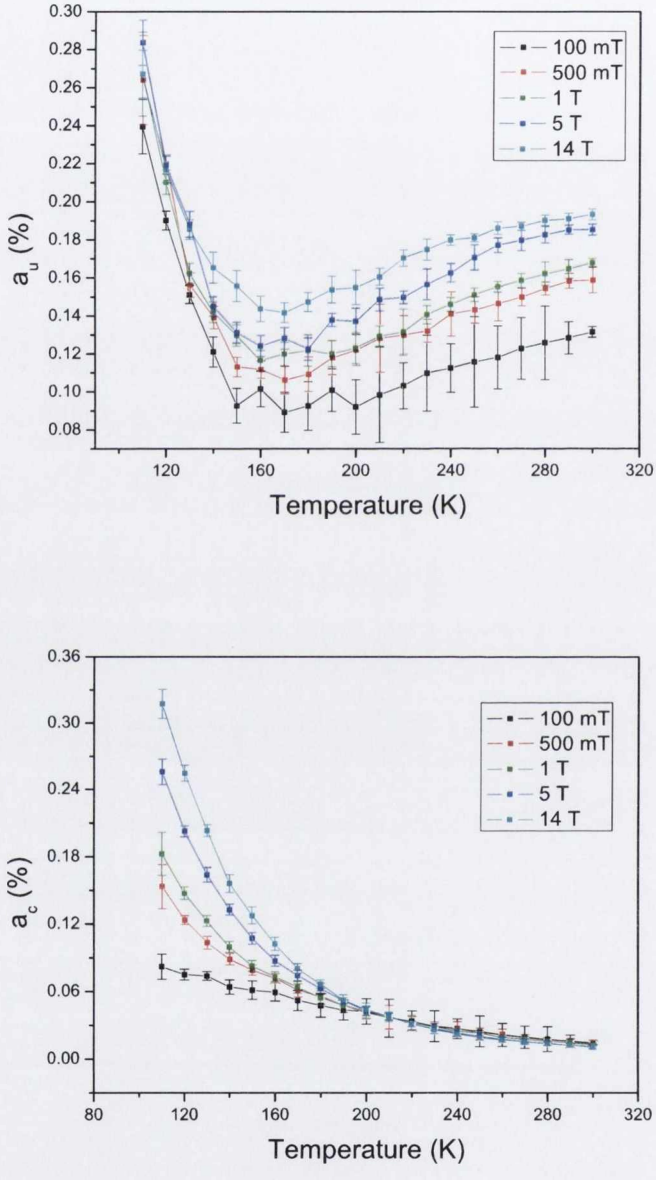

Figure 5.7: Temperature dependence of the (a) uniaxial (a_u) and (b) cubic (a_c) components at different applied fields for the 67 nm thick film.

It can be noticed that the uniaxial component (a_u) shows a non-monotonic temperature dependence with its minimum shifted towards lower temperatures with increasing thickness. The cubic component (a_c) shows a monotonic dependence with a continuous increase as the temperature is decreased. Wu et al. observed a similar behavior in (Ga,Mn)As films [42]. They consider the cubic component arising from the ferromagnetic order of the sample which is due to reduced thermal fluctuations of the spins as the temperature is decreased and as the spins become more aligned it is possible to observe higher order terms. They considered the uniaxial component to be dependent on the ferromagnetic order as well as on a superparamagnetic component (SPM) arising from bound magnetic polarons (BMP).

Since the characteristic features are similar for the three thin films, we focus our disscussion on the 67 nm thick film sample. Figures 5.7(a) and 5.7(b) show the temperature dependence of the fitting coefficients (a_u and a_c) obtained at fields 0.1, 0.5, 1, 5 and 14 Tesla. The uniaxial component shows a similar temperature dependence for all field values. Its magnitude increases with an increasing magnetic field above 140 K. Below 140 K we notice a non-monotonic field dependence in a_u. The increase in magnitude of a_u with magnetic field for $T >$ 140 K is contrary to the notion that AMR (AMR=$(\rho_{\parallel} - \rho_{\perp})/\rho_{ave}$) is independent of the magnetic field at fields above the saturation field. This behavior can be explained on the basis that Fe_3O_4 films contain APBs, which leads to a field dependent MR due to a non-saturation of the magnetization in fields up to several Tesla. The non-monotonic field dependence below 140 K could be related to the sign change of the magnetic anisotropy constant (K_1) in magnetite, which happens above T_V at $\sim$ 130 K [48]. In contrast to it, the cubic component shows the same temperature dependence for all field values and no field dependence down to a temperature of about 200 K. Below 200 K, a_c shows a different temperature

dependence for different field values, with a stronger increase in magnitude for higher magnetic fields.

The fact that the additional symmetry appears at a temperature well above T_V is in agreement with previous reports where anomalies in muon spin rotation (μSR) measurements [49] and neutron scattering experiments [50, 51] have been observed at temperatures $T > T_V + 100$, which have been related to the formation of polarons.

Recalling the discussion on the temperature dependence of the resistivity for our films, we consider the activation energies measured in region II. Following the model by Ihle et al. [39], the electron-phonon coupling constant (S_0) was obtained and the temperature of transition between the SP band and hopping conduction region, was calculated using the expression $kT' = \omega_0\{2ln[2S_0 + (1 + 4S_0^2)^{1/2}]\}^{-1}$ [52], where $\omega_0 = 0.07eV$ (highest longitudinal optical phonon mode). We obtained the temperature value of $T' = 215K$ for the 67 nm thick film. This is in good agreement with the temperature where the a_c component shows the splitting with the field (see Fig. 5.7(b)) around 200 K, suggesting that the observed anomaly is a consequence of a change in the conduction mechanism in magnetite due to the formation of polarons. Piekarz et al. [53, 54] have recently proposed a mechanism for the Verwey transition as a cooperative effect between intra-atomic Coulomb interaction of Fe ions and phonon-driven lattice instability. They developed a model which shows that the strong electron-phonon coupling induces local crystal deformations and a polaronic short-range order above T_V and point out that the signs of the metal-insulator transition already appear at about 200 K [50, 51, 55].

According to their model, the X_3 phonon mode is responsible for the observation of charge-order stabilization at temperatures higher than the Verwey transition temperature, neutron scattering data [56] and dispersion curves [54]

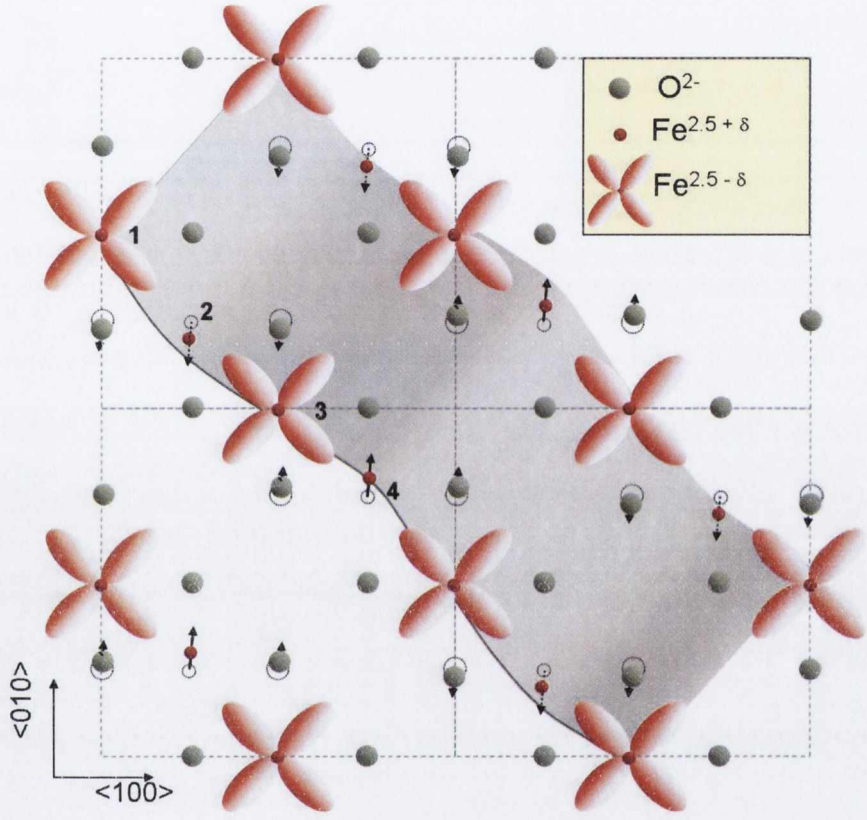

Figure 5.8: Representation of the atomic displacements induced by the X_3 phonon mode. Broken (solid) arrows represent displacements along $< 0\bar{1}\bar{1} >$ ($< 011 >$). The cations in positions 2 and 4 and its nearest neighbor anions in the $< 100 >$ direction are displaced along $< 0\bar{1}\bar{1} >$ ($< 011 >$) respectively, therefore the atomic sites in positions 1 and 3 will present t_{2g} orbital ordering (d_{xy} orbital) due to the lower Coulomb repulsion as a consequence of the out of plane displacement of two of the nearest neighbor anions.

show that the energy of this mode is around 17 meV ($\sim$ 197 K), which is in close agreement with the temperature where we observe the splitting in the a_c component. This mode consists of atomic displacements of the octahedral Fe and O atoms along <110> and <1$\bar{1}$0> directions in alternate planes. These displacements modify the interplanar distances between Fe-O atoms, stabilizing charge and orbital order of the t_{2g} states (see Fig. 5.8). The charge order creates a charge disequilibrium between the Fe ions on B sites (octahedrally coordinated cation sites in the spinel structure of magnetite), ideally departing from the average $Fe^{2.5+}$ state to Fe^{2+} and Fe^{3+} at different octahedral sites. It is known that Fe^{3+} has a singlet ground state $^6S_{5/2}$ with orbital moment zero and therefore no spin-orbit splitting. On the other hand the Fe^{2+} has a ground state $^5D_4$ that will be split by spin-orbit interactions [57]. Therefore the charge ordering produces an enhancement of the effect of the spin-orbit interaction. Since the anisotropic magnetoresistance is a consequence of this interaction [19, 20, 23] it can be expected that the the effect of polaron formation, thus charge ordering in the system can be observed by anisotropic magnetoresistance measurements as evidence from our observations.

5.4 Conclusion

Deviation from the normal $cos^2\theta$ angular dependence of the anisotropic magnetoresistance has been observed in epitaxial Fe_3O_4 films grown on MgO(001) substrates. The deviation is manifested as an additional set of peaks at 90° and 270° for temperatures below 200 K. The same angular dependence was observed in magnetite (001)-oriented single crystals suggesting that the effect is of general nature rather than sample especific. This result is compared with the mechanism of the Verwey transition suggesting that the additional feature observed is re-

lated to a change in the conduction mechanism due to the formation of polaronic short-range order at temperatures above T_V. The effect of polaron formation can be observed by anisotropic magnetoresistance measurements as a consequence of enhancement of the effect of spin-orbit splitting, induced by the charge-order formation as explained above.

References

[1] Tokura, Y. and Nagaosa, N. *Science* **288**, 462 (2000).

[2] Imada, M., Fujimori, A., and Tokura, Y. *Rev. Mod. Phys.* **70**, 1039 (1998).

[3] Ziese, M. *Rep. Prog. Phys.* **65**, 143 (2002).

[4] Žutić, I., Fabian, J., and Sarma, S. D. *Rev. Mod. Phys.* **76**, 323 (2004).

[5] Fonin, M., Dedkov, Y. S., Pentcheva, R., Rüdiger, U., and Güntherodt, G. *J. Phys. Condens. Matter* **19**, 315217 (2007).

[6] Walz, F. *J. Phys.: Condens. Matter.* **14**, R285 (2002).

[7] García, J. and Subías, G. *J. Phys. Cond. Matter.* **16**, R145 (2004).

[8] Voogt, F. C., Fujii, T., Smulders, P. J. M., Niesen, L., James, M. A., and Hibma, T. *Phys. Rev. B* **60**, 11193 (1999).

[9] Ogale, S. B., Ghosh, K., Sharma, R. P., Greene, R. L., Ramesh, R., and Venkatesan, T. *Phys. Rev. B* **57**, 7823 (1998).

[10] Balakrishnan, K., Arora, S. K., and Shvets, I. V. *J. Phys.: Condens. Matter* **16**, 5387 (2004).

[11] Arora, S. K., Wu, H.-C., Choudhary, R. J., Shvets, I. V., Mryasov, O. N., Yao, H., and Ching, W. *Phys. Rev. B* **77**, 134443 (2008).

[12] Margulies, D. T., Parker, F. T., Spada, F. E., Goldman, R. S., Li, J., Sinclair, R., and Berkowitz, A. E. *Phys. Rev. B* **53**, 9175 (1996).

[13] Kale, S., Bhagat, M., Lofland, S. E., Scabarozi, T., Ogale, S. B., Orozco, A., Shinde, S. R., Venkatesan, T., Hannoyer, R., Mercey, B., and Prellier, W. *Phys. Rev. B* **64**, 205413 (2001).

[14] Eerenstein, W., Palstra, T. T. M., Hibma, T., and Celotto, S. *Phys. Rev. B* **68**, 014428 (2003).

[15] Sofin, R. G. S., Arora, S. K., and Shvets, I. V. *J. Appl. Phys.* **97**, 10D315 (2005).

[16] Eerenstein, W., Palstra, T. T. M., Saxena, S. S., and Hibma, T. *Phys. Rev. Lett.* **88**, 247204 (2002).

[17] Jeng, H.-T. and Guo, G. Y. *Phys. Rev. B* **65**, 094429 (2002).

[18] Arora, S. K., Sofin, R. G. S., and Shvets, I. V. *Phys. Rev. B* **72**, 134404 (2005).

[19] Smit, J. *Physica* **17**, 612 (1951).

[20] McGuire, T. R. and Potter, R. I. *IEEE Trans. Mag.* **11**, 1018 (1975).

[21] Jan, J. P. *Solid State Physics, edited by F. Seitz and D. Turnbull* **Vol. 5**, 1 – 96 (1957).

[22] Berger, L. *Phys. Rev.* **138**, 1083 (1965).

[23] Potter, R. I. *Phys. Rev. B* **10**, 4626 (1974).

[24] Campbell, I. A., Fert, A., and Jaoul, O. *J. Phys. C: Solid State Phys.* **3**, S95 (1970).

[25] Pallecchi, I., Gadaleta, A., Pellegrino, L., Gazzadi, G. C., Bellingeri, E., Siri, A. S., and Marré, D. *Phys. Rev. B* **76**, 174401 (2007).

[26] Amaral, V. S., Loureço, A. A. C. S., Araújo, J. P., Pereira, A. M., Sousa, J. B., Tavares, P. B., Vieira, J. M., Alves, E., da Silva, M. F., and Soares, J. C. *J. Appl. Phys.* **87**, 5570 (2000).

[27] Bolotin, K. I., Kuemmeth, F., and Ralph, D. C. *Phys. Rev. Lett.* **97**, 127202 (2006).

[28] Rüster, C., Gould, C., Jungwirth, T., Sinova, J., Schott, G. M., Giraud, R., Brunner, K., Schmidt, G., and Molenkamp, L. W. *Phys. Rev. Lett.* **94**, 027203 (2005).

[29] Viret, M., Gabureac, M., Ott, F., Fermon, C., Barreteau, C., Autes, G., and Guirado-Lopez, R. *Eur. Phys. J. B* **51**, 1 (2006).

[30] Bibes, M., Laukhin, V., Valencia, S., Martnez, B., Fontcuberta, J., Gorbenko, O. Y., Kaul, A. R., and Martínez, J. L. *J. Phys. Condens. Matter* **17**, 2733 (2005).

[31] Li, R.-W., Wang, H., Wang, X., Yu, X. Z., Matsui, Y., Cheng, Z.-H., Shen, B.-G., Plummer, E. W., and Zhang, J. *Proc Natl Acad Sci USA* **106**, 14224 (2009).

[32] Ziese, M. and Blythe, H. J. *J. Phys: Condens. Matter* **12**, 13 (2000).

[33] Ziese, M. *Phys. Rev. B* **62**, 1044 (2000).

[34] Sena, S., Lindley, R., Blythe, H., Sauer, C., Al-Kafarji, M., and Gehring, G. *J. Magn. Magn. Mater.* **176**, 111 (1997).

[35] Arora, S. K., Sofin, R. G. S., Shvets, I. V., and Luysberg, M. *J. Appl. Phys.* **100**, 073908 (2006).

[36] Ziese, M. and Srinitiwarawong, C. *Phys. Rev. B* **58**, 11519 (1998).

[37] Gridin, V. V., Hearne, G. R., and Honig, J. M. *Phys. Rev. B* **53**, 15518 (1996).

[38] Mott, N. F. *Conduction in Non-Crystalline Materials*, 17ff. Clarendon Press, Oxford (1993).

[39] Ihle, D. and Lorenz, B. *J. Phys. C: Solid State Phys.* **19**, 5239 (1986).

[40] Jin, X., Ramos, R., Zhou, Y., McEvoy, C., and Shvets, I. V. *J. Appl. Phys.* **99**, 08C509 (2006).

[41] O'Donnell, J., Eckstein, J. N., and Rzchowski, M. S. *Appl. Phys. Lett.* **76**, 218 (2000).

[42] Wu, D., Wei, P., Johnston-Halperin, E., Awschalom, D. D., and Shi, J. *Phys. Rev. B* **77**, 125320 (2008).

[43] et al., A. W. R. *Phys. Rev. Lett.* **99**, 147207 (2007).

[44] Bibes, M., Martínez, B., Fontcuberta, J., Trtik, V., Ferrater, C., Sánchez, F., Varela, M., Hiergeist, R., and Steenbeck, K. *J. Magn. Magn. Mater.* **211**, 106 (2000).

[45] Döring, W. *Ann. Phys.* **32**, 259 (1938).

[46] Gorkom, R. P., Caro, J., Klapwijk, T. M., and Radelaar, S. *Phys. Rev. B* **63**, 134432 (2001).

[47] Birss, R. R. *Symmetry and Magnetism.* North-Holland Publishing Co. Amsterdam, (1964).

[48] van der Heijden, P. A. A., van Opstal, M. G., Swüste, C. H. W., Bloemen, P. H. J., Gaines, J. M., and de Jonge, W. J. M. *J. Magn. Magn. Mater.* **182**, 71 (1998).

[49] Boekema, C., Lichti, R. L., Denison, A. B., Brabers, A. M., Cooke, D. W., Heffner, R. H., Hutson, R. L., and Schillaci, M. E. *Hyperfine Interactions* **31**, 487 (1986).

[50] Shapiro, S. M., Iizumi, M., and Shirane, G. *Phys. Rev. B* **14**, 200 (1976).

[51] Yamada, Y. *Phys. Rev. B* **21**, 4642 (1980).

[52] Ihle, D. *Z. Phys. B* **58**, 91 (1985).

[53] Piekarz, P., Parlinski, K., and Olés, A. M. *Phys. Rev. Lett.* **97**, 156402 (2006).

[54] Piekarz, P., Parlinski, K., and Olés, A. M. *Phys. Rev. B* **76**, 165124 (2007).

[55] Shvets, I. V., Mariotto, G., Jordan, K., Berdunov, N., Kantor, R., and Murphy, S. *Phys. Rev. B* **70**, 155406 (2004).

[56] Samuelsen, E. J. and Steinsvoll, O. *Phys. Status Solidi B* **61**, 615 (1974).

[57] McQueeney, R. J., Yethiraj, M., Chang, S., Montfrooij, W., Gardner, J. S., Metcalf, P., and Honig, J. M. *Phys. Rev. B* **73**, 174409 (2006).

Chapter 6

Anisotropic magnetoresistance of Fe_3O_4 films on vicinal MgO(001)

6.1 Introduction

The area of magnetic thin films on vicinal substrates has attracted a lot of activity in the past few years [1, 2, 3, 4], because of both their technological applications and interesting fundamental physics [5, 6]. The effect of translational symmetry breaking, caused by the introduction of atomic steps in such systems leads to additional in-plane magnetic anisotropies.

Magnetite (Fe_3O_4) is an important half-metallic material with a high Curie temperature (858 K) and presents a metal-insulator transition at T_V ~125 K (also known as Verwey transition). These properties have attracted a lot of interest in studies of possible spin-electronics applications. [7, 8, 9, 10]. It is known that epitaxial Fe_3O_4 films grown on MgO substrates present APBs [11, 12], the presence of these defects introduces local modifications of the structure and alters the magnetic interaction at the boundary, inducing additional exchange interactions

which are predominantly anti-ferromagnetic (AF) [13]. The effect of APBs can be observed both in transport and magnetic properties; with an increased resistivity, magneto-resistance [14] and making the films hard to saturate even with strong fields of up to several Tesla [15].

Vicinal MgO substrates with atomic steps, provide an excellent template for the manipulation of the APB density in Fe_3O_4 thin films using a bottom-up approach. The presence of miscut allows for the formation of atomic steps in the surface, therefore there is an increased probability of formation of antiphase boundaries along the step edges of the atomic terraces. The crystal structure of magnetite and MgO are based on the fcc oxygen sublattice. The adjacent (001) planes containing the octahedral Fe of Fe_3O_4 are separated by 0.2099 nm, this quite close to the the atomic step height in a vicinal MgO substrate. If we consider the nucleation by B-sites on the substrate, which is supported by STM studies [16, 17], there are 32 possible combinations of positioning the nucleation islands of Fe_3O_4 on two neighboring terraces. In order to calculate the probability of APB formation, we need to compare the positions of the atoms of the third atomic layer on the lower terraces with the positions of the atoms of the first Fe layer on the upper terrace. Of the possible 32 combinations, 16 have the nucleation rows of first B-site layer on the upper terrace parallel to the ones on the lower terrace. All these combinations result in the formation of APBs.

Figure 6.1 shows an example of the formation of a step induced APB in a MgO substrate miscut with respect to the (001) plane along the <100> direction. Figure 6.1(a) shows the MgO (001) surface with a monoatomic step directed along <010> direction. Figure 6.1(b) shows the nucleation of the first B site layer on both upper and lower terrace with nucleation rows parallel to each other. Figure 6.1(c) shows the formation of the second layer of tetrahedral sites (A sites) on the lower terrace. Figure 6.1(d) shows the formation of the third layer on the

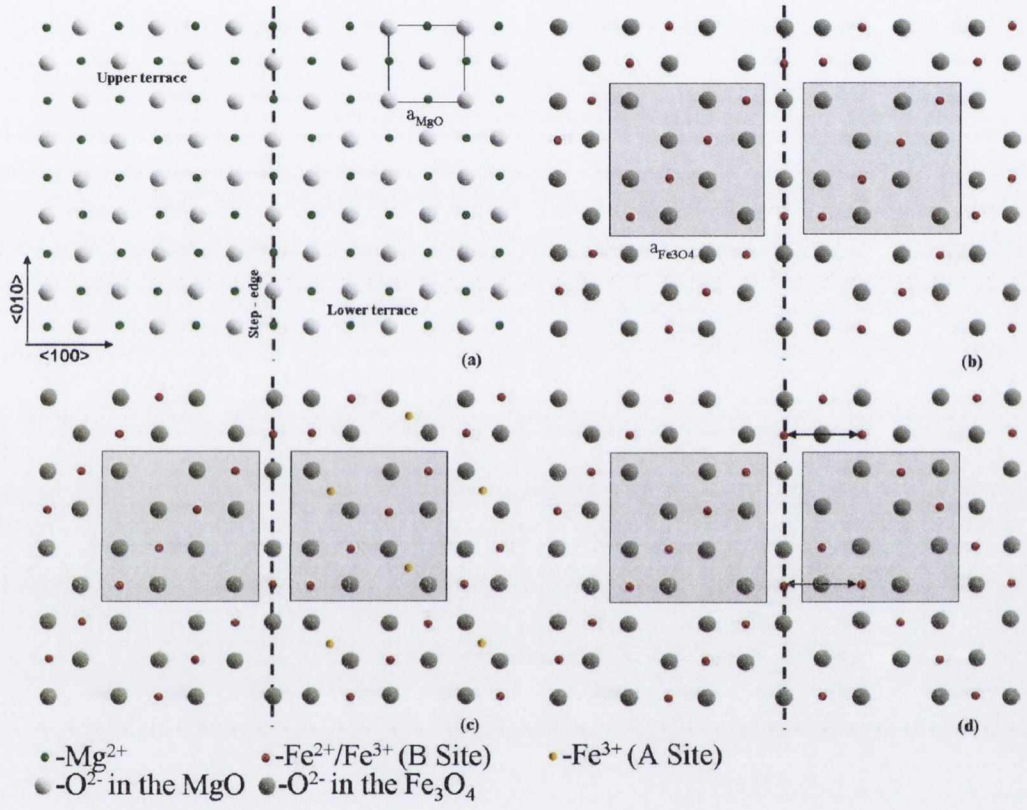

Figure 6.1: Example of the formation of a step induced APB. (a) MgO(001) surface with a monoatomic step directed along <100>. (b) Formation of the first B site layer on both the upper and lower terrace with nucleation rows parallel to each other (c) formation of the second layer on the lower terrace which is an A site plane (d) formation of the third layer on the lower terrace which is a B site plane with nucleation rows perpendicular to the upper terrace and hence the formation of step induced APB

lower terrace with the octahedral sites (B sites) forming rows perpendicular to the upper terrace and hence the formation of step induced APB. The remaining 16 combinations have the rows of the first B site layer on the upper terrace perpendicular to the rows of the first site B layer on the lower terrace. Half of these 16 combinations result in the formation of APB. Our analysis shows that there is 75 % probability of formation of APB along the step edge, if the nucleation starts at the B-sites.

Recent studies [18, 19] show that the Fe_3O_4 films grown on vicinal MgO substrates present anisotropic properties with respect to the step edge direction. In this chapter, we follow a similar aproach to study the effect of the translational symmetry breaking, caused by the presence of atomic steps, on the anisotropic magnetoresistance (AMR). The AMR is expected to be the same along two crystallographic equivalent directions (e.g. <100> and <010>), therefore any difference in AMR measured for currents applied parallel or perpencicular to the miscut direction must be a consequence of the presence of steps.

6.2 Experiment

The epitaxial Fe_3O_4 thin films used in this study were grown on (001) oriented MgO single crystal substrates using oxygen plasma assisted molecular beam epitaxy (DCA MBE M600). Before deposition the substrates were solvent cleaned prior to insertion into the growth chamber and then they were annealed at 600°C in UHV for 1/2 h followed by 5 h annealing in 1.1 x 10^{-5} Torr oxygen. More details about the growth procedure can be found elsewhere [18]. 30 nm thick Fe_3O_4 films were grown on two vicinal MgO (001) substrates, which were miscut by 2.86° and 7° with respect to (001) plane along the <100> direction. The results obtained were also compared with previous AMR data on 30 nm thick film

grown on a flat substrate (nominal miscut less than 0.5°. Reflection high-energy diffraction (RHEED) was employed to confirm the epitaxial growth and establish the growth mode. The presence of the RHEED intensity oscillations confirms that the films grow in a layer-by-layer mode with a growth rate of 0.3 Å/s.

Structural characterization of Fe_3O_4 thin films was done using a multi-crystal high-resolution x-ray diffractometer, HRXRD (Bede-D1, Bede, UK). The double axis configuration was performed to confirm the epitaxial relationship of the Fe_3O_4/MgO hetero-epitaxy. The miscut of the samples was also measured using the HRXRD technique. To determine the miscut of the sample, the ω-rocking curves were performed at (002) Bragg plane of the substrates at different azimuths. The amplitude and direction of miscut was determined by fitting the dependence of the Bragg incidence angle with the azimuth angle to a sine function (see chaper 3 for details). Magnetization measurements were performed using a vibrating sample magnetometer (Micromag-3900, Princeton Measurements, USA) with a sensitivity of 10^{-6} emu at an averaging time of 1 s per point. The diamagnetic contribution from the MgO substrate was substracted by performing a M-H loop of the MgO substrate of similar dimensions in the same field range. The magneto-transport measurements were carried out using a Physical Property Measurement System (Quantum Design PPMS 6000), which is equipped with a 14 Tesla superconducting magnet and a horizontal rotator that allows the sample orientation to be changed from -10 to 370 degrees. Prior to the measurements, Hall bars with the current path oriented along the <100> and <010> directions were fabricated using photolithography, these directions correspond to the perpendicular and parallel to the step edge (SE) directions respectively. The angular dependence of the magnetoresistance was measured using the standard four-probe method in a constant in-plane magnetic field, the orientation of which was changed with respect to the direction of applied current, <100> (<010>) for

directions perpendicular (parallel) to the SE direction respectively.

6.3 Results and discussion

We provide comparative results of measurements perfomed on 30 nm thick Fe_3O_4 films grown on vicinal samples with miscut angles of 2.86° and 7° with respect to the (001) plane along the <100> direction.

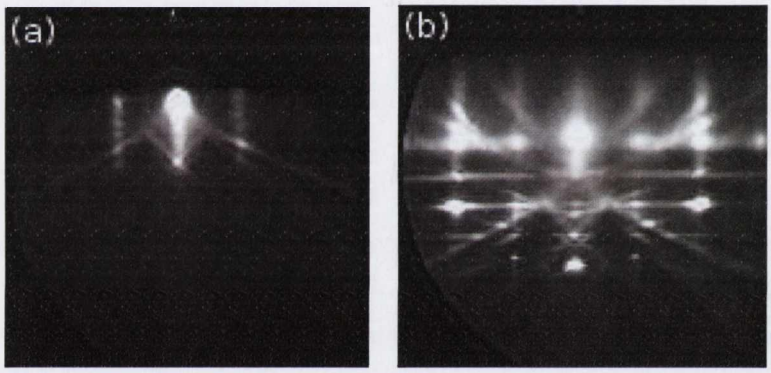

Figure 6.2: RHEED images of 2.86 ° miscut MgO (001) substrate after the annealing treatmet, just prior to deposition. Incident electron beam was directed (a) along the step edges and (b) perpendicular to the step edges.

RHEED measurements were performed in order to confirm the epitaxial growth and the presence of steps in the substrates and thin films, this was the only method to confirm the presence of steps, since atomic force microscopy (AFM) does not provide atomic resolution in ambient due to formation of hydroxide on the MgO surface [19]. Figure 6.2 shows the RHEED images of the 2.86° substrate after the UHV heat treatment, performed prior to deposition. The images were taken with an incident electron beam in the <100> directions of the MgO crystal (Figure 6.2(a) and 6.2(b)). Figures 6.2(a) and 6.2(b) correspond to the

case when electron beam is incident parallel or perpendicular to the SE directions, respectively. For the case when the electron beam is incident along the step edges, the vertical lattice rods and sharp Kikuchi lines are observed. Sharp horizontal Kikuchi lines are observed only when the direction of the incident electron beam is perpendicular to the step edges, which is a signature of increased inelastic scattering due to the presence of atomic steps.

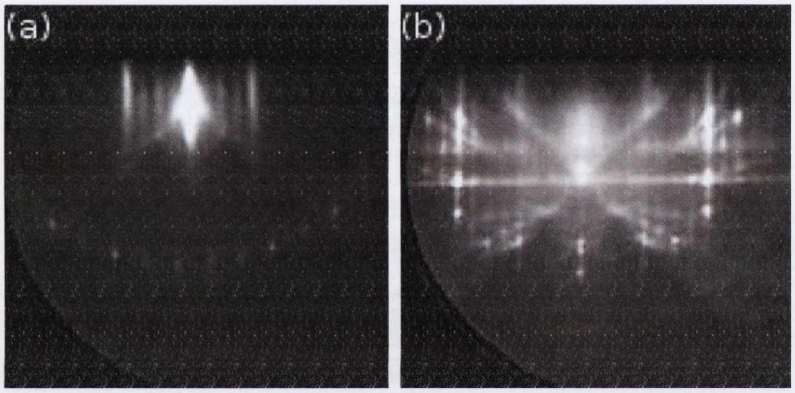

Figure 6.3: RHEED images of 30 nm Fe_3O_4 films deposited on 2.86 ° miscut MgO (001). Incident electron beam was directed (a) along the step edges and (b) perpendicular to the step edges.

Figure 6.3 shows the RHEED images obtained after the growth of 30 nm Fe_3O_4 film on the 2.86 ° MgO (001) substrate. The main features are quite similar to those recorded for the substrate previous to the deposition apart from additional streaks situated in the middle of the MgO streaks, which correspond to the Fe_3O_4 film.

Symmetric scans of the (002) Bragg plane of the substrate were performed in order to confirm the epitaxial relationship of the substrate and thin film. Figure 6.4 shows the $\omega - 2\theta$ rocking curve of the 30 nm Fe_3O_4 film grown on 2.86° miscut MgO(001) substrate. The horizontal axis is shown with reference to the

Bragg angle for symmetric (002) reflection of MgO substrate. From the separation between the film and substrate Bragg peaks, we determine the out of plane lattice constant. The out of plane lattice constants of the film grown on 2.86° and 7° miscut substrate have a value of 0.8370 and 0.8369 nm respectively, indicating the tensile strain state within the plane of the film, in agreement with previous reports [20].

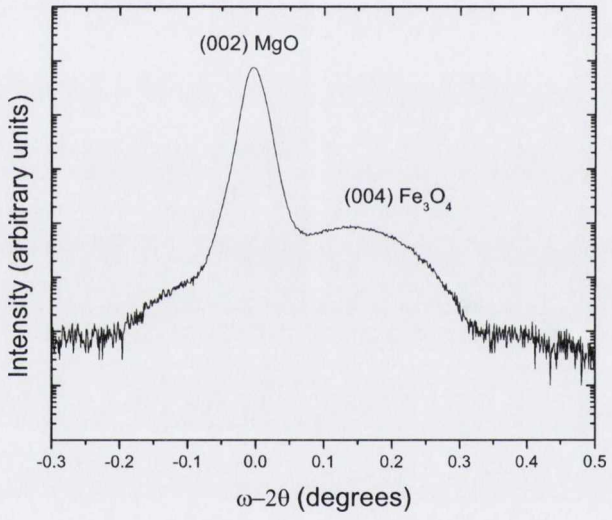

Figure 6.4: $\omega - 2\theta$ scan of 30 nm Fe_3O_4 grown on vicinal MgO(001) with a miscut angle of 2.86° measured relative to the (002) Bragg reflection of MgO.

The full width at half maximum (FWHM) was found to be 0.154° and 0.646° for the 2.86° and 7° samples respectively. The larger FWHM of the 7° miscut sample is representative of the additional scattering contribution arising from the higher density of steps. This broadening can also be interpreted as a change in the microstress structure [21] due to variation of plane spacing in the regions close to the step-edges causing line broadening.

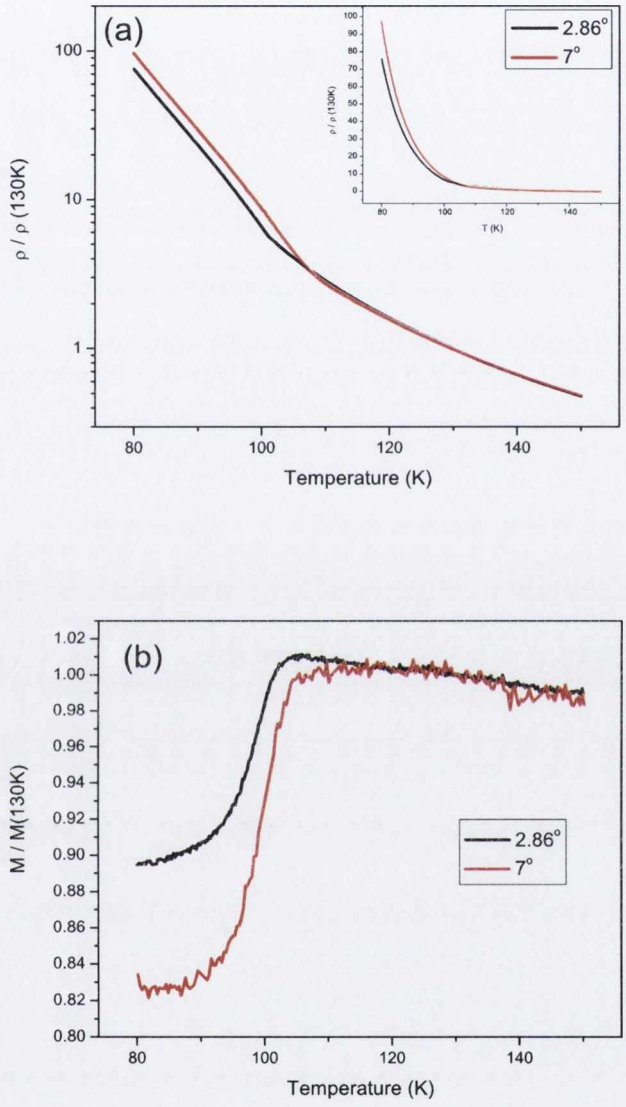

Figure 6.5: Temperature dependence of resistivity and magnetization of 30 nm thick Fe_3O_4 films grown on vicinal substrates, with miscut angles of 2.86 and 7° with respect to (001) along <100> (a)Resistivity along the step edge direction (SE) (inset: linear scale). (b)Magnetization vs temperature measured with a magnetic field of 20 mT applied along SE.

The temperature dependence of the resistivity and magnetization is shown in figure 6.5. Figure 6.5(a) shows the resistivity of the samples measured along the step edge direction and figure 6.5(b) shows the magnetization vs temperature characteristics measured with a magnetic field of 20 mT applied along the steps. All samples showed the characteristic Verwey transition of magnetite, with an increased resistivity and a reduction in magnetization. The magnetization reduction is 10.5% and 17.2% for the samples with miscut of 2.86° and 7° respectively. The Verwey transition temperatures (T_V) determined from maximum slope in the temperature dependence of the magnetization were found to be 98 and 100 K for the film grown on 2.86° and 7° miscut substrate respectively.

6.3.1 Temperature and miscut angle dependence of the magnetization in the samples

We have performed in-plane magnetization measurements with magnetic fields oriented parallel and perpendicular to the direction of step edges (SE) at different temperatures. The magnetization hysteresis loops can give us information about the magnetization reversal mechanism and the magnetic anisotropies present in the system.

Figures 6.6 and 6.7 show the in-plane magnetization hysteresis loops (M-H loops) of 2.86° and 7° miscut samples measured at room temperature (300 K) and at a temperature below the Verwey transition (80 K). As expected for magnetite, the coercivity increases at temperatures below T_V [22]. We have observed a different behaviour of the in-plane M-H loops, when measured with a magnetic field applied across or along the step edges (SE) direction. This is expected to be a consequence of the symmetry breaking introduced by the presence of steps in the system which translates into an uniaxial anisotropy in the magnetization

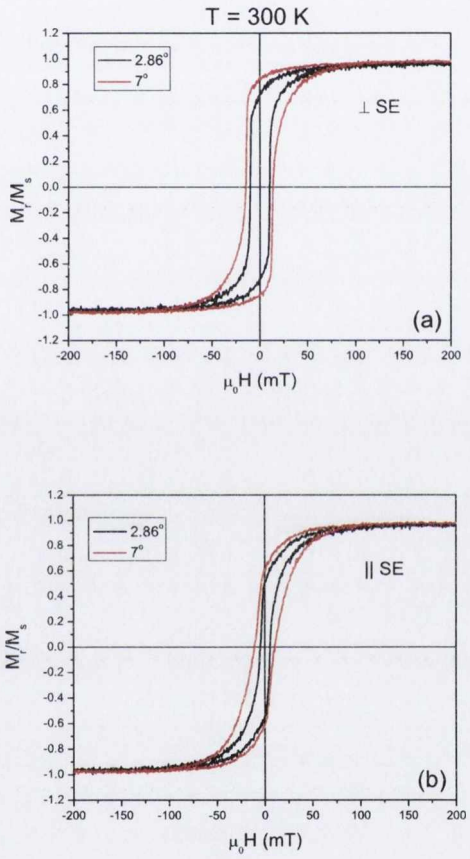

Figure 6.6: Magnetization hysteresis loops measured at 300 K for two samples with different miscut angles with fields applied (a) across or (b) along the step edge direction.

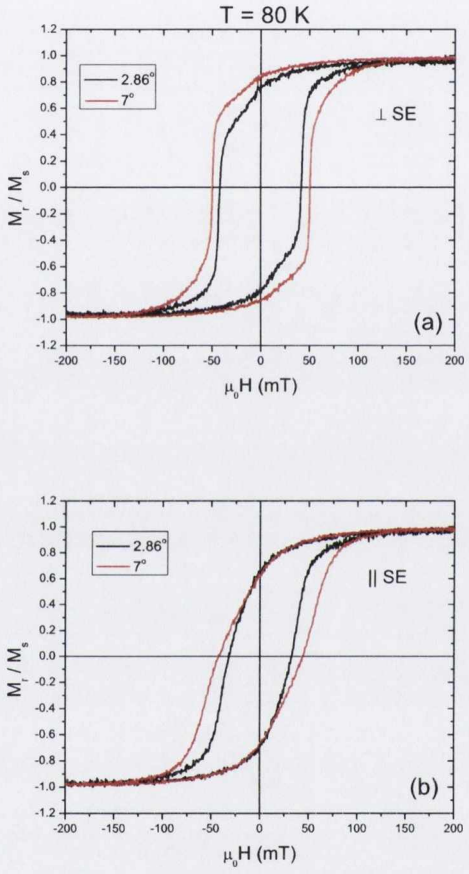

Figure 6.7: Magnetization hysteresis loops measured at 80 K for two samples with different miscut angles with fields applied (a) across or (b) along the step edge direction.

behavior of the films. The M-H loops measured in the direction perpendicular to SE show an increased magnetization remanence (M_r) compared to the loops measured parallel to the SE, this is indicative of the magnetic easy axis character of the direction perpendicular to the SE. This observation is in line with previous FMR studies of Fe_3O_4 films grown on vicinal MgO substrates [19], where a magnetic easy axis was observed in the direction perpendicular to the step edges. It can be observed from figure 6.7(a) that the remanent magnetization at zero field, in the case of loops measured with a magnetic field applied across the step edges, increases with the miscut angle; this can be explained by an increased uniaxial anisotropy for the film grown on the high miscut substrate, therefore when the field is removed there are higher number of domains pointing in the easy axis direction, perpendicular to the steps. As the miscut angle of the samples is decreased the domains would be more evenly oriented, due to the smaller induced uniaxial anisotropy.

In order to understand this result, we need to consider the possible sources of magnetic anisotropy, with particular attention to the case of the broken symmetry impossed by the presence of steps on the system. In any magnetic system the microscopic sources of magnetic anisotropy are mainly the dipole-dipole interaction and the spin-orbit coupling of the system. In the case of stepped surfaces [23] the possible sources of anisotropy are:

- Magnetocrystalline anisotropy due to broken bonds and missing atoms at the step edges [24], which creates uniaxial anisotropy with easy axis either along or perpendicular to the step direction (Neel model).

- Magnetostatic anisotropy originated from the uniaxial roughened surface of films grown on vicinal substrates, the origin of this anisotropy is dipole-dipole interaction [25].

- Magnetoelastic anisotropy due to twofold strain relaxation of the film at the step edges in a direction perpendicular to the steps [26].

The first two mechanisms are not considered here since they are dominant in the case of strong interface or surface contributions for films of a few monolayers. It is known that Fe_3O_4 films grown on MgO(001) substrate remain fully coherent up to thicknesses of several hundred nanometers [20], therefore we will focus our discussion on the effect of the magnetoeleastic induced anisotropy.

The observed differences between magnetization response of vicinal Fe_3O_4 films for magnetic field applied parallel or perpendicular to the step edge (SE) direction can be understood from the fact that atomic-step edges on the surface of the vicinal substrates favour the formation of APBs in Fe_3O_4 films, which produces a highly directional array of APB aligned along the SE directions. The highly directional nature of step induced APBs is expected to induce an anisotropy in the magneto-elastic response of the films. This is due to the fact that APBs can accomodate strain in the films [20]. In light of the above suggestion, one can consider the Fe_3O_4 film as a medium which experiences different extent of strain in two perpendicular directions, parallel or perpendicular to the SE. It is known that the magnetic anistropy can be altered by a modification of the strain status of the film. Recent studies in Fe_3O_4 films show the effect of an uniaxial strain induced within the plane of the film, either mechanically [27] or by the growth of hetero-structures on ferroelectric material [28, 29].

In order to estimate the magnetic contribution arising from strain, we have to minimize the sum of the elastic (F_{el}) and magnetoelastic (F_{me}) energies for a given strain of the system [30]. For a cubic system:

$$F_{me} = b_1 \sum_i \alpha_i^2 \epsilon_{ii} + b_2 \sum_{i>j} \alpha_i \alpha_j \epsilon_{ij} \tag{6.1}$$

$$F_{el} = \frac{c_{11}}{2}\sum_i \epsilon_{ii}^2 + c_{12}\sum_{i>j}\epsilon_{ii}\epsilon_{jj} + \frac{c_4 4}{2}\sum_{i>j}\epsilon_{ij}^2 \tag{6.2}$$

where b_i are the magnetoelastic coupling constants, α_i are the direction cosines of magnetization, ϵ_{ij} are the components of the strain tensor and c_{ij} are the elastic constants. The magnetoelastic constants are related to magnetostriction by [31]:

$$b_1 = -\frac{3}{2}(c_{11} - c_{12})\lambda_{100} \tag{6.3}$$

$$b_2 = -3c_{44}\lambda_{111} \tag{6.4}$$

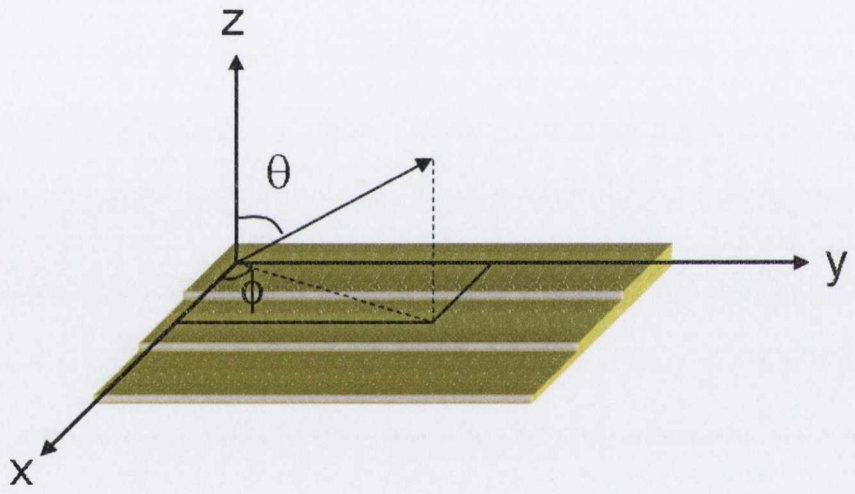

Figure 6.8: Description of the polar geometry, the in-plane orientation is defined by θ=90°.

By finding the minimum of $F_m = F_{me} + F_{el}$ with respect to the strain components, we can obtain the contribution to magnetoelastic anisotropy, which is given below in spherical coordinates (see Fig. 6.8 for a schematic of the geometry):

$$F_m = \frac{1}{2}[b_1(\epsilon_{xx} - \epsilon_{yy})cos2\phi + b_2\epsilon_{xy}sin2\phi]sin^2\theta - \frac{b_1}{2}(1+2\frac{c_{12}}{c_{11}})(\epsilon_{xx}+\epsilon_{yy})cos^2\theta \tag{6.5}$$

The first two terms of the equation describe the in-plane anisotropy and the last term describes the out of plane anisotropy.

In the case of vicinal substrates, there will be a strain relaxation in the direction perpendicular to the steps (x direction), due to the higher density of deffects (APBs) along this direction, therefore $\epsilon_{xx} < \epsilon_{yy}$. If we consider only pure strains ($\epsilon_{xy} = 0$) [27], the equation reduces to:

$$F_m = \frac{1}{2} b_1 (\epsilon_{xx} - \epsilon_{yy}) cos2\phi sin^2\theta - \frac{b_1}{2}(1 + 2\frac{c_{12}}{c_{11}})(\epsilon_{xx} + \epsilon_{yy}) cos^2\theta \tag{6.6}$$

Considering only the first term of equation 6.6 (in-plane case $\theta = 90°$) and the relation of the magnetoelastic constants to the magnetostriction (eq. 6.3):

$$F_m = -\frac{3}{4}(c_{11} - c_{12})\lambda_{100}(\epsilon_{xx} - \epsilon_{yy}) cos2\phi \tag{6.7}$$

with the values of the constants for magnetite; ($c_{11} - c_{12} \simeq 4.85\text{x}10^{10}$ N/m^2 [32], $\lambda_{100} = -19.5\text{x}10^{-6}$ [27]) and $\epsilon_{xx} - \epsilon_{yy} < 0$ we obtain $F_m(\phi = 0) < F_m(\phi = 90)$, which considering the geometry of our system indicates a hard axis behavior in the direction parallel to the step edges, in agreement with the magnetization measurements.

Another possibility to explain the observed magnetization behaviour is related to the spin configuration at the APB and how it is affected by the applied magnetic field. Considering an antiferromagnetic coupling across the step-induced APB and from energy considerations, the spins are expected to orient in the plane of the APB and roughly perpendicular to the magnetic field [33], analogous to the spin-flop region in an antiferromagnet. Therefore for magnetic field applied across the step edges, the spin moments at the APB will orient perpendicular to the field and in the plane of the APB (i.e. parallel to the step edges). In contrast, when the field is applied along the steps the only possible direction for the spins to point perpendicular to the field, and in the APB plane, is the out of plane direction, therefore there will be an energy competition between the shape anisotropy of the film and the antiferromagnetic exchange across the APB. This

in turn makes the direction parallel to the step edges less energetically favorable and thus presenting a hard axis behaviour.

6.3.2 Angular dependence of the anisotropic magnetoresistance

We have performed measurements of the angular dependence of the anisotropic magnetoresistance at different temperatures for currents applied along and across the step edge direction. Both directions were probed simultaneously by performing measurements in two hall bars which had their current paths oriented parallel and perpendicular to the step edge direction respectively.
The anisotropic magnetoresistance (AMR) is believed to be the transport equivalent of the magneto-crystalline anisotropy and to be caused by the spin-orbit interaction, which gives rise to a magnetization direction dependent scattering rate. Recalling equation 3.4, the AMR ratio is usually defined by:

$$AMR = \frac{\rho_{\parallel} - \rho_{\perp}}{\rho_{ave}}$$

where $\rho_{\parallel}$ ($\rho_{\perp}$) are the resistivity for current applied parallel (perpendicular) to the magnetization direction and ρ_{ave} is the average resistivity ($\rho_{ave} = \rho_{\parallel}/3 + 2\rho_{\perp}/3$).
In order to extract information from the angular scans measured at different temperatures, we fitted the angular dependence of AMR using the expression 5.4, derived in the previous chapter and reproduced below:

$$\rho(\theta) = a_0 + a_u cos2\theta + a_c cos4\theta \tag{6.8}$$

This equation allows to directly extract information about the uniaxial (a_u) and cubic (a_c) components of AMR, which are proportional to the two-fold and

four-fold angular dependencies respectively.

Figure 6.9 shows comparative results obtained for the angular dependence of AMR at a temperature of 300 K and an applied magnetic field of 5 Tesla for non-vicinal and a vicinal sample, with a miscut of 2.86°, measured parallel and perpendicular to the steps.

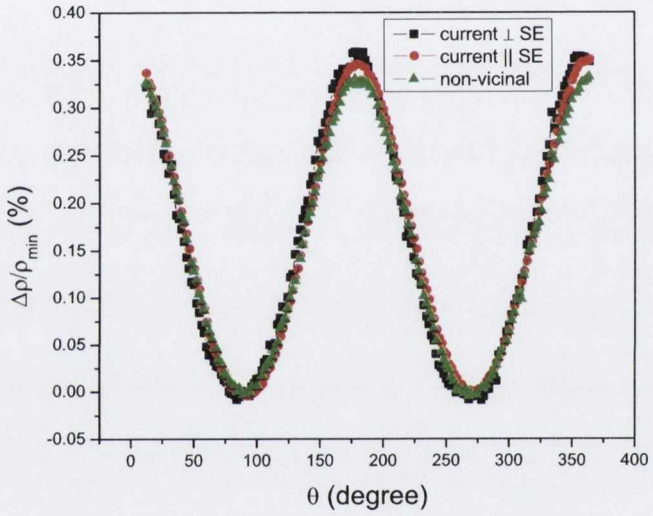

Figure 6.9: Angular dependence of the anisotropic magnetoresistance for non-vicinal (green) and vicinal (black and red) Fe_3O_4/MgO(001) samples at 300 K and an applied field of 5 Tesla. The vicinal sample has a miscut of 2.86° along the <100> direction, meaning that the step edges are along <010> direction

It can be observed that there is not significant difference in the angular behavior of the AMR of non-vicinal and vicinal samples, the data follows the typical $cos^2\theta$ dependence, with peaks at 0° and 180° and valleys at 90° and 270°. At high temperature the angular dependence and magnitude of AMR is similar for all the samples studied with values at 300K around 0.36 ± 0.02 %. Table 6.1

shows the measured values at 300 K and 5 Tesla for all the samples, it can be observed that at this temperature the AMR is insensitive to the presence of steps and its magnitude is in agreement with previously reported values for thin films of magnetite. [34, 35]

Miscut angle (°)	0	2.86		7	
		∥ SE	⊥ SE	∥ SE	⊥ SE
AMR (%)	0.35	0.35	0.36	0.38	0.35

Table 6.1: Magnitude of anisotropic magnetoresistance ratio at 300 K observed for 30 nm Fe_3O_4 films grown on MgO(001) substrates with different miscut angles

As the temperature is decreased below $\sim$ 200K down to temperatures just above Verwey transition (T_V), a deviation from the two-fold symmetry gradually develops with the valleys at 90° and 270° broadening and eventually an additional set of peaks appears. This additional set of peaks is related to an additional four-fold component in the angular dependence of magnetoresistance [36]. In Figure 6.10 we show the angular scan at 120 K measured under an applied magnetic field of 5 Tesla, it can be observed that the angular dependence of the AMR is quite similar for both non-vicinal and vicinal samples and for currents applied across and along the step-edges (SE), with only small differences in the magnitude of the AMR. Table 6.2 shows the AMR ratio as well as the coefficients obtained for the uniaxial a_u and cubic a_c components of anisotropic magnetoresistance.

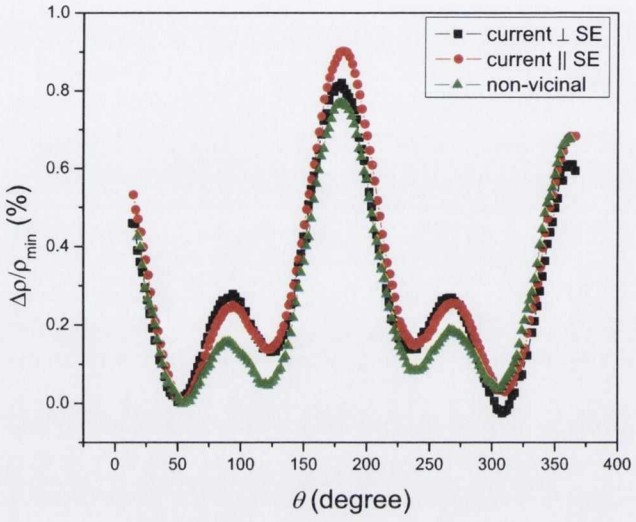

Figure 6.10: Angular dependence of the anisotropic magnetoresistance for non-vicinal (green) and 2.86° miscut sample (black and red), miscut along <100> direction, measured at 120 K and a magnetic field of 5 Tesla.

Miscut angle (°)	0	2.86		7	
		|| SE	⊥ SE	|| SE	⊥ SE
$AMR(\%)$	0.48	0.43	0.36	0.48	0.49
a_u (%)	0.26	0.26	0.21	0.26	0.27
a_c (%)	0.17	0.19	0.19	0.16	0.16

Table 6.2: Values of AMR ratio, uniaxial (a_u) and cubic (a_c) components measured at 120 K and an applied field of 5 Tesla for 30 nm Fe_3O_4 films grown on MgO(001) substrates with different miscut angles

Below the Verwey transition, there is a dramatic change in the features of the AMR's angular response of the vicinal sample as compared to the non-vicinal one. Figure 6.11(a) shows the results obtained at 90 K for an applied field of 5 Tesla, for the non-vicinal as well as the 2.86° miscut sample measured parallel and perpendicular to the step edge direction (SE) (see table 6.3 for the obtained AMR and fitting coefficients). The dependence of the AMR symmetry on the direction of applied current is even more pronounced in the case of the high miscut sample (7° miscut), as can be seen in figure 6.11(b), with an increased AMR and a drastic difference between current applied parallel and perpendicular to the SE direction.

Miscut angle (°)	0	2.86		7	
		$\parallel$ SE	$\perp$ SE	$\parallel$ SE	$\perp$ SE
$AMR(\%)$	-0.66	-0.77	0.61	-3.44	1.67
a_u (%)	-0.25	-0.31	0.38	-1.63	1.00
a_c (%)	0.42	0.26	0.27	0.52	0.63

Table 6.3: Values of AMR ratio, uniaxial (a_u) and cubic (a_c) components measured at 90 K and an applied field of 5 Tesla for 30 nm Fe_3O_4 films grown on MgO(001) substrates with different miscut angles

It is interesting to observe that despite no significant difference in the amplitude of AMR when measured parallel or perpendicular to the step-edges, the angular response is clearly affected, showing different dependence for currents applied parallel or perpendicular to the step edges. For current applied parallel to SE the magnetoresistance scan presents maximums at angles 90° and 270°, while for current perpendicular to SE the maximums are at positions 0° and 180°, these results suggest that presence of miscut on the samples induces an additional uniaxial component in the AMR due to the break of symmetry imposed on the

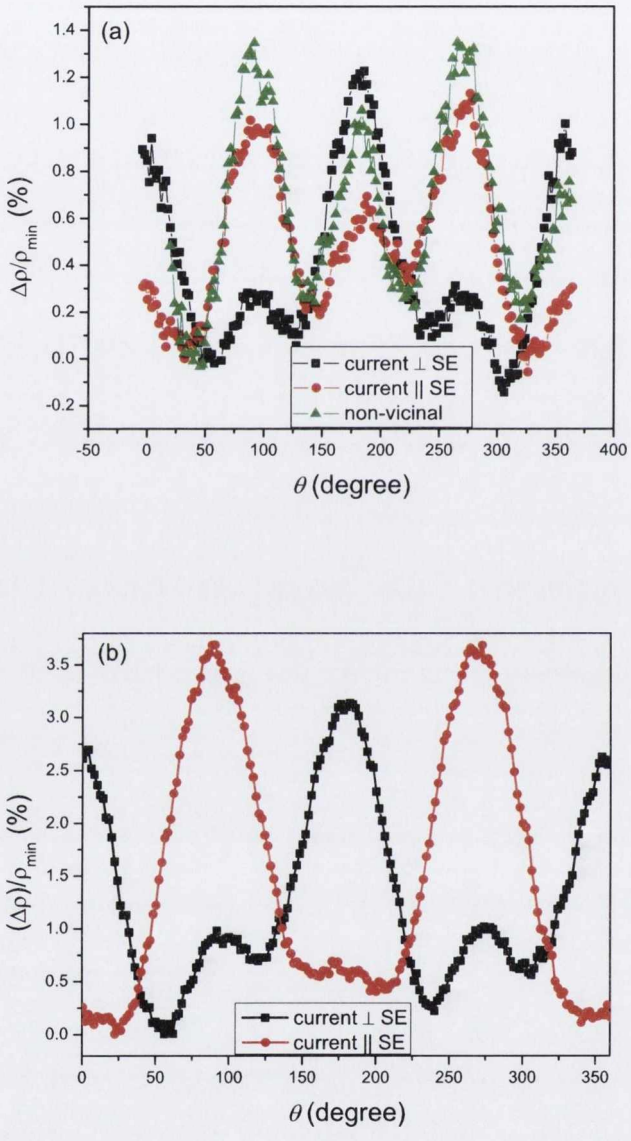

Figure 6.11: Angular dependence of the anisotropic magnetoresistance at 90 K and 5 Tesla for 30 nm thick Fe_3O_4 film grown on: (a)non-vicinal and 2.86° vicinal MgO(001) substrates (b) 30 nm thick Fe_3O_4 film grown on 7° miscut MgO(001) substrate .

system by the presence of atomic steps. One of the interesting features of the observed result is that the effect of the presence of steps in the AMR is only significant at temperatures below the Verwey transition. This could indicate that the physical origin should be connected to that of the metal to insulator (Verwey) transition in magnetite.

Similar behaviour has been observed previously in manganite films grown on substrates with different mismatch strain [37], the effect of the strain on those films manifests itself as a 90° shift in the angular dependence of magnetoresistance (or sign change of AMR ratio) depending on the sign of the mismatch strain of the film, which is quite similar to the currently observed behaviour at temperature below Verwey transition, although this does not explain why we do not observe any difference in AMR at temperatures above T_V.

In order to get better insight into the related mechanism, we performed fittings of the angular dependence of AMR to equation 6.8 to analyze the temperature dependence of the observed effect, from this equation the normalized coefficients a_c and a_u, proportional to the cubic and uniaxial components of AMR, are obtained. These coefficients are plotted in figures 6.12 and 6.13(b). In Fig 6.13(a), we have also shown the AMR ratio as defined on equation 3.4 for a magnetic field of 5 Tesla.

The cubic component, a_c remains unaffected by the presence of steps for all the temperature range of the performed measurements, figure 6.12 shows the cubic component obtained for the 2.86° miscut sample, from fittings of measurements performed with current applied across and along the step edges (SE) under an applied field of 5 Tesla, the magnitude and temperature dependence is quite the same in the other measured samples. In contrast, we can observe that the temperature dependence of the uniaxial component (a_u) follows a behaviour similar to that of the AMR ratio. The magnitude of AMR ratio (a_u component) shows

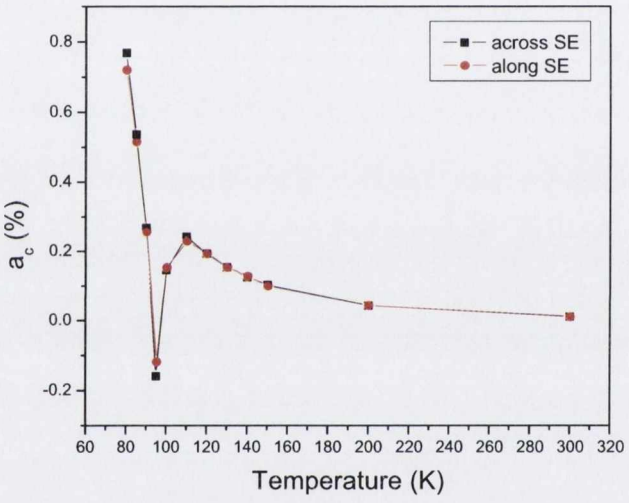

Figure 6.12: Temperature dependence of the cubic AMR component a_c for the Fe_3O_4 film grown on 2.86 ° miscut subtrate. Data was extracted from the angular scans measured at 5 Tesla.

no significant variation above the Verwey transition temperature (T_V) and as the samples are cooled down below T_V, there is a sign change from positive to negative and an increase in the magnitude in the direction parallel to the SE. Whereas in the direction perpendicular to the SE the AMR ratio (a_u) remains positive (see figure 6.13).

In order to understand the origin of the different behaviour of the uniaxial component (AMR ratio) with respect to the miscut direction below T_V, we need to look at the origin of the sign change of a_u and AMR ratio in magnetite. Previous studies of AMR on Fe_3O_4 films [35] have pointed to the relation in the sign change of AMR and the sign change in the anisotropy constant of magnetite in the vicinity of the Verwey transition.

Another possibility, highlighted by Ziese [38], is related to the band structure of magnetite. The starting point of Ziese's description is the AMR model developed for metals with a spin flip scattering term, the AMR ratio can be expressed as:

$$\frac{\Delta\rho}{\rho} = \frac{\rho_\uparrow\Delta\rho_\downarrow + \rho_\downarrow\Delta\rho_\uparrow + \rho_{\uparrow\downarrow}(\Delta\rho_\uparrow + \Delta\rho_\downarrow)}{\rho_\uparrow\rho_\downarrow + \rho_{\uparrow\downarrow}(\rho_\uparrow + \rho_\downarrow)} - \frac{\Delta\rho_\uparrow + \Delta\rho_\downarrow}{\rho_\uparrow + \rho_\downarrow + 4\rho_{\uparrow\downarrow}} \tag{6.9}$$

where $\rho_\uparrow$, $\rho_\downarrow$ are the resistivities associated with the majority, minority spin channels respectively, $\rho_{\uparrow\downarrow}$ is the spin-flip scattering resistivity [38] (this term was introduced by Fert [39] to describe the contribution of spin wave-electron collisions to the mixing of the spin up and spin down currents) and the resistivity anisotropy between longitudinal and transversal resistivity in the minority (majority) spin channel is given by $\Delta\rho_\downarrow$ ($\Delta\rho_\uparrow$), these resistivity anisotropies have been found to be a function of the channel resistivities and can be expressed as: [40]

$$\Delta\rho_\uparrow = \gamma_{\uparrow\uparrow}\rho_\uparrow + \gamma_{\uparrow\downarrow}\rho_\downarrow \tag{6.10}$$

$$\Delta\rho_\downarrow = \gamma_{\downarrow\uparrow}\rho_\uparrow + \gamma_{\downarrow\downarrow}\rho_\downarrow \tag{6.11}$$

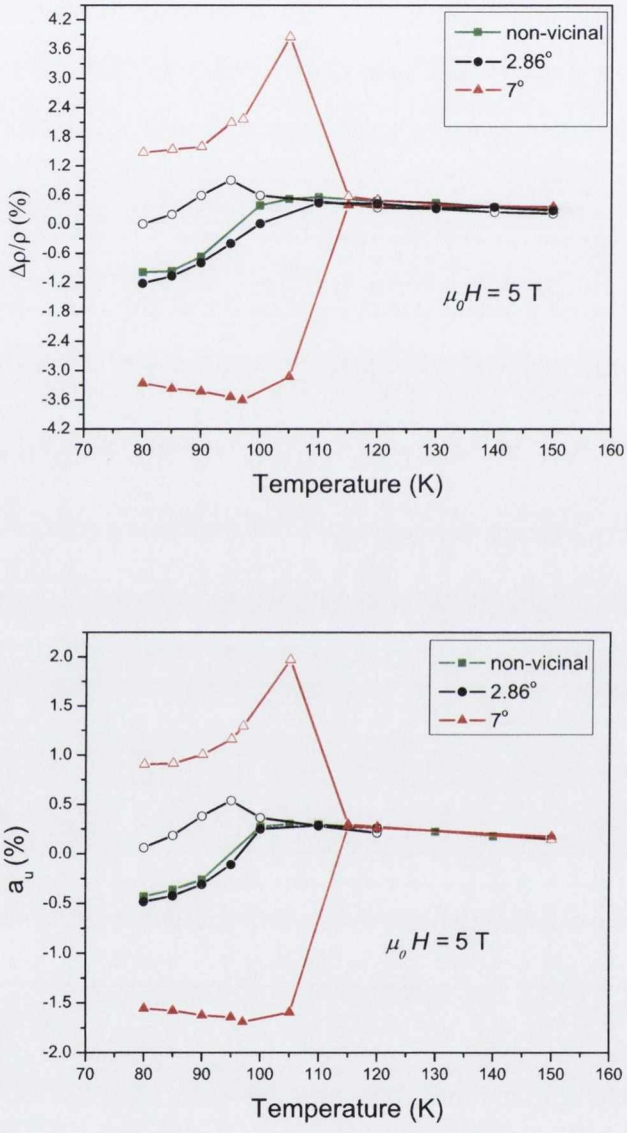

Figure 6.13: Temperature dependence of the (a)anisotropic magnetoresistance ratio ($\Delta\rho/\rho$) and (b)normalized uniaxial component (a_u) extracted from angular magnetoresistive scans measured under an applied magnetic field of 5 Tesla, for 30 nm thick Fe_3O_4 films grown on non-vicinal and vicinal MgO(001) substrate miscut with respect to the (001) plane along the <100> direction (miscut angles: 2.86° and 7°). Filled/empty symbols correspond to direction parallel/perpendicular to the step edges respectively.

The γ_{ij}'s coefficients have been calculated by Malozemoff [41] considering the effect of spin-orbit coupling, exchange and the crystal field on the atomic d wave functions.

At high temperatures, above T_V, the AMR ratio in magnetite has been measured to be positive with a magnitude of $\sim$ 0.3%. The calculation of AMR within a one-band model, considering conduction by minority spin only, since magnetite is predicted to be a half metal with a majority spin gap, yields a magnetoresistance:

$$\frac{\Delta\rho}{\rho} = \gamma_{\downarrow\downarrow} \tag{6.12}$$

This coefficient in the case of conduction by means of t_{2g} electrons is given by:

$$\gamma_{\downarrow\downarrow} = -\frac{3}{4}\frac{\lambda^2}{\Delta_{cf}^2} \tag{6.13}$$

considering appropriate values for magnetite, the spin orbit coupling λ=0.04 eV [38] and the crystal field splitting Δ_{cf}=1.75 eV [42] a value of $\Delta\rho/\rho$= -0.04 % is obtained, this value has the opposite sign and is one order of magnitude smaller. In order to explain this discrepancy, Ziese [38] considered the presence of a majority spin band close to the Fermi level which could be identified with the majority e_g band [43, 44, 45], this is further supported by the small spin polarization values obtained for magnetite [42, 46]. Therefore the AMR defined using a two band model (equations 6.10), when scattering is due to t_{2g} minority electrons and e_g majority electrons, with the coefficients given by Malozemoff [41]:

$$\gamma_{\uparrow\uparrow} = -\frac{3}{4}\frac{\lambda^2}{(H_{ex} - \Delta_{cf})^2} - \frac{\lambda^2}{\Delta_{cf}^2} \tag{6.14}$$

$$\gamma_{\uparrow\downarrow} = \frac{3}{4}\frac{\lambda^2}{(H_{ex} - \Delta_{cf})^2} \tag{6.15}$$

$$\gamma_{\downarrow\uparrow} = 0 \tag{6.16}$$

$$\gamma_{\downarrow\downarrow} = -\frac{3}{4}\frac{\lambda^2}{\Delta_{cf}^2} \tag{6.17}$$

these coefficients can be calculated using the previously used spin-orbit coupling energy and crystal field splitting, considering the exchange field for magnetite H_{ex}=2.5 eV [47], the following values for the coefficients are obtained $\gamma_{\uparrow\uparrow}$=-0.17 %, $\gamma_{\uparrow\downarrow}$=0.21 %, and $\gamma_{\downarrow\downarrow}$=-0.04 %.

The AMR in this two-band model is given by

$$\frac{\Delta\rho}{\rho} = \gamma_{eff}(\alpha - 1) \tag{6.18}$$

this expression has been obtained from equation 6.9, with

$$\gamma_{eff} = \frac{-\gamma_{\downarrow\downarrow} + \gamma_{\uparrow\downarrow}\alpha(1+4\beta) - 4\gamma_{\uparrow\uparrow}\alpha\beta^2}{[1+\beta(1+\alpha)][1+\alpha+4\alpha\beta]} \tag{6.19}$$

with $\alpha = \rho_\downarrow/\rho_\uparrow$, the minority to majority resistivity ratio and $\beta = \rho_{\uparrow\downarrow}/\rho_\downarrow$ the reduced spin-flip scattering resistivity. Values of AMR obtained using the previous equation are shown in figure 6.14 and are the same as those obtained by Ziese [38], obtaining an AMR of ~0.3% for α ~3 and β <0.1.

Below T_V, due to the gap opening, the e_g electrons move away from the Fermi level, therefore the one band case is eventually reached with a negative AMR. Although the magnitude of AMR obtained previously with the one band model is too small to quantitatively explain the experimental data, it provides a qualitative explanation for the behavior observed for $T < T_V$ in non-vicinal and vicinal samples with current applied parallel to the step-edges (SE).

Due to the presence of atomic steps, a higher probability of formation of regular array of APBs along the step edges is expected. The nature of the exchange interaction across this APBs is expected to be predominantly antiferromagnetic, due to 180° cation-anion-cation bonding (see Figure 6.1). As a consequence of the periodical nature of the APBs a spin down conduction electron moving across step edges can be scattered by electrons with spin up character. Therefore conduction could be expected to present a two-band character. We considered this effect as

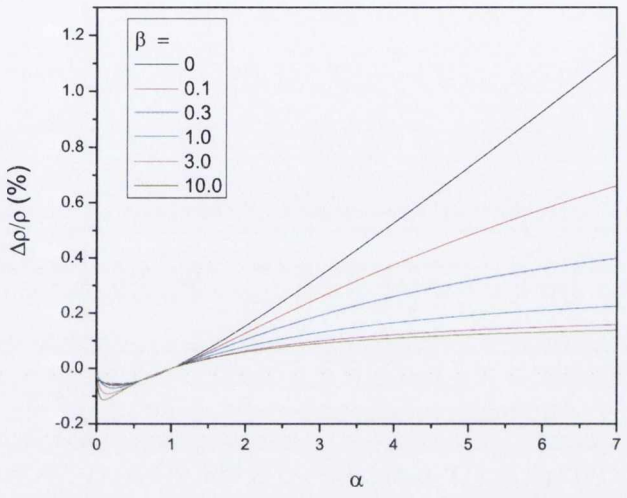

Figure 6.14: AMR two-band model for magnetite as a function of the minority to majority resistivity ratio α for different spin-flip scattering β. Reproduced from [38]

an effective t_{2g} majority band and follow similar procedures as in the previous two-band AMR calculation obtaining the following γ coefficients [41]:

$$\gamma_{\uparrow\uparrow} = -\frac{3\lambda^2}{4\Delta_{cf}^2} \tag{6.20}$$

$$\gamma_{\uparrow\downarrow} = \frac{3\lambda^2}{4(H_{ex} + \Delta_{cf})^2} \tag{6.21}$$

$$\gamma_{\downarrow\uparrow} = \frac{3\lambda^2}{4(H_{ex} - \Delta_{cf})^2} \tag{6.22}$$

$$\gamma_{\downarrow\downarrow} - \frac{3\lambda^2}{4\Delta_{cf}^2} \tag{6.23}$$

With the coefficients $\gamma_{\uparrow\uparrow}$=-0.04%, $\gamma_{\uparrow\downarrow}$=0.21%, $\gamma_{\downarrow\uparrow}$=0.01%, and $\gamma_{\downarrow\downarrow}$=-0.04% and combining equations 6.9 and 6.10 we obtain the following expression for AMR:

$$\frac{\Delta\rho}{\rho} = \frac{\gamma_{\downarrow\uparrow}(\alpha^{-1} + 4\beta + 4\alpha\beta^2) + \gamma_{\downarrow\downarrow}(1 + 2\alpha\beta)^2 + \gamma_{\uparrow\downarrow}\alpha^2(1 + 2\beta)^2 + \gamma_{\uparrow\uparrow}\alpha(1 + 2\beta)^2}{[1 + \beta(1 + \alpha)][1 + \alpha + 4\alpha\beta]} \tag{6.24}$$

The anisotropic magnetoresistance as a function of the channel resistivity ratio is shown in figure 6.15, it can be observed that the AMR is positive for all values of α and β. The initial part of the curve (small α), shows increased positive AMR values. Although this model can explain the relatively higher positive values of AMR for the film grown on high miscut substrate, the relation between α and the presence of APBs remains unclear. After all magnetite is a strongly correlated oxide with polaronic effects and the application of a theory developed for metals might be doubtful. Further investigations are required, in order to clarify the effect of a regular array of APBs on the band structure of magnetite.

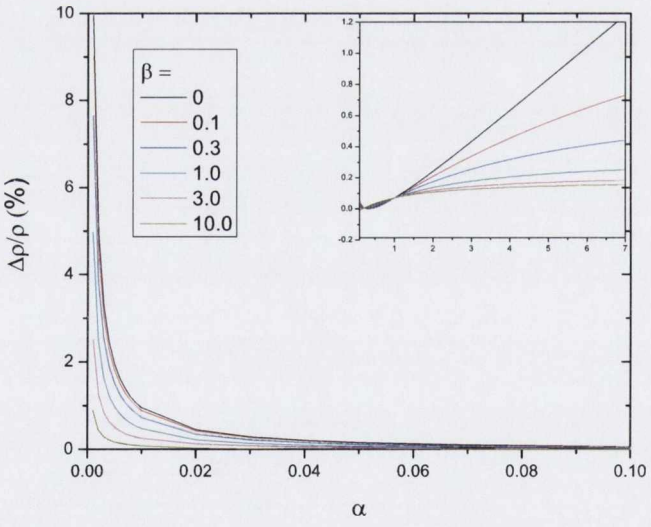

Figure 6.15: APB induced two-band model of AMR for magnetite as a function of the minority to majority resistivity ratio α for different spin-flip scattering β.

6.4 Conclusion

We presented results obtained on magnetization and anisotropic magnetoresistance properties of 30 nm thick Fe_3O_4 films grown on non-vicinal and vicinal MgO(001) substrates. The vicinal substrates presented a miscut angle of 2.86° and 7° with respect to the (001) plane along the <100> direction. The results show that the samples present a easy magnetization direction in the direction perpendicular to the steps, which can be understood in terms of different strain status of the films for directions parallel and perpendicular to the step edges, since the APBs are know to accomodate the strain of the Fe_3O_4 films [20], therefore the highly directional alignment of the step-induced APBs is expected to result in an anisotropy in the strain within the plane of the film.

The effect of the presence of steps on the AMR response presents two regions, above and below the Verwey transition (T_V). Above T_V there is not significant effect of the presence of steps on the AMR of the films. In contrast, below the Verwey transition the AMR characteristic changes dramatically depending on the direction of applied current with respect to the step edges. The symmetry of the AMR is affected by the presence of steps, this effect has been possibly related to the effect of the APBs on the conduction electrons below T_V.

Our measurements suggest that ab-initio studies are required to clarify the effect of the APBs on the strain relaxation and its effect on the magnetic and transport properties as well as the effect of highly regular APB array on the band structure of magnetite.

References

[1] Maranville, B. B., Shapiro, A. L., Hellman, F., Schaadt, D. M., and Yu, E. T. *Appl. Phys. Lett.* **81**, 517 (2002).

[2] Degroote, B., Major, M., Meersschaut, J., Dekoster, J., and Langouche, G. *Surf. Sci.* **482-485**, 1090 (2001).

[3] Usov, V., Murphy, S., and Shvets, I. V. *J. Appl. Phys.* **95**, 7312 (2004).

[4] Naguyen-Van-Dau, F., Sissaiu, M., Schuhl, A., and Galtier, P. *J. Appl. Phys.* **81**, 4482 (1997).

[5] Sugahara, S. and Tanaka, M. *Appl. Phys. Lett.* **80**, 1969 (2002).

[6] Zhao, D., Lui, F., Huber, D. L., and Lagally, M. G. *J. Appl. Phys.* **91**, 3150 (2002).

[7] Gong, G. Q., Gupta, A., Xiao, G., Qian, W., and Dravid, V. P. *Phys. Rev. B* **56**, 5096 (1997).

[8] Li, X. W., Gupta, A., Xiao, G., and Gong, G. Q. *J. Appl. Phys.* **83**, 7049 (1998).

[9] Wu, H. C., Arora, S. K., Mryasov, O. N., and Shvets, I. V. *Appl. Phys. Lett.* **92**, 182502 (2008).

[10] Lee, S., Fursina, A., Mayo, J. T., Yavuz, C. T., Colvin, V. L., Sofin, R. G. S., Shvets, I. V., and Natelson, D. *Nat. Mat.* **7**, 130 (2008).

[11] Eerenstein, W., Palstra, T. T. M., Hibma, T., and Celotto, S. *Phys. Rev. B* **68**, 014428 (2003).

[12] Sofin, R. G. S., Arora, S. K., and Shvets, I. V. *J. Appl. Phys.* **97**, 10D315 (2005).

[13] Celotto, S., W.Erenstein, and Himba, T. *Eur. Phys. J. B* **36**, 271 (2003).

[14] Eerenstein, W., Palstra, T. T. M., Saxena, S. S., and Hibma, T. *Phys. Rev. Lett.* **88**, 247204 (2002).

[15] Margulies, D. T., Parker, F. T., Spada, F. E., Goldman, R. S., Li, J., Sinclair, R., and Berkowitz, A. E. *Phys. Rev. B* **53**, 9175 (1996).

[16] Shvets, I. V., Mariotto, G., Jordan, K., Berdunov, N., Kantor, R., and Murphy, S. *Phys. Rev. B* **70**, 155406 (2004).

[17] Mariotto, G., Murphy, S., and Shvets, I. *Phys. Rev. B* **66**, 245426 (2002).

[18] Arora, S. K., Sofin, R. G. S., and Shvets, I. V. *Phys. Rev. B* **72**, 134404 (2005).

[19] McGuigan, L., Barklie, R. C., Sofin, R. G. S., Arora, S. K., and Shvets, I. V. *Phys. Rev. B* **77**, 174424 (2008).

[20] Arora, S. K., Sofin, R. G. S., Shvets, I. V., and Luysberg, M. *J. Appl. Phys.* **100**, 073908 (2006).

[21] Cullity, B. D. and Graham, C. D. *Introduction to magnetic materials.* John Willey & Sons, Inc, Hoboken, New Jersey, (2009).

[22] Bohra, M., Prased, S., Venketaramani, N., Kumar, N., Sahoo, S. C., and Krishnan, R. *J. Magn. Magn. Mater.* **321**, 3738 (2009).

[23] Mathews, M., Postma, F. M., Lodder, J. C., Jansen, R., Rijnders, G., and Blank, D. H. A. *Appl. Phys. Lett* **87**, 242507 (2005).

[24] Chuang, D. S., Ballentine, C. A., and O'Handley, R. C. *Phys. Rev. B* **49**, 15084 (1994).

[25] Arias, R. and Mills, D. L. *Phys. Rev. B* **59**, 11871 (1999).

[26] Jaffres, H., Bertrand, D., Fert, A. R., Vogel, J., Fontaine, A., and Brookes, N. B. *Phys. Rev. B* **63**, 174411 (2001).

[27] Brandlmaier, A., Geprägs, S., Weiler, M., Boger, A., Opel, M., Huebl, H., Bihler, C., Brandt, M. S., Botters, B., Grundler, D., Gross, R., and Goennenwein, S. T. B. *Phys. Rev. B* **77**, 104445 (2008).

[28] Vaz, C. A. F., Hoffman, J., Posadas, A.-B., and Ahn, C. H. *Appl. Phys. Lett.* **94**, 022504 (2009).

[29] Tian, H. F., Qu, T. L., Luo, L. B., Yang, J. J., Guo, S. M., Zhang, H. Y., Zhao, Y. G., and Li, J. Q. *Appl. Phys. Lett.* **92**, 063507 (2008).

[30] Vaz, C. A. F. *arxiv* **0811**, 2146 (2008).

[31] Chikazumi, S. *Physics of Ferromagnetism.* Oxford University Press, (1997).

[32] Goto, T. and Lüthi, B. *Adv. Phys.* **52**, 67 (2003).

[33] Kalev, L. A. and Niesen, L. *Phys. Rev. B* **67**, 224403 (2003).

[34] Jin, X., Ramos, R., Zhou, Y., McEvoy, C., and Shvets, I. V. *J. Appl. Phys.* **99**, 08C509 (2006).

[35] Ziese, M. and Blythe, H. J. *J. Phys: Condens. Matter* **12**, 13 (2000).

[36] Ramos, R., Arora, S. K., and Shvets, I. V. *Phys. Rev. B* **78**, 214402 (2008).

[37] Li, Q., Wang, H. S., Hu, Y. F., and Wertz, E. *J. Appl. Phys.* **87**, 5573 (2000).

[38] Ziese, M. *Phys. Rev. B* **62**, 1044 (2000).

[39] Fert, A. *J. Phys. C: Sol. State Phys.* **2**, 1784 (1969).

[40] Muth, P. and Christoph, V. *J. Phys. F: Metal Phys.* **11**, 2119 (1981).

[41] Malozemoff, A. P. *Phys. Rev. B* **34**, 1853 (1986).

[42] Alvarado, S. F., Erbudak, M., and Munz, P. *Phys. Rev. B* **14**, 2740 (1976).

[43] Anisimov, V. I., Elfimov, I. S., Hamada, N., and Terakura, K. *Phys. Rev. B* **54**, 4387 (1996).

[44] Jeng, H.-T. and Guo, G. Y. *Phys. Rev. B* **65**, 094429 (2002).

[45] Piekarz, P., Parlinski, K., and Olés, A. M. *Phys. Rev. B* **76**, 165124 (2007).

[46] Li, X. W., Gupta, A., Xiao, G., Qian, W., and Dravid, V. P. *Appl. Phys. Lett* **73**, 3282 (1998).

[47] Camphausen, D. L., Coey, J. M. D., and Chakraverty, B. K. *Phys. Rev. Lett.* **29**, 657 (1972).

Chapter 7

Magneto-transport properties of Fe_3O_4 probed using contacts with nano-scale gap

7.1 Introduction

The epitaxial Fe_3O_4 films grown on MgO(001) substrates are known to suffer from the presence of antiphase boundaries (APBs) [1, 2, 3]. Eerenstein et al. [4, 5, 6, 7] performed an extensive study of the properties of APBs on Fe_3O_4 epitaxial films, their microstructure and physical properties (conductivity, magneto-resistance and magnetisation) were analyzed. They found that the APB domain size increases significantly with film thickness and shows a parabolic relation $D \propto \sqrt{t}$ where D is the domain size and t is the deposition time (proportional to the thickness of the film). The presence of APB in the films are known to affect the physical properties such as a non-saturation of magnetization [8] due to the induced antiferromagnetic (AF) coupling [1], an increased resistivity with the

decrease of film thickness [4] and the magnetoresistance (MR) of the films is increased [5], compared to the single crystals [9].

It was also shown that through the manipulation of these defects, the MR behavior of epitaxial Fe_3O_4 films can be improved [10, 11], which suggests that such manipulated defects might be an attractive tool for technological applications. Therefore, measuring the MR of one antiferromagnetic APB (AF-APB) is highly interesting because it occurs on even very short length scale and a very large MR ratio across one AF-APB is expected [5]. Despite all of the intensive research over the last decade, unfortunately, nobody measured the magneto-transport properties through a single AF-APB or a single magnetite domain. There are two main complications. First, an anti-ferromagnetic coupling is not always present across the APBs [7]. This complicates making device structures because not all APBs give an MR effect. Second, the domain size is small which complicates the fabrication of electrical contacts.

In this study we have demonstrated the feasibility to probe one AF-APB and a single magnetic domain of Fe_3O_4 epitaxial films using a pair of contacts with a nanoscale gap fabricated using electron beam lithography (EBL). Our experiments clearly show that, in the case of probing an AF-APB, a large magnetoresistance, high resistivity, and a high saturation field are observed compared to the case of probing a single Fe_3O_4 domain.

7.2 Experiment

The Fe_3O_4 films used in the present study were grown on (001) oriented MgO single crystal substrates using oxygen plasma assisted molecular beam epitaxy system (DCA MBE M600) with a base pressure of 5 x 10^{-10} Torr. More details about the growth procedure can be found elsewhere [11]. Reflection high energy

electron diffraction (RHEED) was employed to confirm the epitaxial growth and establish the growth mode. The presence of the RHEED intensity oscillations confirms that the films grew in a layer-by-layer mode with a growth rate of 0.3 $\AA$/s. A multicrystal high-resolution x-ray diffractometer was used to confirm the single phase structural and epitaxial nature of the Fe_3O_4 films. Device fabrication was carried out by EBL using a single layer positive tone resist PMMA supplied by MicroChem Corp. After development, thick metal contacts consisting of Ti (5 nm) / Au (50 nm) were deposited through evaporation. All these nanogap contacts are along <100> or <010> directions of the films. Subsequently, after liftoff by using acetone, UV lithography has been carried out in order to have macroscopic metal contacts. The resistance was examined by means of physical property measurement system (PPMS). All microstructures were fabricated on Fe_3O_4 epitaxial thin film of 60 nm.

7.3 Results and discusion

Figure 7.1(a) shows a typical schematic drawing of TEM dark field images of epitaxial Fe_3O_4 film. In order to measure a single AF-APB or a single magnetite domain, 60 nm films were grown and EBL technique was used to pattern the contacts with different size gap on the film surface. It is known that the domain size in magnetite film dependens on the thickness [6]. For a 60 nm thick Fe_3O_4 film, the average domain size is around 50 nm and the thickness of APB is around 2-3 nm. Therefore, in order to make sure we measure at least one APB but less than 3 APB, the gap of the contact should be between 50 to 100 nm (Figure 7.1(b)). To probe a single magnetite domain, a pair of contacts with a gap less than 50 nm is necessary (Figure 7.1(c)). The lateral geometry of the devices is shown in Figure 7.1(d) with a nanogap of 30 nm.

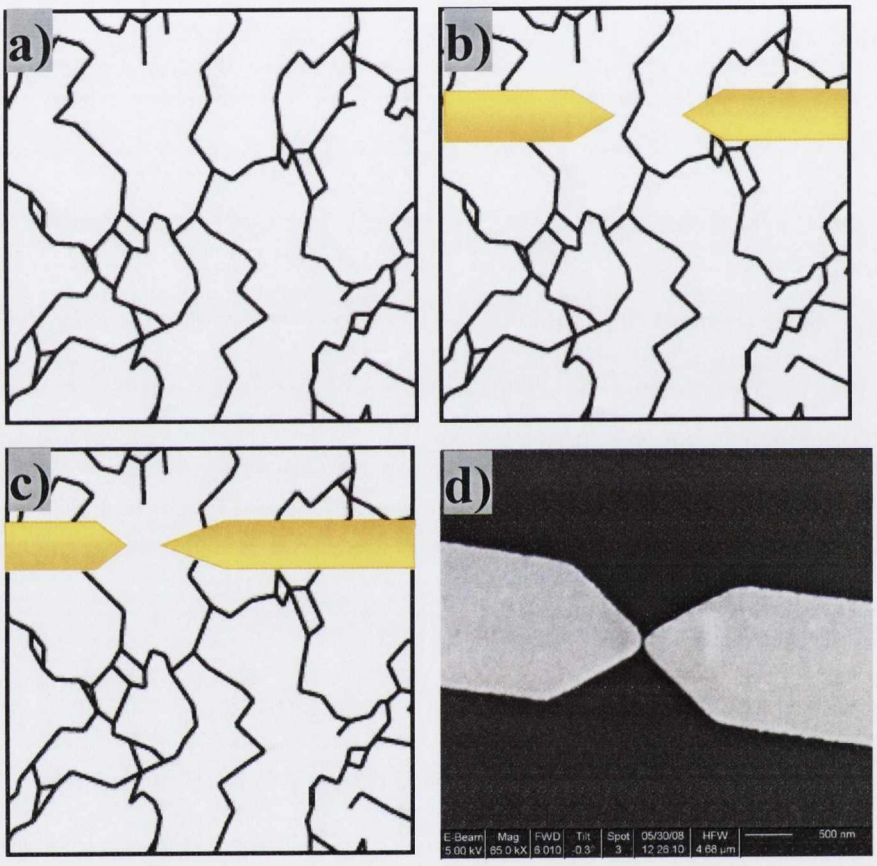

Figure 7.1: Schematic of APB in magnetite thin film (a), Schematic of the setup to probe a single APB (b) and a single domain (c), SEM image of contact with 30 nm gap (d).

The resistances were measured using two probes for both current and voltage bias measurements due to the devices' design. Although in this configuration the resistance measured is the sum of $R_{sample} + R_{leads} + R_{contact}$, the devices were designed to reduce R_{leads} giving a maximum error of 10 %. As we will see below $R_{contact}$ can also be neglected in this case. Therefore we consider the measured resistances to correspond to R_{sample}.

For probing one AF-APB, the gap between the contacts is around 80 nm and the resistivity is around 0.029 Ωcm at room temperature, which is one order of magnitude larger than the bulk value of 0.005 Ωcm and is also larger than the value of 60 nm thick Fe_3O_4 films (0.011 Ωcm). For probing single domain magnetite, the gap between the contacts is around 30 nm. The resistivity measured in this case is one order of magnitude smaller than that for probing one AF-APB, with a value of 0.0026 Ωcm at room temperature. We found that the single domain resistivity is even less than the bulk value. This observation is consistant with the assumption of the narrow gap measurements corresponding to a defect free single domain case. This very small resistivity allows us to investigate the very low temperature transport properties of magnetite thin films, it is worth noting that for the 30nm gap, the MR could be measured down to temperature of 40 K.

Figure 7.2(a) shows the MR measurements (up to 2 T) for the case of probing one AF-APB with the in-plane external field applied along the current direction. The magnetoresistance shows a linear response to the external magnetic field at all temperatures, which suggests we are measuring one AF-APB [5, 12].

Figure 7.2(b) shows the MR ratio (up to 2 T applied field) as a function of temperature. A MR ratio of -1.8 % was achieved at room temperature. We can also notice from Figure 7.2(b) that the MR ratio increases as the temperature is decreased and peaks at the Verwey transition temperature. Further decrease in

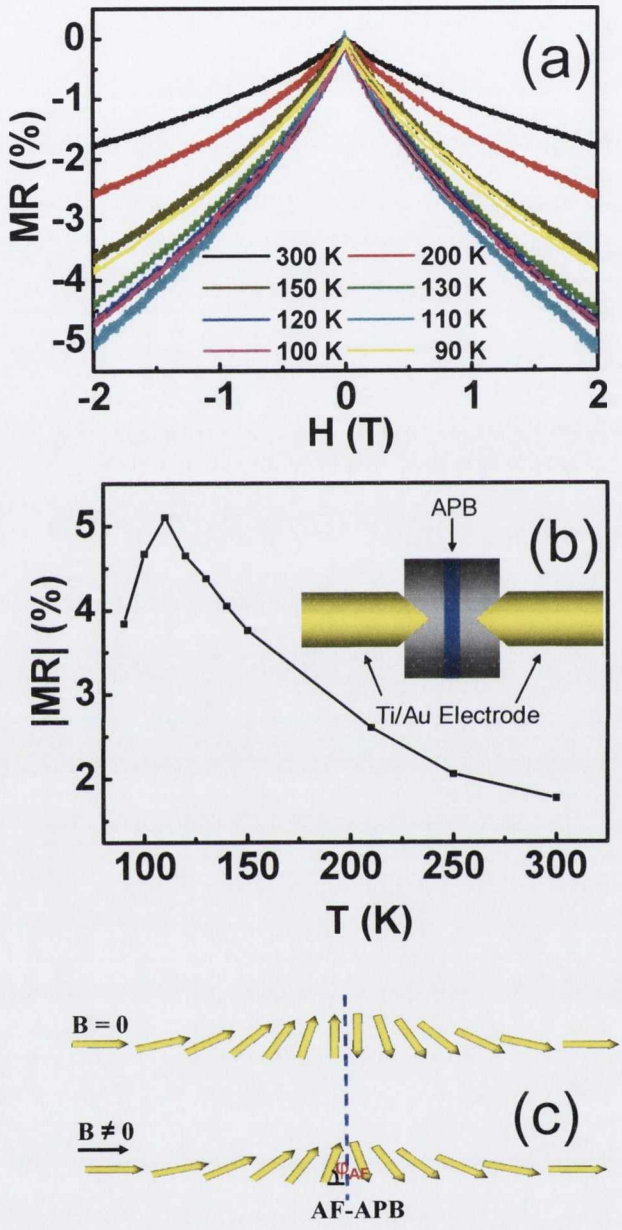

Figure 7.2: (Color online) Magneto resistance vs field curve at different temperature (a) and MR ratio at 2 Tesla field as a function of temperature (b) for the case of probing one AF-APBs. (c) Schematic drawing of spin structure at the AF-APB with and without an in-plane external field.

the temperature leads to a lowering of the MR ratio. We would like to mention that the shape of the MR curve in this case is independent of temperature. We assume that magnetotransport properties of the 80 nm gap nanoscale device are dominated by transport across the AF-APB, which is consistent with the observed linear response to the external field. The conductivity for probing a single AF-APB can be written in the following form:

$$\sigma = \sigma_0 + t_0^2 cos^2 \phi_{AF} \tag{7.1}$$

where σ_0 is due to the spin-dependent scattering at the interface without and external field and the second term is responsible for the MR effect. ϕ_{AF} (see 7.2(c)) is the angle between the spins at the APB and the external magnetic field, where $\phi_{AF} = 0$ and $\phi_{AF} = \pi/2$ correspond to the cases for probing a single domain and one AF-APB, respectively. Using the values from the resistivity measurements, we get $\sigma_0 = 34.48(1/\Omega cm)$ and $t_0^2 = 350.1(1/\Omega cm)$. In a 2 T external field, the conductivity increases to 35.1 $(1/\Omega cm)$ and ϕ_{AF} rotates to 87.6 °, which is still close to $\pi/2$. Using equation 4 in [5], we get

$$A_{AF} = -\sqrt{A_F d^2 \mu_0 H M_S / (cos^2 \phi_{AF} + cos^3 \phi_{AF})} \tag{7.2}$$

where H is the external field and M_S is the saturation magnetization. A_{AF} is the exchange stiffness for the AF exchange interaction at the boundary. A_F is the exchange stiffness for the ferromagnetic coupling of the spins, and d is the average distance between two neighbouring spin chains along the boundary. Taking the literature value for $A_F = 3K$ [1] and d is set to 5 Å[12], we get A_{AF} around -27.6 K, which is slightly larger than the literature value (-25 K) stimated by Motida el al. [13], this supports our assumption that the $R_{contact}$ could be neglected and to the best of our knowledge is the first evaluation of A_{AF} accross an AF-APB on the basis of transport measurements. For this strong AF coupling, a magnetic

field can align the spins far from the boundary, whereas the spins close to the boundary still require a stronger external field to align.

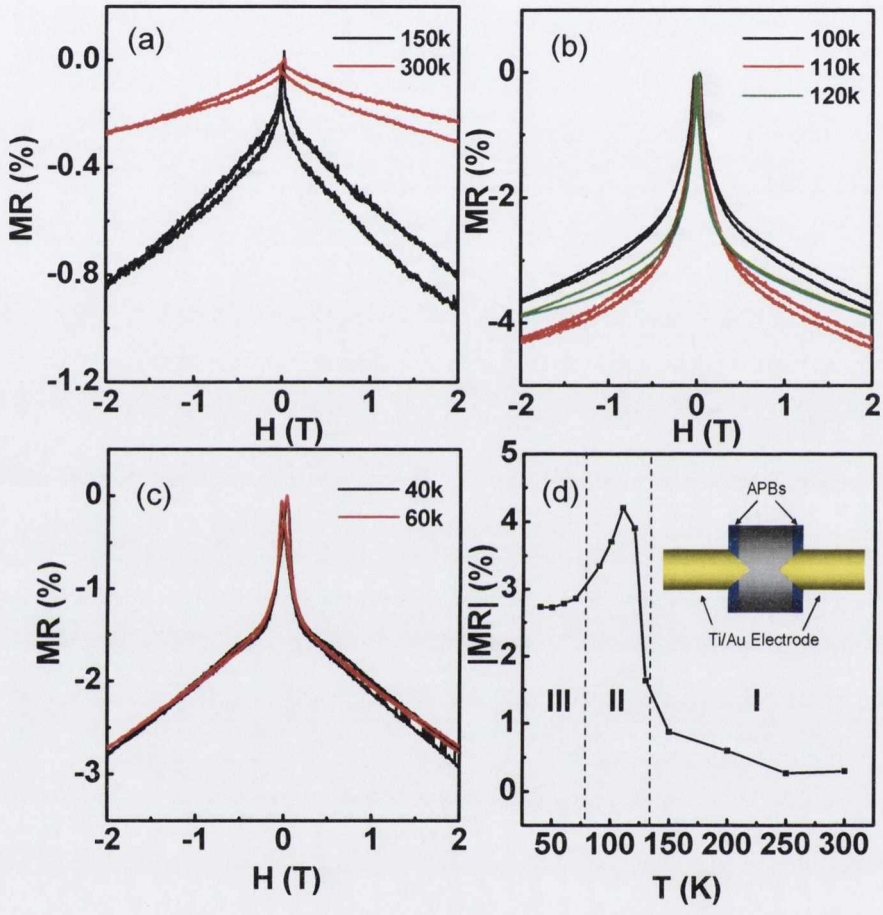

Figure 7.3: Magneto resistance vs field curve at different temperature (a-c) and MR ratio as a function of temperature (d) for probing a single magnetite domain.

MR measurements (up to 2 T) for probing a single magnetite domain at different temperatures are shown in Figure 7.3(a)-(c). The external in-plane field is applied along the current direction and the gap of the contact in these measurements is around 30 nm. Figure 7.3(d) shows the MR ratio measured at 2 Tesla as a function of temperature. A small MR ratio of -0.3 % was observed at

room temperature which is comparable to the MR ratio of bulk magnetite [9]. It can be observed from Figures 7.3(a)-(c) that nonlinear MR curves were observed for all temperatures, this is different to the case of probing one AF-APB. The studied temperature range can be divided into 3 regions, according to Fig. 7.3(d): region I (above T_V), region II (vicinity of T_V) and region III (below T_V). It can be noticed from figures 7.3 (a) to (c) that the shape of MR curve vary from one temperature region to another. This variation can be attributed to different mechanisms of spin dependent transport dominating at different temperatures. As there are no APBs and the gap between the contacts is close to the domain size, the MR effect is due to the rearrangement of spin moments for atoms. At temperatures above (region I) or below (region III) Verwey temperature (T_V), at weak fields, the configuration of the spins is only affected by the magnetic anisotropy field. A relatively small field is needed to align the spins far from the boundary, this corresponds to the initial change in resistance at low field. As the field is increased rotation of spins close to the boundary will start to take place, this is the reason for the observed linear behaviour at high field.

Above T_V we can write the resistivity as $\rho = \rho_0 exp[\frac{E_a}{k_B T}]$, where E_a is the activation energy [14]. Since the MR $<<$ 1, we can write MR$\approx \frac{E_a(H)-E_a}{k_B T}$ [15], where $E_a(H)$ is the field dependent activation energy. At temperatures below T_V (region III), the long range order sets in and the conductivity can be described by a variable range hopping [16] with a temperature dependent resistivity of the form $\rho = \rho_0 exp[\frac{T_0(H)}{T}]^{1/4}$, where the Mott temperature, $T_0(H)$ can be interpreted as a field dependent activation energy (in units of K) [17].

For a small field $T_0(H)$ can be expanded as a Taylor series, $T_0(H) = T_0 - \alpha(T)H + \beta(T)H^2$, where parameters $\alpha(T)$ and $\beta(T)$ are only slightly dependent on the temperature [17], this agrees with the temperature independent MR ratio observed below T_V (see Fig. 7.3(c)-(d)). The difference between the mechanisms

of transport at region I and region III and also less thermal spin disorder at low temperature could be reasons for the difference in shape of MR curves. In the vicinity of the Verwey transition (region II), the discontinuos change of the entropy [15] and the phonon-magnon interaction [18] play an important role which make the shape of MR curve different form those above or below T_V and also gives the MR extremum.

7.4 Conclusion

In summary, we have demonstrated the feasibility to probe one AF-APB and single magnetic domain of Fe_3O_4 using contacts with nanoscale gap. The experiment clearly shows that, in the case of probing one AF-APB, a large magnetoresistance, high resistivity, and a high situation field are observed compared to the case of single Fe_3O_4 domain. The shape of the MR curves shows that in the case of probing a single domain is found to be strongly temperature dependent. This information may have a strong influence on the realization of spin electronic devices which utilize magnetite-based hetero-structures.

References

[1] Margulies, D. T., Parker, F. T., Rudee, M. L., Speda, F. E., Chapman, J. N., Aitchison, P. R., and Berkowitz, A. E. *Phys. Rev. Lett* **79**, 5162 (1997).

[2] Voogt, F. C., Palstra, T. T. M., Nielsen, L., Rogojanu, O. C., James, M. A., and Hibma, T. *Phys. Rev. B* **57**, R8107 (1998).

[3] Hibma, T., Voogt, F. C., Niesen, L., a. van der Hieijden, P. A., de Jonge, W. J. M., Donkers, J. J. T. M., and van der Zaag, P. J. *J. Appl. Phys* **85**, 5291 (1999).

[4] Eerenstein, W., Palstra, T. T. M., Hibma, T., and Celotto, S. *Phys. Rev. B* **66**, 201101 (2002).

[5] Eerenstein, W., Palstra, T. T. M., Saxena, S. S., and Hibma, T. *Phys. Rev. Lett.* **88**, 247204 (2002).

[6] Eerenstein, W., Palstra, T. T. M., Hibma, T., and Celotto, S. *Phys. Rev. B* **68**, 014428 (2003).

[7] Celotto, S., W.Erenstein, and Himba, T. *Eur. Phys. J. B* **36**, 271 (2003).

[8] Margulies, D. T., Parker, F. T., Spada, F. E., Goldman, R. S., Li, J., Sinclair, R., and Berkowitz, A. E. *Phys. Rev. B* **53**, 9175 (1996).

[9] Ziese, M. and Blythe, H. J. *J. Phys: Condens. Matter* **12**, 13 (2000).

[10] Sofin, R. G. S., Arora, S. K., and Shvets, I. V. *J. Appl. Phys.* **97**, 10D315 (2005).

[11] Arora, S. K., Sofin, R. G. S., and Shvets, I. V. *Phys. Rev. B* **72**, 134404 (2005).

[12] Ramos, A. V., Moussy, J.-B., Guittet, M.-J., Bataille, A. M., Gautier-Soyer, M., Viret, M., Gatel, C., Bayle-Gillemaud, P., and Snoeck, E. *J. Appl. Phys.* **100**, 103902 (2006).

[13] Motida, K. and Miyahara, S. *J. Phys. Soc. Jpn* **28**, 1188 (1970).

[14] Ziese, M. and Srinitiwarawong, C. *Phys. Rev. B* **58**, 11519 (1998).

[15] Gridin, V. V., Hearne, G. R., and Honig, J. M. *Phys. Rev. B* **53**, 15518 (1996).

[16] Mott, N. F. *Conduction in Non-Crystalline Materials*, 17ff. Clarendon Press, Oxford (1993).

[17] Gong, G. Q., Gupta, A., Xiao, G., Qian, W., and Dravid, V. P. *Phys. Rev. B* **56**, 5096 (1997).

[18] Ogale, S. B., Ghosh, K., Sharma, R. P., Greene, R. L., Ramesh, R., and Venkatesan, T. *Phys. Rev. B* **57**, 7823 (1998).

Chapter 8

Conclusions and outlook

8.1 Introduction

Magnetite (Fe_3O_4) is an important ferromagnetic oxide, with a high Curie temperature (858 K) and a metal-insulator transition known as Verwey transition, despite decades of intensive research, the mechanism behind the transition remains an unsolved issue. Its predicted half metallic nature, attracted great interest for spin electronics application, but with unpromissing results [1]. Understanding mechanisms that affect magnetotransport behavior in Fe_3O_4 is of crutial importance in realization of its application as a magnetoresistive sensor. One of the mechanisms contributing to the magnetotransport is the anisotropic magnetoresistance (AMR), which is caused by the spin-orbit interaction and believed to be the transport equivalent to the magnetocrystalline anisotropy [2]. Although the experimental obsevation of the AMR effect is rather direct, its theoretical understanding is far from being complete. All theoretical attempts have been developed for ferromagnetic metals and its alloys [3, 4, 5, 6, 7] and some recent models for magnetic semiconductors [8, 9], but a theory for oxides is still lacking, due to the complexity of the interactions involved in this strongly correlated systems [10].

Previous studies of AMR of Fe_3O_4 focused on the magnitude of the effect and not on the magnetic field direction dependence, in this work we have performed measurements of the angular dependence of the anisotropic magnetoresistance. Measurements of the angular dependence of the anisotropic magnetoresistance in Fe_3O_4 films grown on flat and vicinal MgO(001) single crystal substrate shed light into the relation between the conduction mechanism and the presence of defects on the anisotropic magnetoresistance respectively. Using contacts with a nanoscale gap, we performed magnetotransport measurements through one antiferromagnetic APB and a single magnetite domain. Below we will describe the main results presented in this thesis.

8.2 Main Results

ANOMALOUS ANISOTROPIC MAGNETORESISTANCE IN Fe_3O_4(001) EPITAXIAL FILMS

Measurements of the angular and temperature dependence of the anisotropic magnetoresistance in epitaxial Fe_3O_4 films of different thickness grown on MgO (001) substrates and a Fe_3O_4 (001) single crystal show the presence of an additional anisotropy in AMR, supperimpossed to the conventional two-fold anisotropy. At temperatures below $\sim$ 200 K, this additional component gradually develops with the valleys near 90° and 270° broadening and as the temperature is further lowered an additional set of peaks appears showing an overall four-fold (cubic) symmetry. The observed effect is independent of thin film thickness and also present in the Fe_3O_4(001) single crystal, suggesting that, it is not exclusive to the epitaxial films and the presence of APBs, but rather an intrinsic property of the Fe_3O_4 system. The observation of this anomalous cubic component of AMR was compared with

the mechanism of the Verwey transition suggesting that its origin could be related to a change in the conduction mechanism of magnetite due to the presence of polarons at temperatures above T_V.

ANISOTROPIC MAGNETORESISTANCE OF Fe_3O_4 FILMS ON VICINAL MgO(001)

We have studied the anisotropic magnetoresistance of Fe_3O_4 thin films grown on MgO (001) substrate with a miscut angle with respect to the (001) plane along the <100> direction, due to the miscut, the presence of atomic steps is expected on the surface of MgO. The translational break of symmetry induced by the presence of steps is expected to influence the magnetic anisotropy of the films as well as their anisotropic magneto-transport properties. Furthermore the presence of atomic steps is expected to favour the formation of a regular array of APBs along the direction of the step edges (SE). Measurements of in-plane magnetization hysteresis loops show that the presence of atomic steps induces an uniaxial anisotropy within the plane of the films, which could be observed at all temperatures studied. This uniaxial anisotropy was suggested to relate to the anisotropy in the magneto-elastic energy due to the different strain status of the films in the directions parallel or perpendicular to the steps. This magnetoelastic anisotropy on the films could explain the observed easy axis behaviour in the direction perpendicular to the step edges. Measurements of the angular dependence of the AMR for current applied parallel and perpendicular to the SE, show that the AMR symmetry is not visibly affected at high temperatures and at temperatures just above the Verwey transition (T_V). However, below T_V, a dramatic change is observed when comparing the symmetry of AMR for current applied parallel or perpendicular to the SE. The data was analyzed in terms

of the uniaxial (a_u) and cubic (a_c) components of AMR. The a_u component is proportional to the AMR ratio and, below T_V, it shows different behaviour for current applied parallel or perpendicular to SE. For current applied parallel to SE a_u changes from positive to negative on cooling through T_V, similar to Fe_3O_4 films grown on non-vicinal substrates, while on the direction perpendicular to SE it remains positive. The observed differences in sign could be understood within a two-band model for magnetite. For Fe_3O_4 films grown on non-vicinal substrates; at high temperatures the positive sign in a_u can be understood as a consequence of the presence of a majority spin band at the Fermi level as suggested by Ziese [11], this agrees with the disappointingly low spin polarization values observed for magnetite [1], with decreasing temperature the majority spin band moves away from the Fermi level and the one-band case, with negative a_u, is eventually reached. This explains the observed behavior for non-vicinal and vicinal samples along the SE direction. In the direction perpendicular to SE, due to the presence of regular array of APBs and the antiferromagnetic coupling induced by them, it could be expected that as a consequence of the spin scattering they induce, the conduction electrons will suffer a spin flip, this will effectively restore the two-band model and induce a positive a_u. The a_c is not affected by the presence of steps showing similar response for current parallel or perpendicular to the SE for all temperatures measured, this further proves the intrinsic nature of the cubic component.

MAGNETO-TRANSPORT PROPERTIES OF Fe_3O_4 PROBED USING CONTACTS WITH NANO-SCALE GAP

Magneto-transport measurements were performed on 60 nm Fe_3O_4 films grown on MgO(001), in which nano-scale gaps of different dimensions have been deposited.

The separation between APBs in Fe_3O_4 films on MgO is known to scale with the thickness, for a 60 nm thick film the average domain size is around 50 nm. In order to measure an antiferromagnetic APB (AF-APB) and single magnetite domains, gaps of 80 nm and 30 nm were deposited respectively. The measurements clearly show the different transport properties, with an increased resistance and MR in the case of the measurement of one AF-APB, in comparison to a reduced resistance and lower MR for the single magnetite domain. The resistance increases by more than one order of magnitude in the case of on AF-APB while the gap distance is only increased by 8/3. The MR characteristics show different behaviour, with an approximately linear dependence with the applied magnetic field in the case of probing one AF-APB (80 nm gap) and a non-linear MR behaviour when measuring a single magnetite domain (30 nm gap). Furthermore we find that the shape of MR curves for a single Fe_3O_4 domain is temperature dependent while essentially independent for one AF-APB case.

8.3 Future work

8.3.1 First principle studies of the effect of regularly spaced APB arrays on the strain relaxation and band structure properties of magnetite films

In order to clarify the origin of the different behaviour observed in AMR of the films grown on vicinal substrates, when measured parallel or perpendicular to SE direction below the Verwey transition; further studies of the effect of regularly spaced arrays of APBs, on the magnetic and transport properties are required. First principle studies of the effect of the regular array of APBs, on the magne-

toelastic properties, as well as, on the band structure of magnetite, would help to clarify the underlying mechanism behind the obseved behaviour.

8.3.2 Measurement of exchange induced domain wall resistance

We have performed the initial steps to test a recently proposed magnetoresistive nanostructure [12], which utilizes domain wall (DW) scattering, where the magnetoresistance (MR) is enhanced by creating multiple DWs in a nanowire. The multiple DW structure is created by intermingled areas with pinned and unpinned magnetic moments of a ferromagnetic nanowire. The regions with pinned magnetic moments are obtained by exchange of selected areas of the ferromagnetic nanowire with an antiferromagnet, in this manner, the field required to rotate the magnetization will be different in the pinned and unpinned areas, with the subsequent formation of DW at the boundary between the regions. Although DW scattering leads to an order of magnitude smaller MR effect than spin dependent scattering in magnetic tunnel junctions (MTJs) or giant magnetoresistance (GMR) structures, it is expected that very narrow DW leads to MR values on the order of 100% [13]. The selected exchanged biased medium was the CoO/Co system. Thin films of 13nm Co were deposited by MBE, the CoO layer was obtained by introduction of oxygen at room temperature, obtaining a 2nm oxide layer as checked by x-ray reflectivity (XRR), in agreement with previous studies [14]. After oxidation the film was capped with 3 nm Au. This oxide layer is enough to produce an exchange bias field of -330 Oe at 77 K when grown on the 13 nm Co layer, as it can be observed in figure 8.1, where we show the magnetization hysteresis loops obtained at different temperatures after cooling on an external magnetic field of 4 kOe.

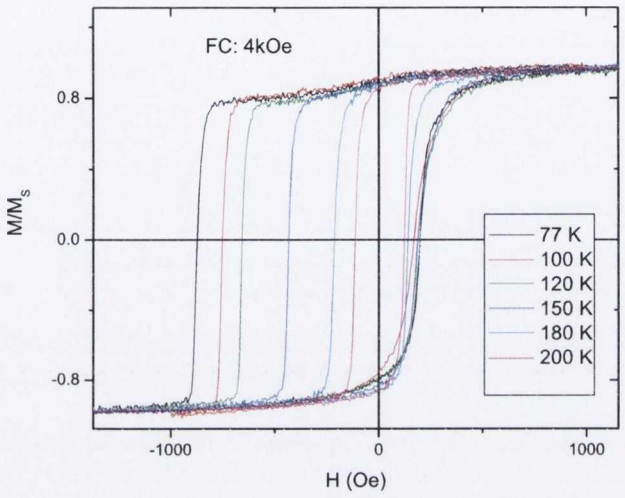

Figure 8.1: Exchange bias in the CoO/Co system

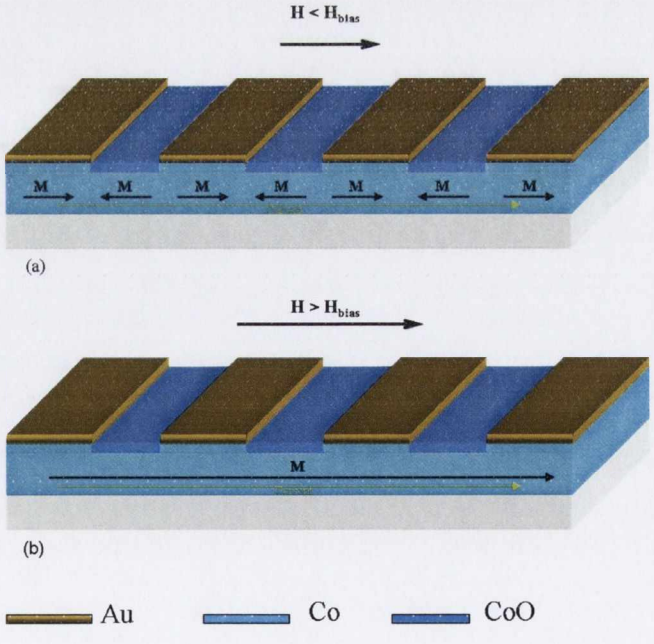

Figure 8.2: Geometry of the magnetoresistive device.

To test this idea, we followed a top-down approach by means of electron beam lithography (EBL), in order to create the array of successive regions with pinned and unpinned magnetic moments. Initially, 13nm Co was grown and capped with 3nm Au previous to any oxidation step. In the first lithography step, we opened windows on the Au layer for the selective oxidation of the Co layer underneath. In such a way we obtained the areas with pinned and unpinned magnetic moments in the Co film, a schematic is shown in figure 8.2. A second lithography step is performed to create the Co nanowire and the final step is to contact it by deposition of Au/Ti contacts and lift-off. A SEM picture of one of the obtained devices is shown in figure 8.3, the Co wire is 250 nm width, the magnetically pinned regions are 150 nm wide, with a separation of 400 nm.

Measurement of the magneto-transport properties on the obtained magnetoresis-

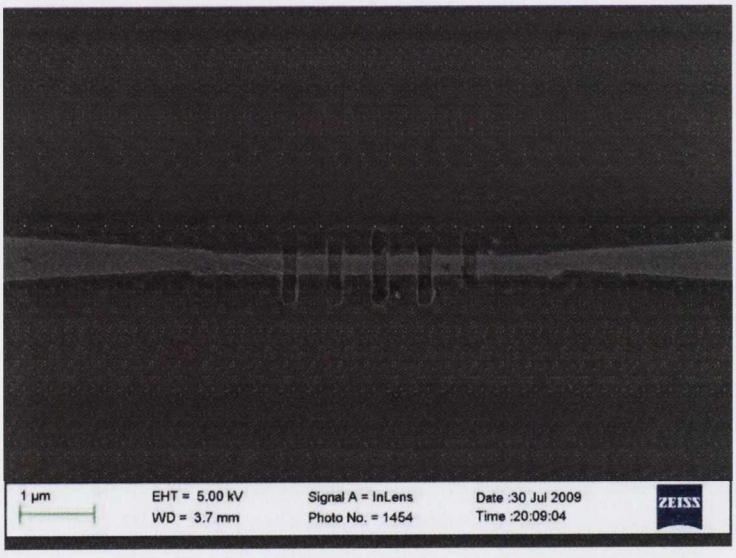

Figure 8.3: Picture of the CoO/Co device.

tive devices are to be performed. This results will help to clarify the mechanism of domain wall resistance obtained by means of an anti-ferromagnetically exchange biased medium. Similar experiments performed with structures obtained by UV

lithography [15, 16, 17] have been far from promising. The reduced dimmensions that can be attained with EBL structures will allow for smaller wire dimmensions which should suppress complex wall structures, such as vortices and possibly leading to sharper domain walls [18].

The final aim of the experiment is to develop the magnetoresistive medium using nanowires grown by the atomic terrace low angle shadowing technique (ATLAS) [19], this technique allows for the growth of self assembled nanowires of antiferromagnetic material that can act as the pinning areas of a deposited ferromagnetic overlayer. The advantaged of the ATLAS tecnique is the reduction of the lithography steps and the possibility to obtain wires of smaller dimmensions and with smaller separation than those achieved with the top-down lithographic tecniques.

8.3.3 Nanoscale microwave oscillator

While miniaturisation is the general trend in the electronics industry, it is being negatively impacted upon because microwave generators have not undergone miniaturisation equivalent with other electronic components, i.e. transistors. Here, based on ATLAS we propose the realisation of a high density matrix of nanocontacts for the realisation of spin torque induced generation of microwaves. Figure 8.4 shows a schematic of the proposed device geometry. A highly dense array of nanowires, deposited by ATLAS technique will constitute the free magnetic layer of the nano-oscillator, where the microwave oscillations shall be excited. The second ferromagnetic cross electrode separated from the free layer by a normal metal spacer layer shall be formed by means of lithography.

The concept of spin torque generated microwave oscillations has been previously used in a configuration, where the junctions were created by means of depositing the multilayer structure and making the nanocontacts by lithography. The spin

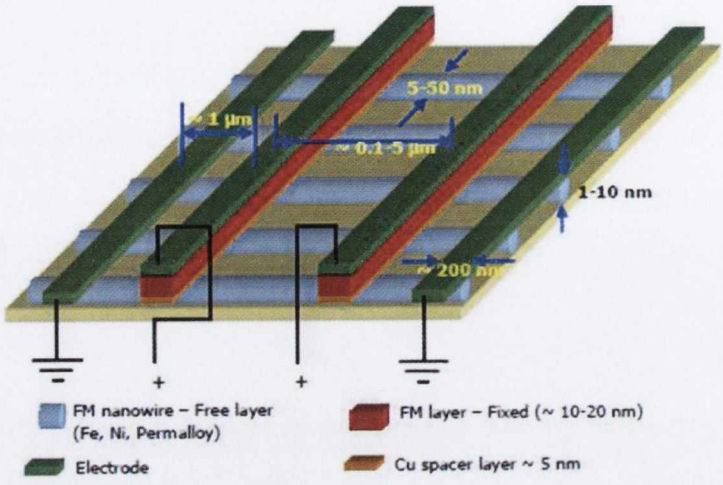

Figure 8.4: Schematic of the proposed STO configuration. The active regions comprise the interface between the nanowires and the Cu/FM/Electrode structure.

polarised current was injected into a nano-pillar composed of two ferromagnetic layers separated by a normal metal spacer [20, 21, 22].

The aim of the project is the generation of spin torque microwave oscillations, the study of the phase coherency and mechanism of phase locking in an array of nanocontacts and the differences between the different possible coupling mechanisms between the nanocontacts, for example two neighbouring oscillators along the same wire or two neighboring oscillators in adjacent wires should have different coupling mechanisms. One of the key advantages of the ATLAS technique is its wide range of separation between the nanowires; from dimmensions as small as 3-5 nm up to several microns.

References

[1] Li, X. W., Gupta, A., Xiao, G., Qian, W., and Dravid, V. P. *Appl. Phys. Lett* **73**, 3282 (1998).

[2] McGuire, T. R. and Potter, R. I. *IEEE Trans. Mag.* **11**, 1018 (1975).

[3] Smit, J. *Physica* **17**, 612 (1951).

[4] Campbell, I. A., Fert, A., and Jaoul, O. *J. Phys. C: Solid State Phys.* **3**, S95 (1970).

[5] Jaoul, O., Campbell, I. A., and Fert, A. *J. Magn. Magn. Mater.* **5**, 23 (1977).

[6] Potter, R. I. *Phys. Rev. B* **10**, 4626 (1974).

[7] Malozemoff, A. P. *Phys. Rev. B* **34**, 1853 (1986).

[8] Rushforth, A. W., Výborný, K., King, C. S., Edmonds, K. W., Campion, R. P., Foxon, C. T., Wunderlich, J., Irvine, A. C., Vašek, P., Novák, V., Olejník, K., Sinova, J., Jungwirth, T., and Gallagher, B. L. *Phys. Rev. Lett.* **99**, 147207 (2007).

[9] Výborný, K., Kovalev, A. A., Sinova, J., and Jungwirth, T. *Phys. Rev. B* **79**, 045427 (2009).

[10] Dagotto, E. *Science* **309**, 257 (2005).

[11] Ziese, M. *Phys. Rev. B* **62**, 1044 (2000).

[12] Shvets, I. V., Wu, H. C., Usov, V., Cuccuredu, F., Arora, S. K., and Murphy, S. *Appl. Phys. Lett.* **92**, 023107 (2008).

[13] Dennis, C. L., Borges, R. P., Buda, L. D., Ebels, U., Gregg, J. F., Hehn, M., Jouguelet, E., Ounadjela, K., Petej, I., Prejbeanu, I. L., and Thornton, M. J. *J. Phys.: Condens. Matter* **14**, R1175 (2002).

[14] Gruyters, M. and Riegel, D. *Phys. Rev. B* **63**, 052401 (2000).

[15] Nagahama, T., Mibu, K., and Shinjo, T. *J. Appl. Phys.* **87**, 5648 (2000).

[16] Buntinx, D., Brems, S., Volodin, A., Temst, K., and Haesendonck, C. V. *Phys. Rev. Lett.* **94**, 017205 (2005).

[17] Vandezande, S., Haesendonck, C. V., and Temst, K. *Appl. Phys. Lett.* **94**, 192501 (2009).

[18] Ebels, U., Radulescu, A., Henry, Y., Piraux, L., and Ounadjela, K. *Phys. Rev. Lett.* **84**, 983 (2000).

[19] Cuccureddu, F., Usov, V., Murphy, S., Coileain, C. O., and Shvets, I. V. *Rev. Sci. Instr.* **79**, 053907 (2008).

[20] Kiselev, S. I., Sankey, J. C., Krivorotov, I. N., Emley, N. C., Schoelkopf, R. J., Buhrman, R. A., and Ralph, D. C. *Nature* **425**, 380 (2003).

[21] Kiselev, S. I., Sankey, J. C., Krivorotov, I. N., Emley, N. C., Rinkoski, M., Perez, C., Buhrman, R. A., and Ralph, D. C. *Phys. Rev. Lett.* **93**, 036601 (2004).

[22] Krivorotov, I. N., Emley, N. C., Sankey, J. C., Kiselev, S. I., Ralph, D. C., and Buhrman, R. A. *Science* **307**, 228 (2005).